

**DESIGN OF ULTRA WIDEBAND RF ICs  
FOR MEDICAL IMAGING APPLICATIONS**

**BY**

**HOSSEIN KASSIRI BIDHENDI**

# **DESIGN OF ULTRA WIDEBAND RF ICs FOR MEDICAL IMAGING APPLICATIONS**

**By**

**HOSSEIN KASSIRI BIDHENDI**

A Thesis  
Submitted to the School of Graduate Studies  
in Partial Fulfillment of the Requirements  
for the Degree  
Master of Applied Science

McMaster University  
Hamilton, Ontario, Canada

Copyright by Hossein Kassiri Bidhendi, August 2010

MASTER OF APPLIED SCIENCE (2010)  
(Electrical and Computer Engineering)

McMaster University  
Hamilton, Ontario

TITLE:

Design of Ultra Wideband RF IC for  
Medical Imaging Applications

AUTHOR:

Hossein Kassiri Bidhendi,  
B.Sc. University of Tehran 2008

SUPERVISOR:

Professor M. Jamal Deen

NUMBER OF PAGES:

XVII, 159

# Abstract

Being the second most important cause of death in women, breast cancer attracted great interest from many research groups in different fields developing techniques to prevent, detect or cure it. Due to the fact that this disease can be treated if it is detected in early stages, many projects in this field have focused on early breast cancer detection. Modern imaging technologies have helped in the detection of this cancer but they still have high false positive or negative rates indicating a great need for more research in early breast cancer detection.

In 2002 the Federal Communication Commission allowed usage of 3.1 – 10.6 GHz frequency range for short-range medical and personal applications, and this has stimulated much research on one of the most interesting technologies for medical imaging. With the aid of advances in complementary metal-oxide-semiconductor technology as well as wireless communications, this imaging technology has steadily grow, and now, it has it has many attractive characteristics that makes it a perfect substitute for conventional imaging systems.

This thesis reports on the design of some key circuits for an ultra-wideband transceiver architecture that can be used for medical imaging and especially for breast cancer detection. In this work, we concentrated on the receiver and two of its major blocks, namely, a low noise amplifier and a mixer are designed, simulated, fabricated and tested. Both of these circuits are designed in 0.13  $\mu\text{m}$  technology and Cadence tools are used for simulation and layout.

First, a low noise amplifier is designed based on a common-source configuration with inductive degeneration and a third order Chebyshev input matching network. Using precise zero-pole analysis, two inductors have been added to the main architecture of amplifier to improve its gain bandwidth product. The designed circuit shows a very good performance in terms of all of design parameters. Voltage gain with a peak value of 18.6 dB and very acceptable flatness is achieved. Also the noise figure of this circuit had an average of 4.7dB and a minimum value of 3.3dB. Input and output impedance matching shows very satisfying performance for the whole range of 3.1 to 10.6 GHz. Moreover,

linearity of the circuit shows a very good performance compared with other works with IIP3 of -0.996 dBm. Finally, all of these specifications are achieved while consuming only 4.01 mW and occupying 1.3 mm<sup>2</sup> of chip area.

Second, an ultra-wideband mixer is designed to work as a multiplier in this configuration, and to perform a critical function in correlation block. The mixer is designed for both super- and sub-threshold modes of MOSFET operation, and in both modes, it shows very acceptable performance. While super-threshold mixer shows much better characteristics in terms of gain, noise and linearity, the very low power consumption of sub-threshold circuit along with its reasonable performance in terms of gain, noise and linearity makes both circuits excellent designs for niche applications. Excellent conversion gain of 22.54dB is achieved for super-threshold circuit together with minimum noise figure of 7.4 dB and IIP3 of 2.67 dBm, while consuming 6.67 mW and having excellent input impedance matching all over the bandwidth. On the other hand, the sub-threshold circuit dissipates only 623  $\mu$ W, with 13.44 dB of conversion gain and minimum noise figure of 7.67 and IIP3 of -7.47 dBm. This circuit has excellent input matching all over the UWB frequency range.

# Acknowledgements

I would like to start by expressing my highest gratitude to the Almighty God, for all His blessings upon me throughout my life.

I would like to thank Dr. Jamal Deen for his guidance, interest, knowledge, and enthusiasm for my research. I appreciate his vast knowledge and experience in Microelectronics, which, without his help, I can't imagine this work to be as good as it is. I would also like to thank Dr. Deen for hours of helping me and for allowing me to fabricate chips without any problem.

I also would like to express my sincere appreciations to Professor Chih-Hung Chen and Dr. Ognian Marinov for their help during the measurements. Without their help, I could not finish my work as good as it is now.

My thanks also go to my colleagues; without their support, I would still be stuck at my first design. I would like to express my appreciation to Darek Palubiak and Munir El-Desouki for sharing with me their knowledge and experience in circuit design and answering all of my questions. I would also like to say thanks to Waleed Shinwari and Jahed Tajik for useful discussions.

I would also like to thank the administrative and technical staff of the ECE department of McMaster University: Cheryl Gies, and Cosmin Coroiu. My special thanks goes to Terrance Greenlay for his continued efforts to keep Cadence in a good condition.

I am truly indebted to my family, and my appreciation and gratitude would not be finished without saying thanks to them. I would like to give my deepest appreciation to my wife, Maryam, who has always been there in good moments and in bad ones. Without her support I would not have been able to work throughout these years.

Last, but not least, I thank my wonderful family. Living so far from you and for so long makes me appreciate and love you even more. I can't thank you enough, Mom and Dad, for all your support, love and understanding.

# Table of Contents

---

Abstract .....	IV
Acknowledgement .....	VI
Table of Contents .....	VII
List of Figure.....	X
Kist of Tables.....	XIV
List of Acronyms .....	XV
<b>Chapter 1</b> .....	<b>1</b>
Introduction.....	1
1.1. Motivation.....	1
1.2. Background.....	2
1.3. Objective.....	4
1.4. Methodology.....	6
1.5. Thesis Layout.....	7
1.6. Contributions.....	8
<b>Chapter 2</b> .....	<b>9</b>
UWB Systems for Medical Imaging Systems .....	9
2.1. UWB Definition.....	9
2.2. UWB Basics:.....	10
2.3. Advantages and Challenges .....	13
2.3.1. Advantages.....	13
2.3.2. Challenges:.....	17
2.4. UWB Applications.....	18
2.5. UWB Medical Applications.....	19
2.5.1. Background and History .....	19
2.5.2. UWB Benefits for Medical Applications.....	20
2.5.3. Medical Applications .....	21
2.5.3.a. Medical Monitoring .....	21
2.5.3.b. Medical Imaging .....	22
2.5.4. Medical Imaging for Breast Cancer.....	24

<b>Chapter 3</b> .....	28
UWB Systems for Medical Imaging Applications .....	28
3.1. UWB Transceiver Basic Architecture .....	29
3.2. UWB Technologies.....	32
3.2.1. Pulse on technology .....	32
3.2.2. Sub-Carrier Technology.....	34
3.2.3. Multi-Spectral Solutions, Inc. ....	35
3.2.4. Xtreme-Spectrum Inc.: Trinity.....	36
3.3. UWB Circuit Implementation.....	37
3.3.1. Pulse Generator .....	37
3.3.2. Correlator.....	42
3.4. UWB antennas .....	44
3.4.1. Antenna Characteristics.....	45
3.4.2. Antenna Types .....	47
3.4.2.a. TEM Horn Antenna.....	48
3.4.2.b. Impulse Radiating Antenna.....	48
3.4.2.c. Folded Horn Antenna.....	49
3.4.2.d. Dipoles and Monopoles .....	49
<b>Chapter 4</b> .....	52
Ultra Wide Band Low Noise Amplifier (LNA).....	52
4.1. LNA Literature Review .....	53
4.2. Common Gate .....	53
4.3. Design Techniques.....	57
4.3.1. Shunt feedback.....	57
4.3.2. Noise Cancellation .....	58
4.3.3. Distributed Amplifiers .....	60
4.4. Common Source.....	61
4.5. Chebyshev Broadband Matching .....	67
<b>Chapter 5</b> .....	71
Design of an Ultra WideBand LNA.....	71
5.1. Introduction.....	71
5.2. LNA Design Parameters .....	71

5.2.1. Linearity .....	72
5.2.2. Noise Figure.....	74
5.2.3. Input Matching.....	80
5.2.4. Gain Analysis.....	81
5.3. Design Procedure .....	89
5.4. Layout .....	93
5.5. Measurement Results .....	94
<b>Chapter 6</b> .....	<b>103</b>
Ultra Wide Band Mixer Design.....	103
6.1. Mixer Topologies.....	104
6.2. Literature Review.....	109
6.3. Mixer Design Parameters.....	116
6.3.1. Noise Figure.....	116
6.3.1.a. Load Noise .....	116
6.3.1.b. RF Transconductance Noise .....	116
6.3.1.c. Direct Noise .....	117
6.3.1.d. Indirect Noise.....	120
6.3.2. Gain and Linearity .....	123
6.3.3. Input Impedance Matching .....	128
6.4. Design Procedure .....	134
6.5. Layout .....	138
6.6. Measurement.....	140
<b>Chapter 7</b> .....	<b>148</b>
7.1. Conclusion .....	148
7.2. Future Work.....	149
<b>References</b> .....	<b>152</b>

# List of Figures

---

Figure 1.1: Frequency dependence of dielectric constant and conductivity for fatty breast tissue, skin and tumor [6].....	2
Figure 1.2: Power level of UWB system in comparison with narrowband and wideband systems [10] .....	3
Figure 1.3: UWB emission limit for indoor systems. [10]. .....	3
Figure 1.4: Figure 1.4. Block diagram of a UWB medical imaging system for breast cancer detection. ....	4
Figure 1.5: Hemi-spherical configuration used for breast cancer detection [6]. ....	5
Figure 1.6: Detected signal for different positions of tumor. Thick solid line is the average of calibration waveform [6].....	5
Figure 1.7: Received signals compared with average waveform for two cases of normal and malignant tissues [10].. ....	6
Figure 2.1: Sine function waveforms in time and frequency domains.. ....	10
Figure 2.2: UWB pulse waveforms in time and frequency domains.....	11
Figure 2.3: Guassian function waveforms in time and frequency domains [11].....	11
Figure 2.4: An example of direct sequence UWB in which the whole band is dedicated to one ultra-short signal [11].....	12
Figure 2.5: An example of frequency spectrum of multi-channel technique [11].....	13
Figure 2.6: Comparison between narrow- wide- and ultra wide-band technologies in terms of bandwidth and signal power [11].. ....	14
Figure 2.7: A demonstration of multipath problems that happens in narrow-band communication systems [11].. ....	16
Figure 2.8: Transceiver architecture of both narrowband and UWB communication systems. This comparison shows how much simpler UWB transceiver is [11].. ....	17
Figure 2.9: Multiple Access Interference (MAI) [11].. ....	19
Figure 2.10: Detection of any movement in the room. [13]. ....	23
Figure 2.11: Body monitoring and imaging apparatus and method proposed by McEwan [12].....	24
Figure 2.12: Images from McEwan's Patent (Patent No. 5,573,012) [12].....	24
Figure 2.13: Obstetrics Imaging using UWB radar [14].....	25
Figure 3.1: Typical transmitter of a UWB system [24]. ....	30
Figure 3.2: Typical basic structure of a UWB receiver [24].....	31
Figure 3.3: Correlation results of transmitted and received signals [24].....	32

Figure 3.4: Block diagram of a typical transmitter and receiver for UWB technology [24]	34
Figure 3.5: Control signal generation for PTD block in sub-carrier technology.[24]	35
Figure 3.6: Scheme of pulse generation in Multi-Spectral Solutions Method. [24]	36
Figure 3.7: Primary and final pulses in Trinity pulse generation method. [24]	38
Figure 3.8: Frequency mask for UWB indoor devices set by FCC [10]	39
Figure 3.9: Top level design of pulse generation architecture [24]	40
Figure 3.10: Waveform in different phases of monocycle generation presented in figure 3.9 [24]	40
Figure 3.11: Using XOR gate for pulse generation [24]	41
Figure 3.12: Using AND gate for pulse generation [24]	41
Figure 3.13: A single ended to differential converter [24]	42
Figure 3.14: Analog subtractor [24]	43
Figure 3.15: Pulse generator's analog subtraction circuit [24]	44
Figure 3.16: Integrator schematic which can be used in the body of correlator in UWB receiver architecture [24]	45
Figure 3.17: Correlator which is used in UWB received design [24]	46
Figure 3.18: Ringing effect of antenna for UWB systems. [24]	48
Figure 3.19: Folded horn antenna [24]	51
Figure 3.20: Some examples of bow-tie antenna [24]	52
Figure 4.1: UWB LNA in medical imaging UWB system architecture [34]	53
Figure 4.2: Common Gate UWB LNA proposed in [35]	55
Figure 4.3: Noise figure of UWB CG-LNA proposed in [35]	56
Figure 4.4: The gm-boosting technique proposed in [36] to improve noise figure of CG stage.	57
Figure 4.5: Noise figure of circuit proposed in [36] and effect of proposed idea in this work.	58
Figure 4.6: (a) Narrowband LNA topology. (b) small-signal model. [37]	59
Figure 4.7: (a) Proposed idea of adding a shunt feedback to narrow-band LNA structure. (b) small signal equivalent of input circuit after adding shunt feedback [37].	60
Figure 4.8: Proposed broadband noise cancelling LNA [39]	61
Figure 4.9: Simulated noise contribution of M1 with and without noise cancelling. [39].	62
Figure 4.10: Schematic circuit diagram of cascade CMOS distributed amplifier [40].	63
Figure 4.11: LNA with a shunt input resistor [41]	64
Figure 4.12: LNA with a resistive shunt feedback.	65

Figure 4.13: LNA with shunt feedback provided by M2.....	66
Figure 4.14: An inductively degenerated LNA.....	67
Figure 4.15: (a) Two port noise model of MOSFET (b) Source degenerated MOSFET represented by a two-port.....	68
Figure 4.16: Inductively-degenerated cascode LNA. ....	69
Figure 4.17: An inductively-degenerated cascode LNA with auxiliary capacitor in parallel with $C_{GS}$ . ....	70
Figure 4.18: Chebyshev Broadband matching network.....	71
Figure 5.1: Simulated 3 <sup>rd</sup> order voltage intercept point for different CMOS technologies. [48].....	74
Figure 5.2: Simplified schematic diagram of CMOS LNA using modified DS mode [49] .....	75
Figure 5.3: Main configuration of UWB LNA .....	76
Figure 5.4: Small signal model of inductively degenerated LNA shown in figure 5.3 without considering input matching network. ....	77
Figure 5.5: representation of LNA input impedance network .....	80
Figure 5.6: Schematic of LNA input network. ....	82
Figure 5.7: Completed LNA circuit after addition of both auxiliary inductors.....	85
Figure 5.8: Pole zero analysis results before and after putting $L_D$ . Two poles, one zero and one twin zero are generated as a result of putting $L_D$ .....	86
Figure 5.9: A comparison of gain curves before and after putting $L_D$ . As it is shown, due to adding this new inductor, gain has much higher values for higher frequencies compared to the case without $L_D$ . ....	87
Figure 5.10: Pole zero analysis results before and after putting $L_C$ . As it is shown, one new pole is generated and 3 poles are displaced. These changes caused gain curve to be more flat as well as a little improvement in very high frequencies of the band. ....	88
Figure 5.11: A comparison of gain curves before and after putting $L_C$ . As it is shown, due to adding this new inductor, gain is more flat compared to the case without $L_D$ and also it has higher values for frequencies in high-end of the band. ....	89
Figure 5.12: Gain comparison between this design and the LNA design which is presented in [16 of my paper]. Both designs use exactly the same topology and the only difference is that in our design two inductors have been added. ....	90
Figure 5.13: Input reflection coefficient versus frequency.....	91
Figure 5.14: Power gain of LNA for cases with and without LD and LC.....	92
Figure 5.15: isolation of LNA versus frequency. ....	92
Figure 5.16: Output reflection coefficient versus frequency. ....	93
Figure 5.17: Noise figure of LNA versus frequency .....	93
Figure 5.18: Third-order intercept point of LNA.....	94

Figure 5.19: Layout of Designed LNA with and without auxiliary inductors.....	95
Figure 6.1: UWB Mixer in medical imaging UWB system architecture.....	96
Figure 6.2: Bbasic Idea of a Mixer .....	97
Figure 6.3: An unbalanced Mixer .....	98
Figure 6.4: Single Balanced Mixer .....	99
Figure 6.5: Double Balanced Mixer , Gilbert Cell.....	100
Figure 6.6: Stacked Mixer on top of an LNA proposed in [56].....	102
Figure 6.7: Stacked Mixer and Oscillator proposed in [57].....	102
Figure 6.8: Bulk driven Mixer proposed in [60].....	103
Figure 6.9: Comparison of conventional and folded configurations for Gilbert cell [61]. .....	104
Figure 6.10: Folded cascode mixer proposed by Hsieh et al in [61]. .....	104
Figure 6.11: Characteristic graph of drain current vs gate-source voltage around threshold voltage for two different sizes of transistor [64].....	105
Figure 6.12: Circuit schematic proposed by lee and mohammady in [64]. .....	106
Figure 6.13: UWB folded-cascode mixer redrawn from [65].....	107
Figure 6.14: Single balanced mixer with switches noise. ....	109
Figure 6.15: Assumed switch I-V characteristics .....	110
Figure 6.16: A switch input voltage, b. mixer output current decomposed into noiseless response and pulse of noise. [68].....	111
Figure 6.17: Mixer output spectrum in presence of direct noise. [68].....	112
Figure 6.18: Waveforms resulting from a square-wave LO: (a) voltage at tail, (b) capacitive current, and (c) output current [68].....	113
Figure 6.19: A charge injection technique for improving the conversion gain and IP3 of a CMOS Gilbert Mixer proposed in [71].....	117
Figure 6.20: Common mode feedback for current injection [71] .....	118
Figure 6.21: . Improved charge-injection technique [71] .....	119
Figure 6.22: Charge injection with reduced noise consequences.[71].....	119
Figure 6.23: $S_{11}$ of Mixer in figure 6.13 for different $C_{ac}$ values.....	120
Figure 6.24: Input matching after addition of auxiliary inductor. ....	122
Figure 6.25: Active balun designed for input network of mixer.....	123
Figure 6.26: Noise Figure before and after addition of balun. As it is shown, adding balun will result in a significant increase in noise figure. ....	124
Figure 6.27: Mixer's Conversion gain before and after addition of balun. It is demonstrated that for lower frequencies, conversion gain increases with balun but it decreases much faster than original mixer for higher frequencies. ....	125

Figure 6.28: Mixer's noise figure for super- and sub-threshold modes.....	127
Figure 6.29: Mixer's conversion gain for super- and sub-threshold modes. ....	127
Figure 6.30: Mixer's reflection coefficient for both super- and sub-threshold modes. ..	128
Figure 6.31: (a) IIP3 for super-threshold mode. (b) IIP3 for sub-threshold mode. Both of them are for 6 GHz. ....	129
Figure 6.32: Layout picture of designed mixer.....	131

# List of Tables

---

Table 2.1: FCC power regulations for UWB indoor and outdoor applications [10] .....	9
Table 3.1: UWB Antenna Requirements [24].....	48
Table 6.1: Mixer Specifications Comparison .....	137

# List of Acronyms

---

UWB	Ultra WideBand	1
LNA	Low Noise Amplifier	6
EIRP	equivalent isotropic radiated power	3
FCC	Federal Communication Commission	9
PPM	Pulse Position Modulation	11
DS-UWB	Direct Sequence Ultra Wide Band	13
DSSS	Direct Sequence Spread Spectrum	14
OFDM	Orthogonal frequency division multiplexing	14
LPI/D	Low Probability of Interception or Detection	15
PG	Processing Gain	16
LOS	Line of Sight	17
NLOS	Non-Line of Sight	17
ADC	Analog to Digital Converter	20
MAI	Multiple Access Interface	20
WPAN	Wireless Personal Area Network	21
LLNL	Lawrence Livermore National Laboratory	24
MRI	Magnetic Resonance Imaging	27
IR-UWB	Impulse Radio ultra-wideband	30
TH-PPM	Time hopping pulse position modulation	30
PRF	pulse repetition frequency	31
PLL	phase locked loops	31
VCO	voltage controlled oscillators	31
AWGN	Additive White Gaussian Noise	31
SNR	Signal to Noise Ratio	31
PTD	Programmable Time Delay	35
FET	Field Effect Transistor	45
TEM	Transverse Electro Magnetic	51
IRA	Impulse Radiation Antenna	52

NF	Noise Figure	54
CG	Common Gate	55
CS	Common Source	55
MOSFET	Metal Oxide Semiconductor Field Effect Transistor	58
$F_T$	Transistor unity-gain frequency	64
$C_{gs}$	Gate source parasitic capacitance of transistor	68
IIP3	Input referred third-order Intercept Point	73
ICP	1-dB Input Compression Point	73
$V_{IP3}$	input voltage amplitude at which the first and third output voltage amplitudes are equal	74
IF	Intermediate frequency	97
LO	Local Oscillator	99

# Chapter 1

---

## Introduction

---

### 1.1. Motivation

Worldwide breast cancer is one of the leading causes of death among women. Only in US, tens of thousands deaths are reported yearly because of this type of cancer. 26% percent of all types of cancers among women are breast cancer [1]. It is now well-known that a high percentage of patients with this type of cancer can be cured if it is detected in the early stages. Therefore there are many works to develop and improve imaging systems to help early detection of this cancer. This includes works which are concentrated on improvement of image processing or optimizing imaging systems' architecture using new technologies.

Ultra Wide Band (UWB) is one of the newest technologies which is employed for imaging humans' body. It is based on using ultra narrow pulses in time domain. Many researches are being done, each one of them concentrated on a particular organ of body including heart, lung, breast and organs involved in breath and speech mechanisms [14].

The main motivation for using ultra-narrow pulses for breast imaging arises from the high contrast between the electrical properties of malignant and normal breast tissues. As an example, this contrast is 5:1 for relative dielectric constant and 10:1 for conductivity at microwave frequencies [2, 3] (see Figure1.1.). Also UWB microwave imaging systems are able to provide both adequate penetration depth and necessary imaging resolution [4, 5].

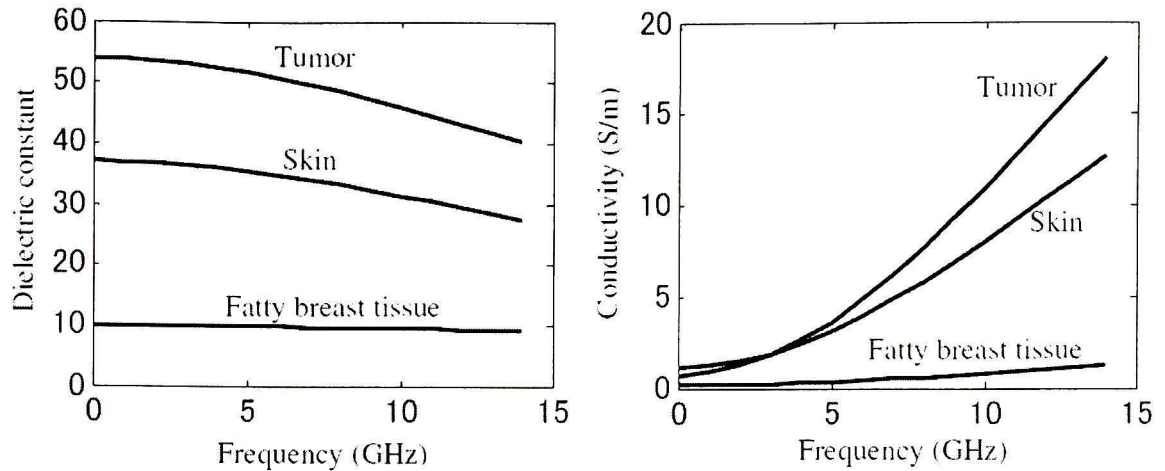


Figure 1.1. Frequency dependence of dielectric constant and conductivity for fatty breast tissue, skin and tumor [6].

In general some key technical features for any electrical medical instrumentation are non-invasiveness, low power, non-contact (remote operation), biocompatible, and biological and environmental friendly. Interestingly, UWB systems possess these properties. Considering all of above advantages, and compared to conventional imaging systems like X-ray and MRI, UWB imaging systems are showing good potential to be a strong substitute for those systems for niche applications; e.g. breast cancer detection.

## 1.2. Background

Ultra Wide Band (UWB) is a communication technology that can achieve high data rates of up to 1 Gbps, uses very low power pulses and is appropriate for short-distance applications [7-9]. Unlike narrowband communication systems, UWB systems does not have problems with fading due to use of short pulses which results in high multi-path resolution. Furthermore, because of wideband nature of these systems, power is distributed over a wide range of frequency which will result in very low power level required for these systems. Consequently, less interference with other radio frequency systems are expected.

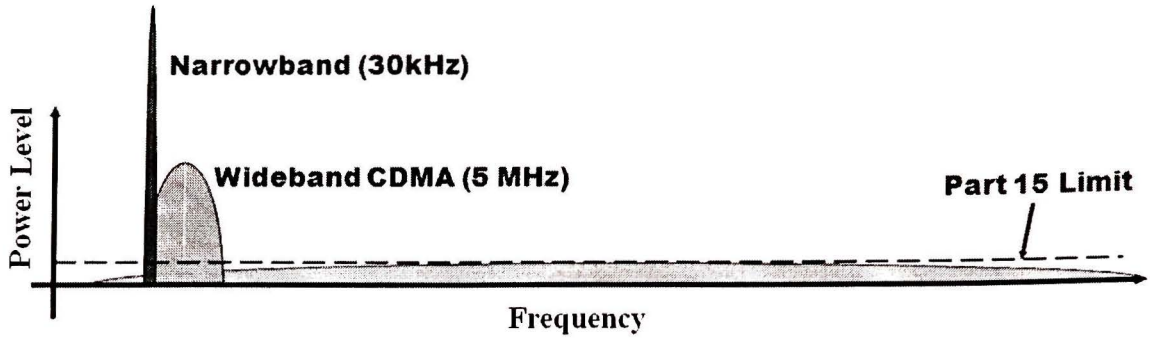


Figure 1.2. Power level of UWB system in comparison with narrowband and wideband systems. [10]

In 2002, the Federal Communication Commission (FCC) in the US authorized commercial use of the band from 3.1GHz to 10.6GHz for research and technology development of new electronic systems. Although, different narrow-band radio systems exist in this range of frequency, as long as UWB systems are satisfying FCC’s spectral mask, they can co-exist with them. This mask is shown in Figure1.3.

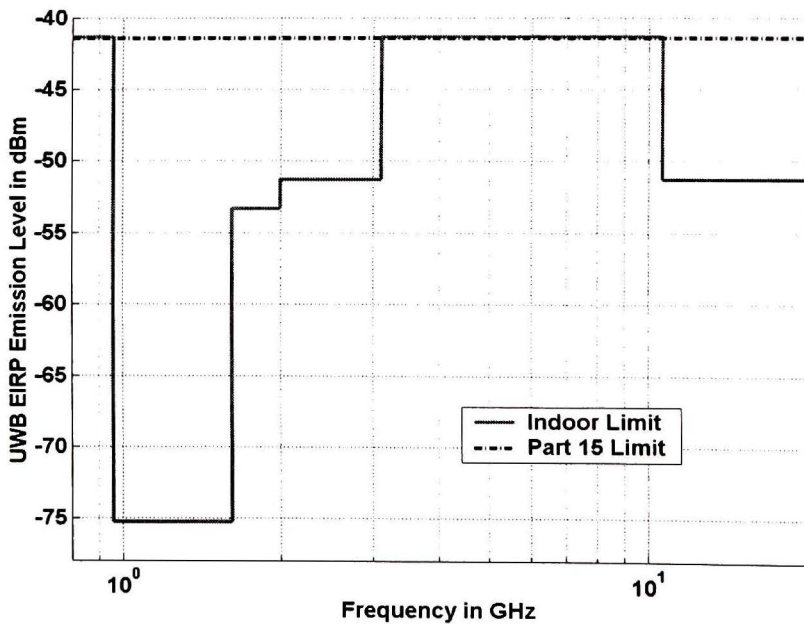


Figure 1.3. UWB emission limit for indoor systems. [10].

As it is shown in this picture, maximum equivalent isotropic radiated power (EIRP) spectral density which is allowed by FCC is -41.3 dBm/MHz. This mask suggests interesting short-distance applications for UWB range. Other than medical imaging, which is our application of interest, high resolution ground penetrating radar, localization at centimeter-level accuracy and personal area networks are other possibilities for this

technology. On the other hand, high spatial resolution of this technology makes it a promising candidate for medical imaging.

### 1.3. Objective

Figure 1.4 shows a symbolic block diagram of UWB medical imaging system for breast cancer detection.

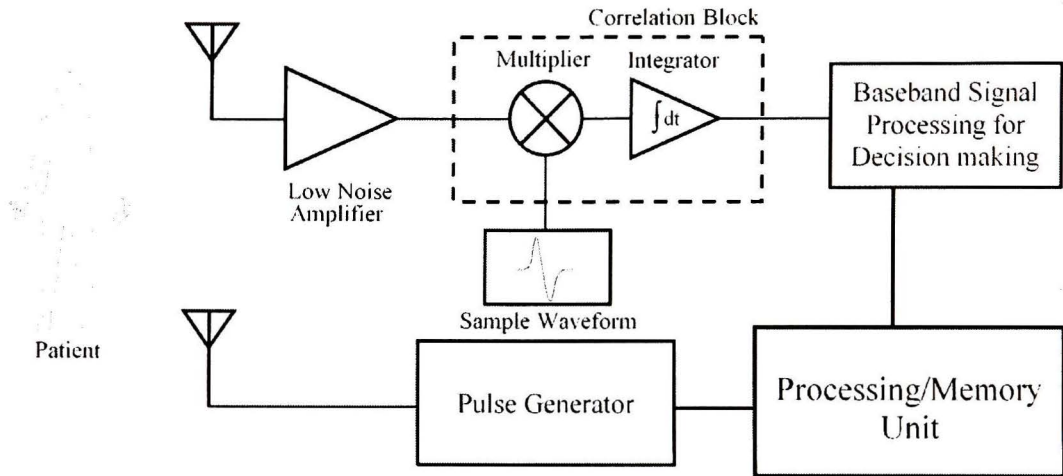


Figure 1.4. Block diagram of a UWB medical imaging system for breast cancer detection.

As shown in this picture, a UWB medical imaging system has some basic differences with narrowband systems. First, since there is no carrier in this type of communication, there is no need for complicated modulation and demodulation blocks. From this point of view, a UWB system's block diagram is much simpler than its narrowband counterparts. As seen from Figure 1.4, and as will also be explained in this thesis, for a UWB system, we use time-domain modulation for transmitting and receiving instead of frequency-domain. This makes the correlation and sample-waveform-generator blocks of this system very important, since they play a very important role in result generation.

The basic idea of breast cancer detection is to send ultra-narrow low-power pulses to the patient's body and then make a decision based on the received signal. The decision is made by comparing received signal with a sample signal, average of backscattered signals, or a signal backscattered from normal tissues. Figure 1.5 shows an example in which nine antennas are positioned on a human's breast in a hemi-spherical configuration.

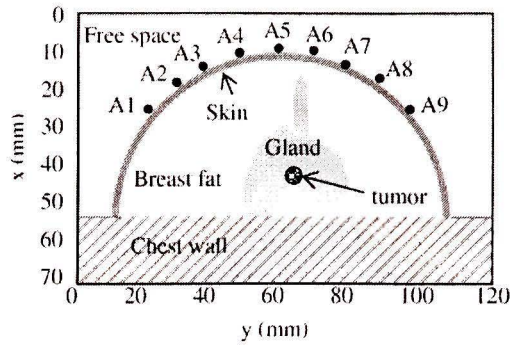


Figure 1.5. The hemi-spherical configuration used for breast cancer detection [6]

First, as shown in Figure 1.6, different pulses will be emitted from each of the antennas and detected by another antenna and location of simulated tumor is being randomly changed. Then, an average waveform of the received signals is calculated, an example of which is shown in Figure 1.6.

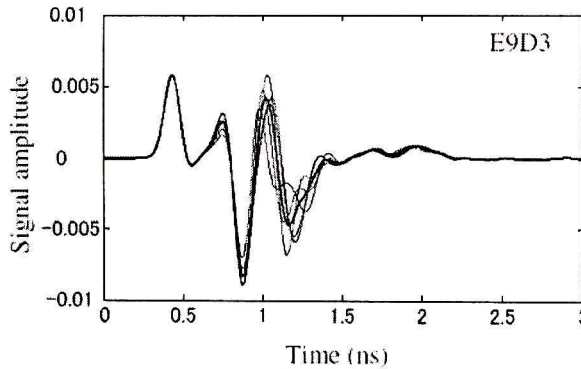


Figure 1.6. Detected signal for different positions of tumor. Thick solid line is the average of calibration waveform [6].

The next step would be using this waveform as a reference for future tests. Comparing the received signals with this waveform indicates the probability of a tumor existing in a specific location. Figure 1.7 shows two cases in which one of them is a normal tissue and the other one is for a malignant tissue. As it is shown, for the malignant tissue, differences between received signal and the average (calibration) waveform is much higher than for the normal tissue.

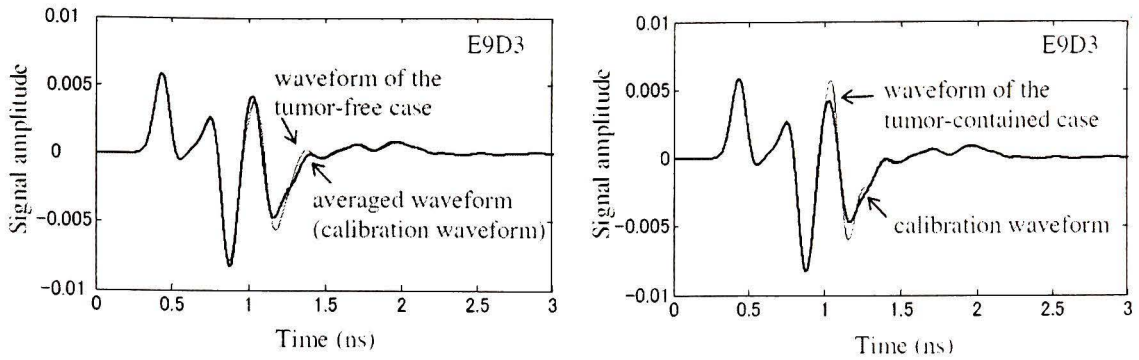


Figure 1.7. Received signals compared with average waveform for two cases of normal and malignant tissues [10].

This comparison is done in correlator block. As it will be explained later in this thesis, in the correlation block a sample waveform is generated using different methods (which will be discussed), and this plays the role of the average waveform in the above example. This waveform then will be compared with received signal using a UWB mixer which multiplies received signal with sample waveform and then an integration block sends a proper signal to decision making unit which is usually a micro controller. The decision unit's answer determines whether the targeted tissue is malignant or normal.

#### 1.4. Methodology

In this work, two main blocks of a UWB receiver are completely designed, simulated fabricated and tested. These blocks are the Low Noise Amplifier (LNA) and the Mixer. together with pulse generator, these three are the most important blocks of a UWB imaging system. The LNA is placed right after antenna to amplify the noisy signal and then its output sent to UWB mixer which operates as a multiplier. After the mixer, we have baseband signal processing. Thus, the only RF (Radio Frequency) circuits in this receiver architecture are the LNA and the mixer.

In this thesis work, the LNA is designed based on a Common Source (CS) configuration and a 3<sup>rd</sup> order Chebyshev filter for input impedance matching. With the addition of two inductors and adjustment of the poles and zeros of this circuit, the voltage gain of LNA is boosted significantly, while all of other circuit specifications keep their original values.

In the second part of this work, a UWB mixer based on a folded-cascode configuration is designed. Due to the unique features of selected configuration, low power, high gain and high linearity are achieved.

## 1.5. Thesis Layout

In this thesis, the design and simulation and measurement results of two main blocks of a UWB receiver namely LNA and Mixer is described.

In Chapter 2, we begin by defining the UWB concept and UWB technology and systems. Next we describe the advantages and challenges of this technology and practical systems. After that, UWB applications are studied. This study includes both medical and non-medical applications. Finally, in this Chapter, some basics of medical imaging are discussed.

Chapter 3 contains a description of the architecture of a UWB medical imaging system. First, different architectures are introduced, and second, different UWB technologies are described in detail. Following that, the circuit implementation of different blocks of this system, including pulse generator and integrator are described. The final section of this Chapter introduces UWB antennas and their required characteristics, after which, different types of antennas are presented.

Chapter 4 contains a thorough literature review of UWB LNAs and different techniques that can be used in design of this circuit. Different circuit configurations, including common-source and common-gate, and different variations of these structures, are introduced. Techniques for noise cancellation and feedback techniques, are also explained. After a detailed discussion of the advantages and disadvantages of the introduced topologies, the final LNA configuration which is selected for this work, is introduced.

In Chapter 5, the design of the LNA based on the configuration introduced at the end of Chapter 4 is described. In this Chapter different design parameters are introduced and ways to optimize each one of them are explained in detail. Linearity, noise figure, impedance matching and gain analysis are introduced, discussed and optimized. Next, new ideas based on precise pole zero analysis are explained. Results of these analysis and the way additional elements are placed to adjust these poles and zeros are also described. Finally, simulation results are presented followed by the layout and measurement results.

In Chapter 6 the UWB mixer is described. First, a literature review of different mixer topologies is introduced. Next the Gilbert mixer, which is the core of our selected design, is introduced. Its advantages over other topologies, together with its design challenges,

are explained. Then, different variations of Gilbert mixer are introduced, and their advantages and disadvantages described. And finally the selected configuration for our design is introduced. The next sections introduce different design parameters of the mixer and ways to optimize each of them. An extensive section is dedicated to noise and different mechanism of mixer noise, including transconductor, load, direct and indirect noises both for low- and high-frequency cases. Next, gain and linearity are discussed and techniques to improve these parameters are studied. Finally impedance matching of this mixer and two solutions to achieve excellent matching at higher frequencies are studied including their advantages and drawbacks. Finally design procedure and simulation results are presented together with layout of designed mixer. Finally in Chapter 7, the main results of the research work is presented. This Chapter also includes some recommendations for future work in UWB systems for medical applications.

## **1.6. Contributions**

In this work, UWB transceiver front-end is introduced and different technologies and topologies for its implementation are described. For the first block, the low noise amplifier, an extensive pole-zero analysis was performed and two new circuit elements have been added to improve both voltage gain amplitude and gain flatness. Noise figure optimization with regards to gain, bandwidth and power consumption has been done. Finally the circuit was laid out and its fabrication was arranged by CMC Microsystems. The fabricated LNA circuit was tested, the measured results were compared with simulation results and good agreement between them was obtained.

For the second block, the wideband mixer, two main approaches- Super-threshold and sub-threshold – were studied. For these two classes of mixers, two solutions have been proposed to solve input impedance matching problem. With the proposed input matching networks, excellent matching and improved conversion gain were achieved. To simplify the test configuration, an ultra-wideband balun was design and fabricated. This balun serves as the interface circuit between input signals (RF and LO) and mixer core. This chip was also fabricated and tested. Measurement results are compared with simulation results and good agreement was obtained.

## Chapter 2

---

# UWB Systems for Medical Imaging Systems

---

### 2.1. UWB definition

Regarding the Federal Communication Commission (FCC) ruling which was issued in February 2002, Ultra Wide Band (UWB) is allowed to be used for medical and commercial and any other unlicensed communication usage. According to FCC's definition any system with a  $B_f$  of lower than 0.2 is recognized as a UWB system, here  $B_f$  is defined as,

$$B_f = \frac{f_H - f_L}{f_H + f_L} \quad (1.1)$$

where  $f_H$  and  $f_L$  are higher and lower -10dB bandwidth. Also, any system with a bandwidth wider than 500MHz is also called UWB. The FCC put some radiation limits on this type of system, and these are listed in Table 2.1 below

Table 2.1.

FCC power regulations for UWB indoor and outdoor applications [10]

Frequency in MHz	Indoor	Outdoor
	EIRP in dBm	EIRP in dBm
960-1610	-75.3	-75.3
1610-1990	-53.3	-63.3
1990-3100	-51.3	-61.3
3100-10600	-41.3	-41.3
Above 10600	-51.3	-61.3

where EIRP is Equivalent Isotropically Radiated Power.

## 2.2. UWB Basics

In general, when we say that a signal is ultra-wideband, it means that the signal is very short in time domain and has a very wide bandwidth in frequency domain. In fact, this is the reason why UWB systems are sometimes called "impulse radio", "short-pulse", "super wideband" or "carrier less".

A common characteristic of all UWB communication systems is using ultra-short time pulses in transmission which results in ultra-wideband in frequency domain. Since the power is distributed over a wide range of frequencies, then UWB signals are usually noise-like and are well below interference level of existing narrowband systems. Although, this means that no price should be paid for the bandwidth it also cause serious challenges for detection and interception which should be solved.

Another effect of being wideband is avoiding conventional carrier-based communication systems that are used for narrowband systems. For UWB, communications is carrier-less, and modulations should be performed in time domain, e.g. Pulse Position Modulation (PPM). Another difference is that if we consider a narrowband signal which is shown in Figure 2.1, we see that it is confined only to a single frequency which makes it vulnerable to detection and interception.

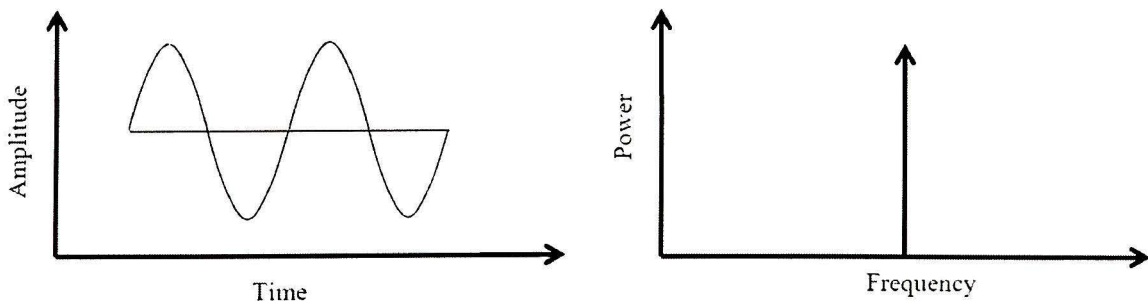


Figure 2.1. Sine function waveforms in time and frequency domains.

Ultra Wide Band signals are extremely-short pulses in time domain, which results in having wideband signal in frequency domain. The UWB pulse, which is shown in Figure 2.2, usually has a very short duty cycle. In fact  $T_{on}$  for UWB signal is around 1% of  $T_{off}$ . This makes communication power consumption considerably lower (~ thousand time lower) than a device like a cell phone.

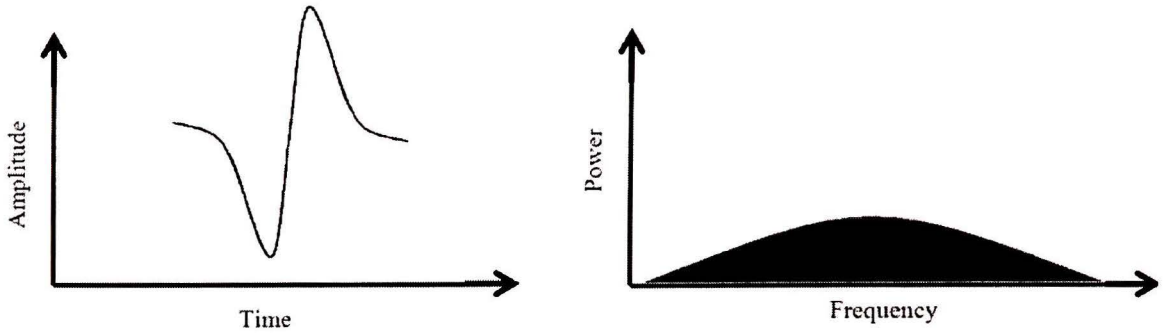


Figure 2.2. UWB pulse waveforms in time and frequency domains.

Various types of wideband signals including Gaussian, chirp, wavelet, or Hermite-based short-duration pulses can be used as UWB signal. As an example, Figure 2.3 shows a Gaussian monocycle which is first derivative of a Gaussian pulse. Following equation is the time-domain representation of this signal.

$$P(t) = \frac{t}{\tau} e^{-\left(\frac{t}{\tau}\right)^2} \tag{1.2}$$

As shown in Figure 2.3, a signal with 500ps duration in time causes a -10dB band ( $f_H - f_L$ ) of 1.4 GHz in frequency domain. The last basic fact about UWB signals and systems is being single- or multi-band. In fact, since 2002 that commercial use of UWB spectrum was allowed, two main approaches have been followed by major companies, each of them has its own advantages and disadvantages.

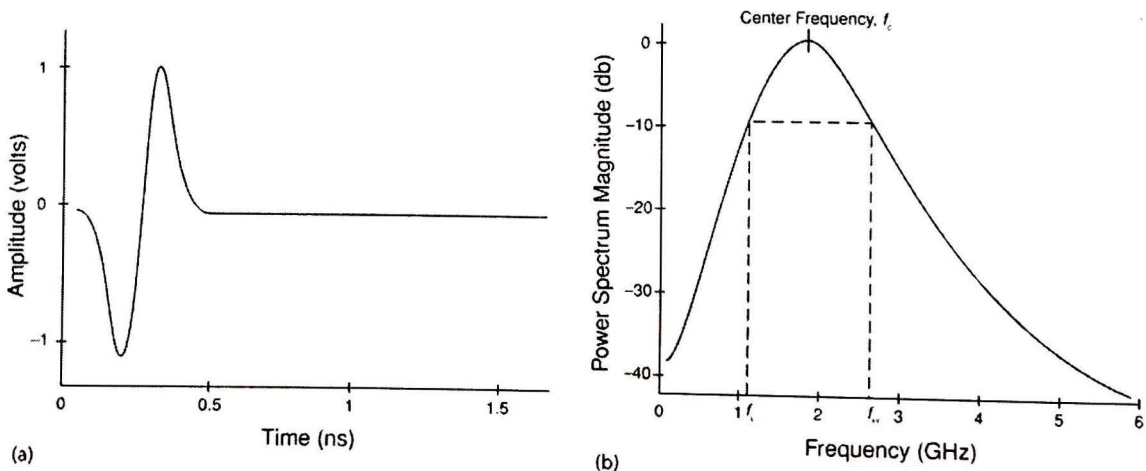


Figure 2.3 Gaussian function waveforms in time and frequency domains [11].

The first approach, which is basically the conventional definition of UWB, is Direct Sequence UWB (DS-UWB). In DS-UWB the whole band is dedicated to one ultra-short time signal. An example of this signal is shown in Figure 2.4.

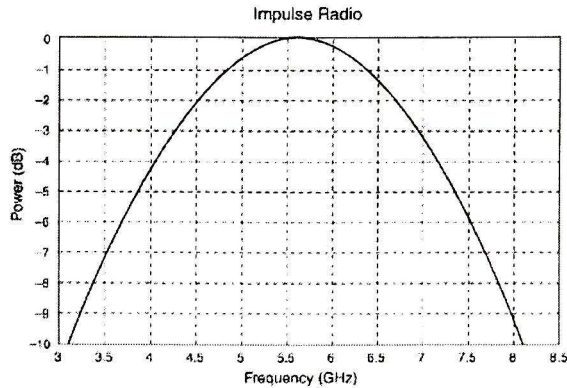


Figure 2.4. An example of direct sequence UWB in which the whole band is dedicated to one ultra-short signal [11]

The main advantages of this approach are now described. First, unlike the narrowband case, they do not experience any Rayleigh fading. This is basically because of wideband nature of this approach in comparison with the other one. Second, in this approach we use time-domain signal processing together with well-understood Direct Sequence Spread Spectrum (DSSS) techniques to transmit and receive information.

On the other hand, we have the multi-channel technique (second approach) which again has its advantages. In this technique, supporters of which include Intel and Texas-Instruments, it is believed that the 7.5 GHz band should be divided into multiple sub-bands in such a way that each band still has the requirements for being a UWB signal. These smaller bands in which each one is slightly wider than 500 MHz, are shown in Figure 2.5.

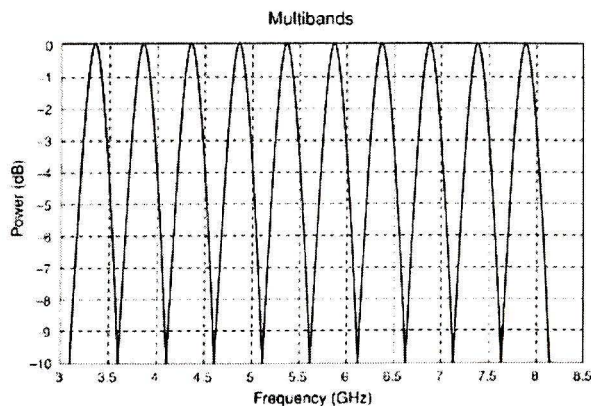


Figure 2.5 An example of frequency spectrum of multi-channel technique [11]

One advantage of this technique is that we can avoid transmission in some specific frequencies or band of frequencies to prevent potential interference with other

communication systems in the same band. Also, since each band is about 500 MHz, UWB pulses are not as short as in the traditional approach. Consequently, we can expect easier synchronization requirements. Finally, for modulation of this type of signals, different techniques are proposed, among them, the most popular is Orthogonal Frequency Division Multiplexing (OFDM).

To sum up, the first approach of one ultra short time signal can employ much simpler techniques to do transmission and reception, but it has possible difficulties with interference. On the other hand, the interference problem is solved in second multichannel technique. However the cost is more complex and more expensive modulation methods and communication techniques.

## 2.3. Advantages and Challenges

### 2.3.1. Advantages

Some of advantages and challenges of UWB systems are mentioned in above in section 2.2. In this section, we will discuss each one in more detail. The first advantage of these systems is their ability to co-exist with other communication systems due to its very low power nature. In fact, since UWB signals are below noise floor of a typical narrowband receiver, it would not make any interference with other narrowband communication systems. Figure 2.6 shows more clearly how coexistence of a UWB communication with a narrowband systems is possible.

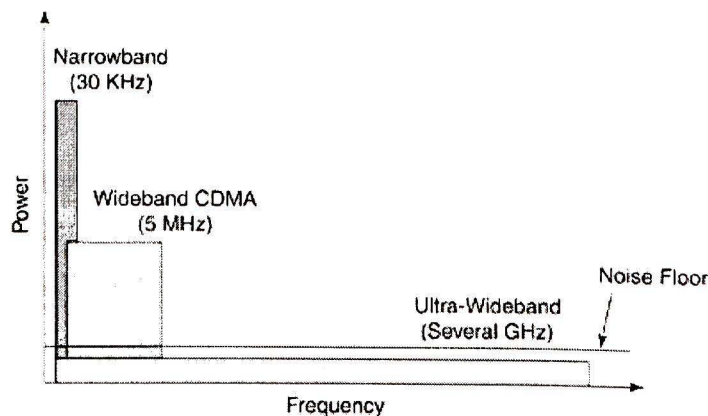


Figure 2.6. Comparison between narrow- wide- and ultra wide-band technologies in terms of bandwidth and signal power [11].

Another result of low average transmission power is immunity to interception and detection, which becomes very important especially in military applications. Also for example, considering the signal in time-domain, since the UWB pulse is an ultra-narrow pulse, it is very difficult to detect it without knowing the exact time of next pulse arrival. For example Low Probability of Interception or Detection (LPI/D) communications, which are mostly for military purposes, needs systems like UWB.

Another advantage for UWB systems, which comes from their wideband nature, is their channel capacity. As can be guessed from its name, channel capacity or data rate is the maximum data that can be transmitted per second over a communication channel. As a result, we can say that more bandwidth means more data rate. In fact, according to Hartley-Shannon capacity formula, we have

$$C = B \cdot \log_2(1 + SNR). \quad (1.3)$$

In this equation  $B$  is channel bandwidth and  $SNR$  is Signal to Noise Ratio. Knowing that channel bandwidth is 7.5 GHz and with a simple estimation, we can expect Gbps data rate for UWB systems. On the other hand, UWB regulation only lets us to use these systems for short-range applications. As a conclusion, we can say that UWB systems are perfect candidates for high data-rate, short range applications. We will see various examples of these applications in later sections. Also, another conclusion that we can get from the Hartley-Shannon formula is that if  $SNR$  is not high-enough, we still have a good data rate. This means that UWB systems are suitable to work with low  $SNRs$ .

Ultra Wide Band systems are also resistant to jamming. Jamming is an undesirable occurrence that frequently happens to wireless communications. To define it briefly, jamming is a deliberate or unintentional radio transmission that results in interference with the main communication stream at the same frequencies. For narrowband and wideband wireless communication systems, jamming is a serious problem; but this is not the case for ultra-wideband systems. For UWB systems, since the band is ultra-wide if a radio transmission make some interference for a frequency or for a band of frequency the signal can still be transmitted through rest of the band. Although resistance to jamming is dependent on type of modulation that is used for UWB communication, in some cases, strong traditional narrowband transmitters can result in jamming for UWB systems. It is

worth mentioning that to measure effect of jamming, we can use a term called processing gain, which is defined as

$$PG = \frac{RF \text{ Bandwidth}}{Information \text{ Bandwidth}} \quad (1.4)$$

Using this equation we can see why UWB systems have a high processing gain and consequently good resistance to jamming.

Another unavoidable problem in wireless communications is multipath effects. Usually, for wireless communications over short distances, there are more than one path between the transmitter and receiver. Among the different paths there is always one path which is a direct line between the transmitter and receiver. This path is called the Line of Sight (LOS). There are also other paths which are caused by presence of various types of obstacles or objects, including buildings, trees and people. We call second group of paths as Non-Line of Sight (NLOS).

Figure 2.7 shows that how in narrowband communications serious problems can be caused by these reflected signals from objects in the environment. It can be seen that if the reflected signal becomes out-of-phase with the main signal, it can significantly degrade the received signal. On the other hand, for UWB systems, since the UWB pulse is ultra-short in time (less than a nanosecond), it is highly improbable that main signal and the reflected signal reaches receiver at the same time to cause a degradation in the received signal. Again, immunity to multipath effect is related to the modulation scheme that we choose.

Beside the advantages mentioned above, wide range of frequencies in the UWB communications helps these systems to have a very good penetration capability. As a matter of fact, being wideband let the system use frequencies from very low to very high values. This means that for applications requiring superior penetration, UWB systems are able to use lower band of frequencies for better communication. (Although, we should have permission to use those frequencies).

The last advantage, which is one of the most important advantages of UWB systems, is their simple transmitting and receiving architecture. As mentioned before, UWB systems are carrier-less. This means that the circuitry needed for carrier based communications is avoided for these systems. For narrowband systems we need carrier translation as well as

carrier recovery stages. This means that, special mixers and oscillators should be designed for these systems. Plus, power amplifier (PA) stage is avoidable in UWB systems too because of the same reason.

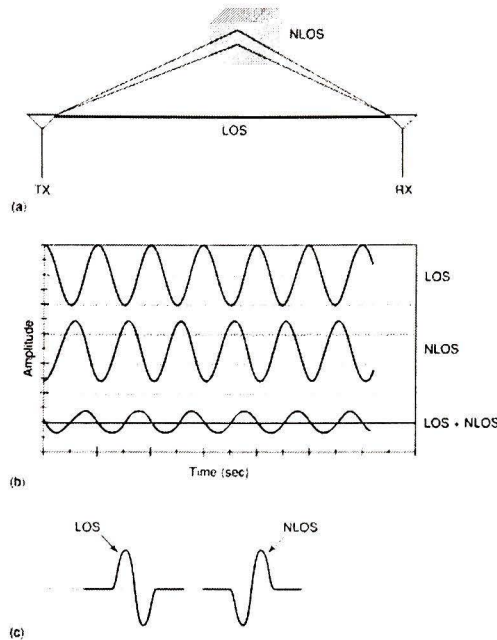


Figure 2.7. A demonstration of multipath problems that happens in narrow-band communication systems [11].

Figure 2.8 shows a transceiver architecture for both narrowband and ultra-wideband systems. From these two pictures it can be seen how much more complicated the transceiver architecture is designed for narrowband communication systems.

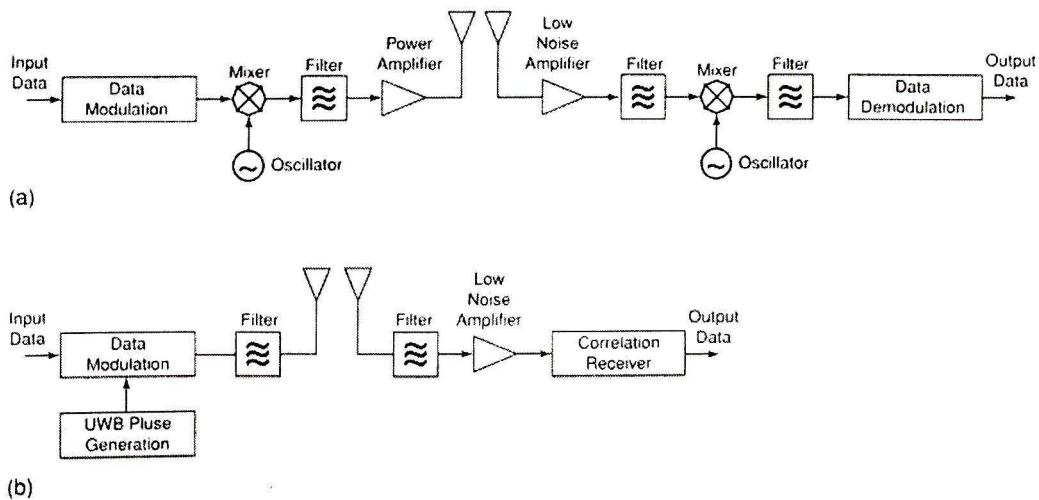


Figure 2.8. Transceiver architecture of both narrowband and UWB communication systems. This comparison shows how much simpler is the UWB transceiver is [11].

### 2.3.2. Challenges:

In the circuit design, besides the advantages of a specific circuit, challenges or trade-off always exist. The UWB systems are not exception. Most of the challenges that we face while using UWB systems are due to very short-time UWB pulses that are used for communication.

Basically, for narrowband systems, when the transmitted signal is a sinusoidal, the received signal has the same format, therefore minor distortion would not result in major changes in the type of signal. Unlike a narrowband system, the UWB pulses can be significantly distorted through the transmission link. To understand this fact quantitatively, Friis equation can be helpful. Regarding Friis equation, we have:

$$P_r = P_t G_t G_r \left( \frac{c}{4\pi d f} \right)^2 \quad (1.5)$$

In which  $P_r$  and  $P_t$  are receiver and transmitted signal power and  $G_r$  and  $G_t$  are receiver and transmitter gain respectively. Also  $C$  is light speed  $d$  is the distance and  $f$  is frequency. This equation shows that for narrowband systems with lower frequencies, changes in frequency will not make a big difference in the received signal power. On the other hand, for UWB signals, since the bandwidth is ultra-wide, then the received signal can be significantly degraded and as a result, the distortion effect becomes large enough to make the received signal totally different from the transmitted signal.

A second challenge, that is again a result of short pulse duration of UWB system, is channel estimation. In fact, to do this job, we need to have a template of expected received signal and compare this template to the transmitted signal to estimate different channel parameters like attenuation or delays of propagation in transmission path. On the other hand, due to very wide bandwidth of UWB systems, the received pulse becomes distorted in many ways and loses its original shape. This makes estimation of the channel parameters very difficult for these systems.

Synchronization is another issue for UWB systems which makes it very challenging to design. This problem arises from ultra-narrow pulses used in this type of communication. Like any wireless communication system, the transmitter and receiver must be synchronized for UWB systems. However, when we have sub-nanosecond pulses, synchronization becomes very challenging. The first challenge is the design of very fast

analog-to-digital converters (ADCs) (in the order of Gbps) to sample these narrow pulses. The second challenge is power consumption, which should be considered very carefully. Beside short pulse duration, power limitation, makes the performance of UWB systems highly sensitive to timing errors like jitter and drift. As a result, if we fail to meet power and speed requirements, we might face serious performance problems, most of them related to timing. An example is Pulse Position Modulation (PPM) which is highly dependent on timing and that can be completely useless if the timing and power limitations are not met.

Finally the last important challenge we mention is Multiple Access Interference (MAI). This kind of interference happens when different users or devices tries to send information wirelessly through a shared medium. In these cases, each receiver should be able to detect which signal is its favorite signal and that should be detected. To make this issue clear, Figure 2.9 demonstrates a multiple access case of communication.

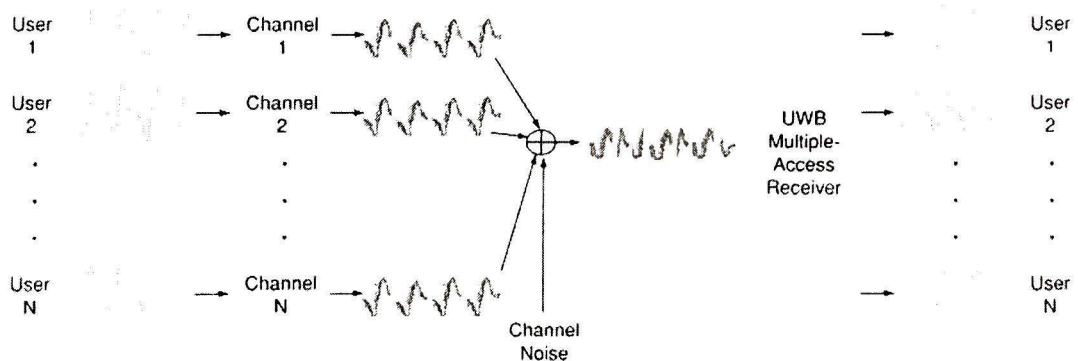


Figure 2.9. Multiple Access Interference (MAI) [11].

In MAI the receiver's channel capacity and performance are degraded. Channel noise and narrowband interference might cause a serious damage on UWB communication, especially when we have a low-power system. The above reason makes MAI an important challenge for UWB systems.

## 2.4. UWB Applications

Having described the advantages and challenges of UWB systems, we now can describe some suitable applications. First, as can be concluded from previous discussions, UWB

communications may be used only for short-range applications. Usually the range of most of the applications considered for ultra-wideband systems is below 10m. The narrow-pulses in UWB communications, results in very high speeds that are very difficult to achieve in other types of communication systems. these high speeds in UWB systems is achieved while consuming very low power, thus making this technology especially suitable for high-speed low-power, short-range applications.

Following the discussions above, one group of applications are wireless personal area networks (WPAN) in which a person can have a very high speed link between his own different electronic devices with very low power consumption. Examples of this group of applications are high resolution printers, scanners and storage devices, multimedia, MP3 and camera and DVD players.

Another group of applications for UWB is geo-location and localization. UWB becomes more special for these types of applications when we have multipath or obscured environment, as explained above.

The final group of applications for UWB (ignoring UWB radar applications) can be named generally as communication applications. Low probability of interception, high data rate over short ranges and the ability to work in multi-path environment are major characteristics of UWB systems that make them suitable to many kinds of communications.

Besides the above groups, UWB application for medical imaging and medicine is one of the most important ones. We can note that we can include this group of application under communication group. However, because of its importance, we dedicate a section to it. Prior to discussing about different types of UWB medical applications, it is good to understand the motivations and background of UWB research for these applications.

## **2.5. UWB Medical Applications**

### **2.5.1. Background and History**

Several specific features of the UWB system have made it a good candidate for medical applications. These features include high contrast between different tissues, good spatial resolution, adequate penetration, low power and simple system architecture. The first time that was in 1993 the UWB system were used in an application related to medicine, which was

human body monitoring. Three years later, in 1996, better description of UWB systems for biomedical application was presented, and at the same time, the US patent was awarded to McEwan [12]. Since then, UWB has been used for medical sensing and imaging. Several advantages of this technology over conventional imaging technologies like X-ray made it a perfect substitute for them. Since 1999, many medical imaging applications in cardiology, obstetrics, breathing pathways and arteries have been using UWB systems.

### **2.5.2. UWB Benefits for Medical Applications**

An important feature of UWB systems is their ability to penetrate obstacles because of using lower frequencies besides having high gain. On the other hand, Ultrasound as the conventional way to do imaging has problems with both obstacles and distance. The ultra-sound device must be placed at most of a few inches from the target because of its low gain and it should be in direct connection to the human body.

UWB systems which use sub-nanosecond pulses provide high precision at centimeter level. These narrow time-domain pulses also result in immunity to multipath transmission problem. Conventional techniques which employed continuous wave (instead of narrow pulses) for transmission and detection, had both of precision and multipath issues.

Regarding to FCC regulations, UWB pulses should not have power level more than -41.3 dB for indoor usage. As a result of this rule, UWB systems cause a very low electromagnetic radiation, which makes them suitable for a hospital environment. Also, since it has low electromagnetic (EM) radiation, it can be used over patient body several times without any danger.

Another important feature of UWB systems is their ability to work with a very low-power consumption due to the very narrow time-domain transmitted pulses. This will result in long life of battery-operated devices. Noise-like transmitted UWB signal makes it possible to deploy medical sensors with UWB since the signal is hard to detect and has excellent jamming resistance.

To summarize, every electrical or electronic device which is to be used for medical purposes should have some specific attractive features. Among them, UWB systems have several important features like non-invasiveness, low power, non-contact remote operation, biocompatibility, environmental friendliness. On the other hand, there are some other features needed for biomedical applications that require more research for

UWB systems require more research to achieve those. Some examples of these features are: user friendliness, “imaging” properties, technical understandability by the users, need to get physiological measurements, and improved sensitivity specificity.

### 2.5.3. Applications

Having briefly discussed UWB technology for medical applications, we can concentrate on some specific relevant details. Generally, there are two main approaches to use UWB in medicine: monitoring and imaging. The following sub-sections will contain explanations of each.

#### 2.5.3. a. Medical Monitoring

As discussed in above, UWB is an excellent choice for medical monitoring, examples of which include patient motion monitoring, vital signs of human's body monitoring and monitoring of medicine storage.

In patient motion monitoring, an alert for sudden infant, death syndromes and SIDS are a few of examples that are very important, especially in intensive care units. In addition, UWB systems are wireless, which result in avoiding many wires in unit around the patient. For rescue operations, UWB systems can detect any tiny motion under soil or any other obstacles due to their high gain and high penetration capabilities. An example of this kind of monitoring is the work in [13] and an example of their result which is shown in Figure2.10.

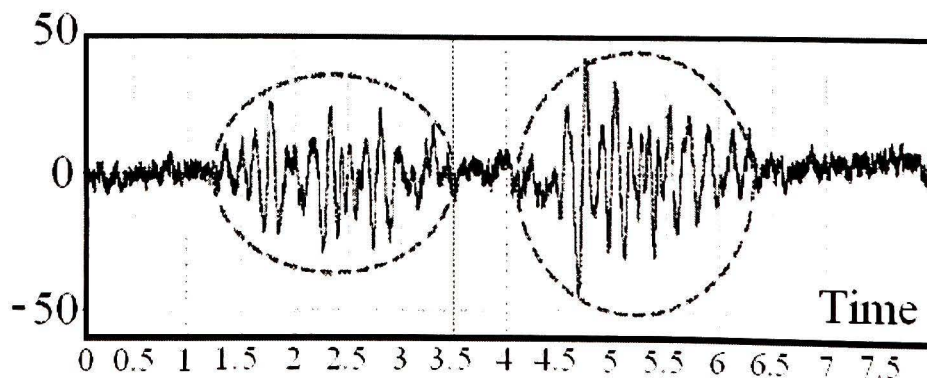


Figure 2.10. Detection of any movement in the room. [13]

Besides patient movement monitoring, UWB sensors are also able to detect internal movements within the human body. Again, this makes internal medical monitoring much



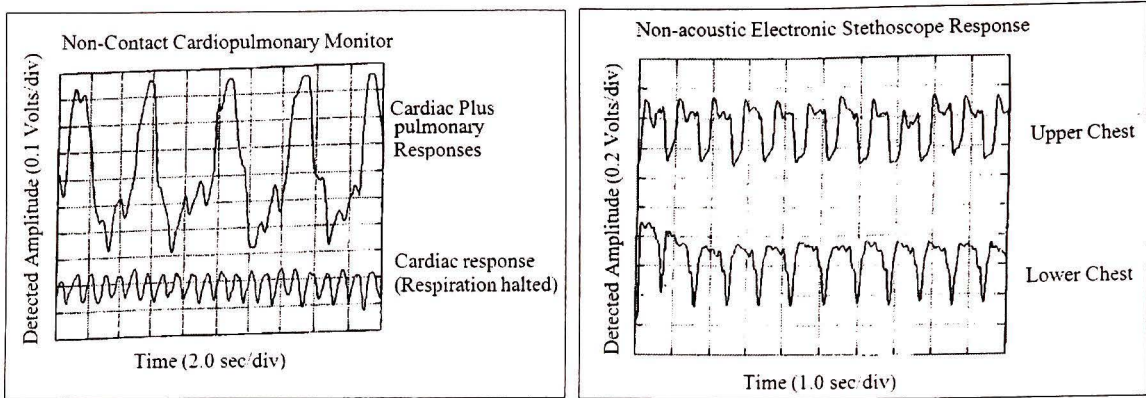


Figure 2.12. Images from McEwan's Patent (Patent No. 5,573,012) [12]

In addition to being of high-speed and low-cost, this radar system could monitor heart movements non-invasively, as shown in Figure 2.12. As demonstrated in Figure 2.11, UWB pulses are transmitted to the heart and the reflected pulses which come from heart are detected by receiver and can be recorded in memory. Then, signal processing is performed on received data, and from a comparison of the received pulses, heart movement can be detected. This can be done because the reflected pulses that come from heart muscles are considerably different from those reflected from blood.

The same technique can be used for pneumology applications. This is because the reflected pulses from different tissues are different enough to clarify boundaries between different human's body's organs. For example chest/lung, air/Chest interfaces and vessel boundaries are where we should focus to do better detection. Using an ultra wideband medical imaging system, it is possible to monitor the respiratory patterns. For example Apnea monitoring in infants, obstructive sleep apnea monitoring, polysomnography (sleep related studies), dynamic chest diameters measurement, allergy and asthma crisis monitoring, and chest imaging are all possible using UWB imaging.

Other important advantages of UWB medical imaging for fetal monitoring no contact with patient, unimpaired mother and child care, remote operation, no cleaning required, and easier use. Figure 2.13 shows the setup which is proposed in [14] for fetal monitoring. Due to above-mentioned benefits, it seems that it should have replaced conventional ultrasound imaging methods by now. However, since there is a public fear from electromagnetic radiation and its perceived danger to newborn infants, it takes more time for the present imaging systems to be replaced by its UWB counterparts.

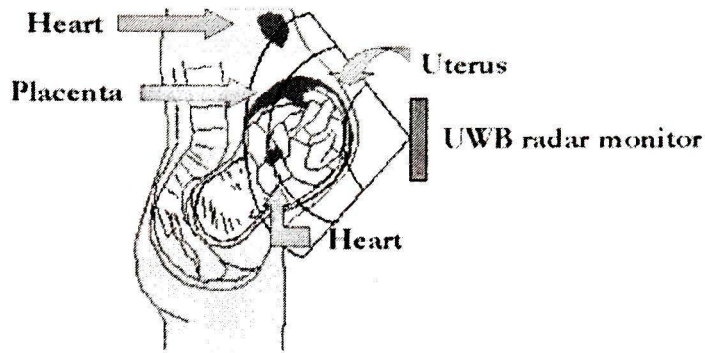


Figure 2.13 Obstetrics imaging using a UWB radar [14]

The final group of imaging applications is related to ear-throat-nose applications. Monitoring vocal chords movement using a UWB system is a typical application in this group. But more important applications in this group are detecting vocal diseases like inflammations, allergies and cancers in the vocal chords. In addition to both monitoring and imaging types of applications, there are new groups of application which are currently under active research [15].

- Underwater medicine measurements.
- Space medicine measurements.
- Sport medicine measurements.

Finally future studies for medical applications may be focused on,

- Ultrasound heart M-Mode tracings.
- External phonocardiogram and apexcardiogram tracings.
- External ballistocardiogram tracings.
- Invasive pressure pulse recordings.
- Electrocardiogram recordings.
- Better understanding and modeling of RF pulse propagation in the living tissues

#### 2.5.4. Medical Imaging for Breast Cancer

As it was explained in the previous section, one of the major groups of medical applications of ultra-wideband systems is medical imaging. Among various types of medical imaging applications, breast cancer detection is one of the most popular fields that attracted much research interest. In recent years, an increasing number of deaths due to breast cancer are reported. Only in United States, there is an average of 40000 deaths a

year because of this type of cancer [16]. Since curing this type of cancer or long-term survival of patients are highly dependent on early detection and timely medical intervention, a very precise and dependable imaging system is demanded in the treatment procedure. Conventional mammography has been done using X-ray imaging of a compressed breast for non-palpable early stage breast cancer. [17]. Through time, some technical advancement such as digital mammography plus radiological expertise have provided significant improvement of image quality and diagnosis using this method of medical imaging. Although generally, due to sensitivity issues of X-ray imaging, there are still many problems with relatively high false-negative rate of detection. [18]. In addition, low positive predictive rates resulted in many additional unnecessary biopsies [19]. Finally, in X-ray imaging, patients have to deal with uncomfortable or painful breast compression and exposure to low level ionization.

Usually Magnetic Resonance Imaging (MRI) and Ultrasound are needed to be used for verification of mammography detected lesions by X-ray. In these systems, the modalities are not yet sensitive/specific enough or are too operator dependent or are too costly to be useful for screening purposes. All of above limitations have led to efforts to find an alternative to X-ray mammography. One of the most promising alternatives is using microwave imaging using UWB systems.

Several different spectroscopy studies show that for the Radio Frequency (RF) and Microwave range of frequencies, differences in electrical characteristics of malignant and normal tissues is greater than 2:1. This is only one of motivating reasons that led to research on electromagnetic imaging at these frequencies.

Another interesting fact is that dielectric constant,  $\epsilon_r$  and conductivity,  $\sigma$ , change with increasing water content in neoplastic tissues due to increased protein hydration [20]. This fact will result in exploiting strong indicators of malignancy associated with physical or physiological factors of clinical interests such as water content, vascularization, blood flow rate and temperature. Compared to X-ray imaging, RF and microwave imaging has this advantage, which can somehow compensate for its spatial resolution which is not as good as X-ray imaging because of short wavelength of X-rays. In fact, high contrast exists for both high and low frequencies. At lower frequencies, contrast is due to breakdown of necrotic cell membranes which are being used for

electrical impedance topography [21, 22]. On the other hand, at higher frequencies we have high contrast due to increase in DNA, protein and hemoglobin absorption in malignant tissues [23]. Considering the above properties of different frequencies and after studying parameters which are important in an imaging procedure, it has been concluded that the frequency range between 1 to 10 GHz is the optimum band for this application. The reason is that this band is a range that includes both advantages of having high spatial resolution which is better at higher frequencies and also better penetration depth which is better for lower frequencies.

At present, it is known that why microwave imaging is a promising substitute for conventional mammography. It is also known what frequency range should be used for imaging.

From this perspective, there have been two main techniques for active microwave imaging\_radar and tomography. Both techniques are based on the dielectric contrast in this range of frequency. In both techniques, low-power microwave signals are transmitted from an array of antennas into the breast. The tomographic image reconstruction technique is the most commonly attempted technique in this frequency range that can be done using narrow band signals. In this technique we need to solve an image reconstruction problem which needs regularization and some other techniques so that it can converge and have a meaningful solution. However, many of these concerns are minimized in smaller cases like that in breast cancer detection.

On the other hand, we have UWB radar in which we are not trying to reconstruct the complete profile of dielectric properties of the breast. In fact, in this technique, we try to find the presence and location of where we have significant backscattered energy due to difference in dielectric properties of normal and malignant tissues. In general, the microwave frequency domain for breast imaging is associated with some features that we expect from UWB system as an imaging systems working in this range of frequency.

1. Significant contrast between dielectric properties of normal and malignant tissues in this frequency range. In normal tissues of the breast, microwave attenuation is low enough that we can image the entire breast.
2. Avoiding breast compression as well as using low-power signals results in little health risk.

3. Conventional microwave tomography has computational challenges. Using space-time UWB imaging, we can overcome these problems and obtain a very good three-dimensional picture of the breast.
4. Using space-time UWB imaging systems, we can expect a precision of less than 0.5 cm which is good enough for early detection and location of breast cancer.
5. Finally, UWB microwave imaging is able to detect if the lesion is malignant or benign. For benign lesions, the dielectric properties are not different from normal tissues as much as they are for malignant lesions. As a result, the scattered waves are not as strong as it is for malignant tissues.

# Chapter 3

---

## UWB Systems for Medical Imaging Applications

---

Due to the very wide bandwidth that is used for ultra-wideband (UWB) systems, there is some confusion between ultra-wideband systems and conventional spread spectrum technologies. In fact, there is a significant difference between basics of data transmission between these two types of communication. Briefly, the difference is that for UWB, we use ultra-short time domain pulses for data transmission whereas for spread spectrum systems, information is transmitted on a modulated continuous carrier signal. In fact, for UWB systems, we use a time-domain modulation scheme like that used in impulse radio ultra-wideband (IR-UWB) systems which is time hopping pulse position modulation (TH-PPM). In addition, UWB systems usually occupy a greater bandwidth than spread spectrum systems.

When we compare UWB systems with conventional spread spectrum systems we can make the following observations.

1. The UWB transceiver architecture is generally much simpler than in conventional radio systems. This is because we do not need some functional components such as modulation and demodulation circuitries which result in more complexity.
2. As mentioned earlier, transmission power is lower than in conventional systems making power consumption in UWB systems lower.
3. Since a UWB system has a very large bandwidth, the possibility of unintended detection by strangers is low.
4. Unlike conventional radio systems, a bit rate of more than a few hundred Mbps is achievable in UWB systems.

### 3.1. UWB Transceiver Basic Architecture

Generally UWB systems are being used for short-range low-power systems. Typically, they use TH-PPM as their modulation scheme. As mentioned previously, one of the key advantages of these systems is their simple architecture. Figure 3.1 shows a block diagram representation of a typical transmitter of UWB system.

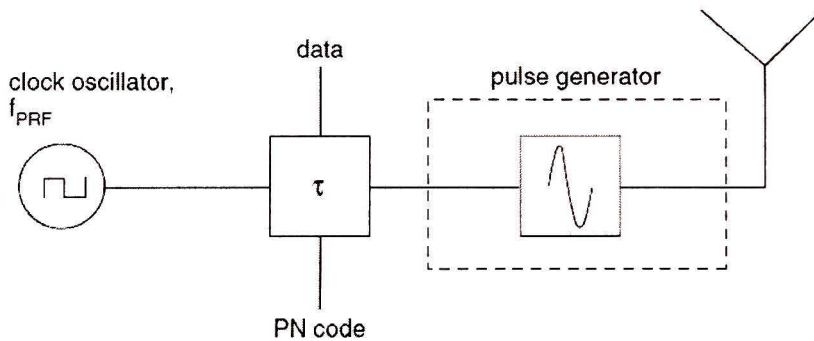


Figure 3.1. Typical transmitter of a UWB system [24].

As it is shown here, there are only three blocks used for this transmitter. The first block is clock oscillator that is used to determine the pulse repetition frequency (PRF). There are two options\_ crystal oscillator and custom design oscillator, for this block. The former one is more feasible for high-frequency systems such as impulse radio. The second block is a digital timing circuit which is basically designed to provide a trigger signal for the pulse generator. In some special cases, this block can be replaced by a digital delay controller. Finally, we have the pulse generator which can form the pulse to be transmitted.

The properties of ultra-wideband width and using narrow pulses for communication, results in no need for complicated circuits like power amplifiers and frequency synthesizers which includes blocks like phase locked loops (PLLs), mixers and voltage controlled oscillators (VCOs). These are among the most complicated blocks used for conventional continuous wave transmission systems. Not having these complex components makes the transmitter architecture of UWB systems inexpensive, simpler to design and simpler to implement, when compared to conventional radio systems.

Regarding the work by Proakis et al in 1995 [26], the optimal receiver for a signal transmitted in an additive white Gaussian noise (AWGN) channel is a correlation or a matched filter receiver which makes SNR(Signal to Noise Ratio) maximum.

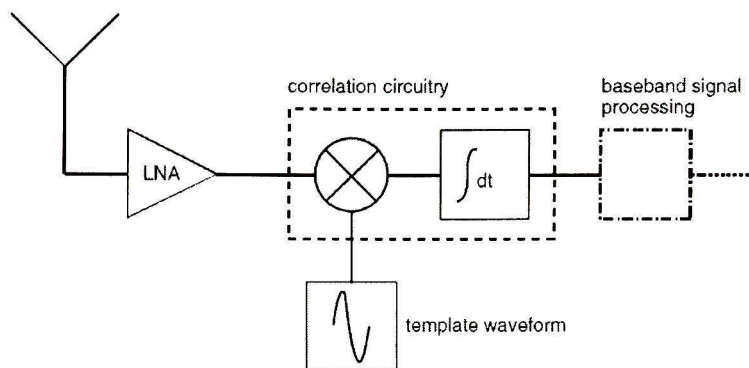


Figure 3.2. typical basic structure of a UWB receiver [24]

Figure 3.2 shows a receiver architecture that is made of three major blocks\_ low noise amplifier (LNA), correlation circuitry and a block for providing template waveform for correlation circuit. In addition, of course after the major blocks of receiver, we have the baseband signal processing unit in which the decision-making and other processing tasks are performed.

The first step in signal detection is to amplify the received signal. Since the received signal from the antenna is fairly noisy and weak, then the first stage of receiver, which is responsible for amplification, must be very low-noise. Also, since this block is connected to the antenna, it should be perfectly matched to the output impedance of antenna, which is normally  $50 \Omega$ . After amplification, there is the correlation block in which received and amplified signal are compared to the template waveform and its result determines the data carried by received signal using baseband signal processing unit.

One of the most important issues in the receiver design is to generate the template waveform for the correlator block. In fact, we need to make this waveform as similar to received signal as much as possible, so as to maximize signal-to-noise ratio. Making this waveform the same as the received signal is a very complicated task, and it makes the receiver circuit very complex.

To avoid this complexity, we have following options. One way is to approximate the received waveform by the transmitted signal. Second way is a coarse approximation like

a rectangular wave, which is very simple to generate but is not very efficient. Another way, which is proposed by [27] is to ignore the template waveform and to rely on the finite bandwidth of transmitting and receiving antennas, which result in a specific pulse shaping. Another fact that can help us in generating the template waveform is that both transmitting and receiving antennas work as differentiators. As a result, in ideal condition, the received signal in the receiver must be the second derivative of transmitted signal. In our case, this would be the third derivative of a Gaussian pulse.

In [24], the auto-correlation of the first and second derivatives of a Gaussian pulse are compared. Also, the cross-correlation of the first and third derivatives of this pulse is compared to the auto-correlation results. The result in Figure 3.3 shows that the cross-correlation result is almost 80% of third derivative autocorrelation. This means that if we use the transmitted pulse as the template waveform, we will only have a loss of less than 1 dB, which is quite reasonable.

After generating this template waveform it will be sent to the correlation circuit. As shown in Figure 3.2, correlation circuit consists of a multiplier and an integrator. The multiplier's task is to multiply received and template waveforms, and its result will then be integrated over the bit duration to maximize the received signal power and minimize the noise component.

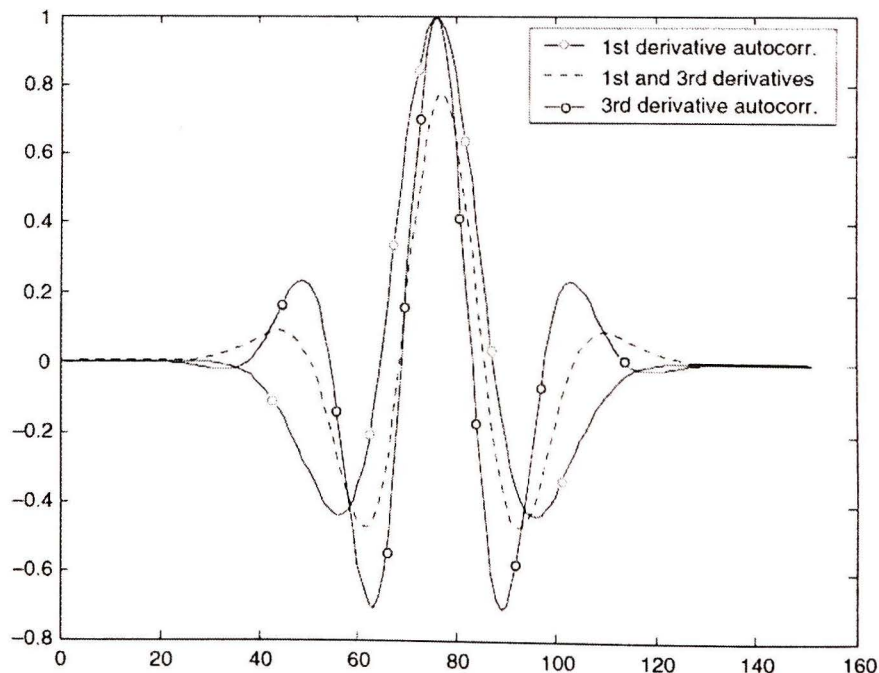


Figure 3.3. Correlation results of transmitted and received signals [24].

Consequently, if we have a pulse train, the integrator's result should be higher than the noise level and the desired signal can be detected and separated from noise or other unwanted signals. Another issue in the design of the correlator is the speed of multiplying and integration, which must be designed carefully so that it will be synchronized with other parts of the system.

In the paragraph above, the basic architecture of a UWB system was introduced. Of course for different types of applications, different sections of this architecture might change in different sections. For example, most UWB systems use time-hopping pulse position modulation (TH-PPM) or some other time-domain modulation schemes which should be considered in the transmitter architecture. Also the correlator structure is not always as simple as explained here, and it might change due to the needs of the specific system.

## **3.2. UWB Technologies**

In this section, we will review different architectures which are used for UWB communication applications. We will focus on the following major topics\_ waveform generation and implementation, data modulation and correlation receiver. Four different technologies including Pulse On technology, sub-carrier technology, multispectral solution and Xtreme Spectrum inc. will be described in this section. It is worth mentioning that first two technologies belong to Time Domain Corporation.

### **3.2.1. Pulse on technology**

This technology, from Time Domain Corporation, believed to be the most popular technology used in UWB communication systems. The main block diagram of this system is shown in Figure3.4.

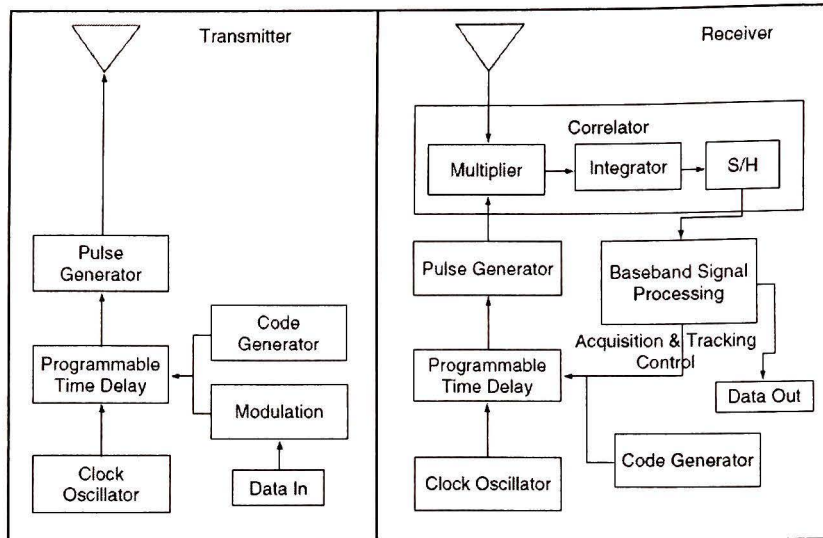


Figure 3.4. block diagram of a typical transmitter and receiver for UWB technology [24]

As shown in Figure 3.4, we see that transmitter architecture has some variations from the basic transmitter configuration which was described in the previous section. From top to bottom, first, we have a transmitting antenna whose task is clear. This antenna is fed by pulse generator block which forms the required pulse shape (i.e. Gaussian monocycle) to be transmitted. Then, we have a programmable time delay block which is responsible for timing of the pulse transmission. This block gets its timing signal from a clock oscillator, which is normally a crystal oscillator. Also, there is another input for the PTD (Programmable Time Delay) block, which is its control signal. This signal comes from output of two other blocks namely, code generator and a modulator. The modulator block receives input data and applies the requisite modulation scheme. Its output, together with the individual pseudo random code which is generated by code generator, are fed into a programmable time delay. Since the system is designed to have low transmitted power, power amplification is not needed, so a simpler topology is used.

In the receiver block, we have the correlation technique to receive signal. As explained in previous section, this is the optimal technique to have the maximum signal-to-noise ratio. In the correlator, we have a multiplier which multiplies the signal with a template waveform. This waveform is generated based on the transmitted signal. As we see in Figure 3.4, the same blocks with the same functionality in transmitter are used to make the same waveform generated in transmitter.

Following the multiplier, we have the integrator which integrates the result of the multiplication over the bit duration, which is the addition of several periods of the received pulse train. After this stage, the output signal is in baseband and it can be sent to the signal processing unit to make decisions and other necessary process. After the signal processing stage, there is a feedback to the template waveform generation blocks. This is responsible for monitoring the final data and apply any required corrections to make the data more meaningful.

### 3.2.2. Sub-Carrier Technology

This technology was also invented by Time Domain Corporation. Its main application is to utilize more channels or transmit different information simultaneously with one system. The main idea is to provide more possibilities for channel coding and signal modulation.

In this technology, we have approximately the same block diagram that was used for the Pulse On technology. The only change is the way we provide the control signal for the programmable time delay block. Figure 3.5 shows how the signal is generated and provided for this block.

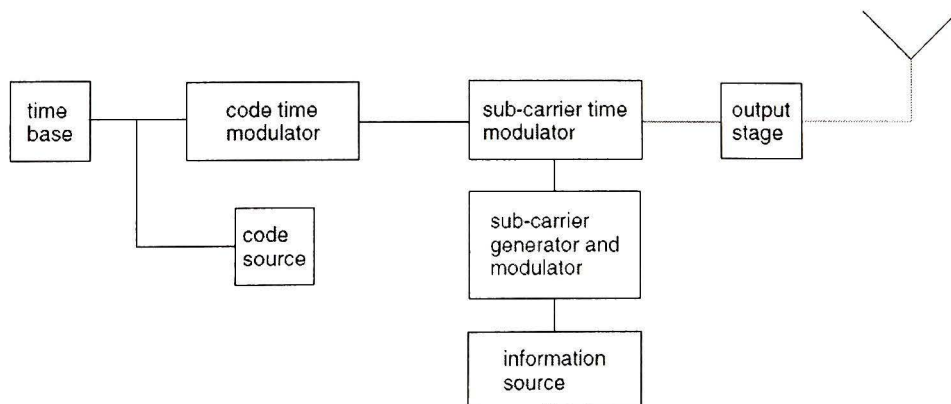


Figure 3.5. Control signal generation for PTD block in sub-carrier technology [24].

As shown in Figure 3.5, the “time base” block and the “code source” provide inputs for code time modulator. Here “time base” is in fact a clock oscillator which determines Pulse Repetition Frequency (PRF). Also the code source is responsible for providing code to be an input for the code time modulator. The output of the code time modulator is a coded timing signal from the PRF source. On the other hand, we have an information

source which is fed to the sub-carrier generator and modulator. This block's task is to generate a sub-carrier signal and then modulate it with information signal to make the modulated subcarrier signal. Finally, the result of this block will be sent into the subcarrier time modulator to be modulated by the coded timing signal which was generated from the other path. The output of this block will then be sent to the programmable time delay as the control signal. The rest of this technology for both transmitter and receiver is same as Pulse On technology.

### 3.2.3. Multi-Spectral Solutions

In this technology, which was created by Parkway in 2001 and belongs to Multi-Spectral Solutions, we have three methods to generate the desired pulse. These methods can be classified into two groups. The first group includes two schemes and the third scheme will be under the second group.

In the first scheme which is shown in Figure 3.6.1, we see that an oscillator generates the input signal based on a preferred phase and frequency which is given.

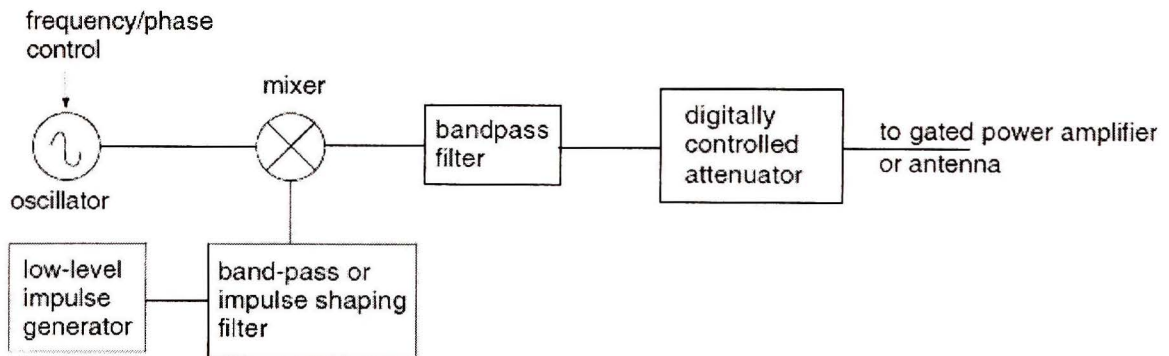


Figure 3.6.1. First scheme of pulse generation in Multi-Spectral Solutions Method. [24]

Also, as we see from the above diagram, an impulse generator makes an impulse which will be shaped through the band-pass or impulse shaping filter and its result will be sent to mixer which is designed to “chop” the signal coming from oscillator to provide a pulse train for the next blocks. This train of pulses will be sent to a band-pass filter so that we can choose desired frequency and bandwidth for the transmitting signal. Since there is no need to generate the derivative of the signal, this transmitter architecture is relatively simple, but on the other hand, it is relatively expensive because the very short impulses means that very fast switches and digital signal processors are needed.

The second scheme of first group is in fact a special case of first scheme where we have zero oscillator frequency (e.g. dc source). In this case we can eliminate this block and also get rid of mixer. This scheme is shown in Figure 3.6.2.

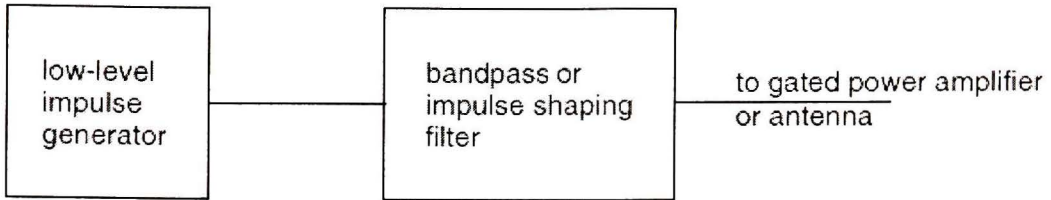


Figure 3.6.2. Second scheme of pulse generation in Multi-Spectral Solutions Method [24].

The second group of pulse generation scheme in this technology is shown in Figure 3.6.3.

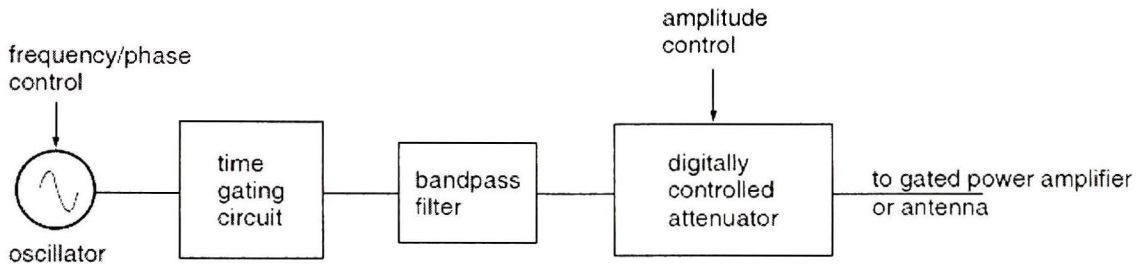


Figure 3.6.3. Second class of Multi-Spectral Solutions' pulse generation schemes. [24]

As we can see in this figure, the impulse generator and impulse shaping and band-pass filter, as well as the mixer which were used in first group, are now replaced with a timing circuit. In this scheme, the oscillator makes the input signal with the desired frequency and phase, and propagates this signal through the timing circuit. The timing circuit provides time frames so that the generated signal by the oscillator can pass through these frames. As a result, the output of this block would be an amplitude modulated signal made of the oscillator output which will be sent to the subsequent circuits.

### 3.2.4. Xtreme-Spectrum: Trinity

In this technology, which was created by McCorkle in 2001 and belongs to Xtreme-Spectrum, the transceiver's architecture consists of an interface and three other parts including a transmitter, a receiver and a radio controller. Basically, the architecture that we have in this technology is very similar to what we explained in previous sections, so it will not be explained again. On the other hand, a novel idea is proposed for pulse generation. In this idea, first, we need to generate two short pulses in which each one has

a pulse-width equal to half of desired monocycle length. Then, these pulse will be sent to a mixer such as a Gilbert cell, to be mixed to make a monocycle signal, as shown in Figure 3.7 below.

As shown in this figure, this method is able to produce both types of monocycle. This is done by a decision bit which will be applied to mixer as an input so that it will determine that the first half-cycle must be negative or positive based on its value.

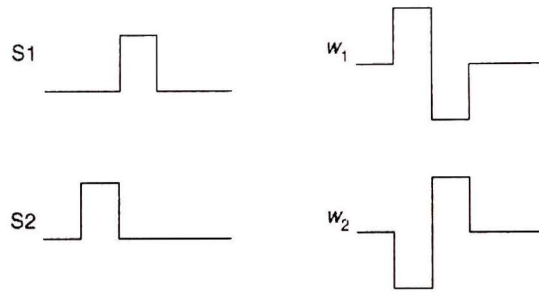


Figure 3.7. Primary and final pulses in Trinity pulse generation method [24].

### 3.3. UWB Circuit Implementation

Having discussed the basic architecture of a UWB imaging system, we can now go through the design of each block individually. In the next two Chapters, the design of two most important blocks of receiver-the ultra-wideband Low Noise Amplifier (LNA) and the UWB Mixer (or multiplier in this case) will be presented and discussed. As a result, we will not describe their design here. Other than these blocks, there are a few important blocks which are necessary for all of different transceiver architecture. In this section, we will describe the design basics of these blocks so that we will have better understanding about the circuit blocks that the LNA and Mixer will work with.

#### 3.3.1. Pulse Generator

This block may be the next important block of a transceiver after the LNA and the Multiplier. The pulse which should be generated for this system should satisfy FCC power requirements for UWB signal. As long as it can satisfy these requirements, it can be any kind of pulses including Gaussian, Laplacian, Rayleigh or Hermitian.

The FCC mask for UWB indoor devices is shown in Figure 1.3. In almost all of UWB systems for medical imaging, a Gaussian pulse is used for the UWB pulse. Such a pulse

can be generated in several different ways, and each way has its own advantages and disadvantages. One way proposed by McCorkle et al [24] was described in section 3.2.4. In this section, we discuss a few methods to generate such a pulse and we focus on methods that can be used for the TH-PPM scheme.

Unlike McCorkle's technique which needed a multiplier, there are other methods with simpler architectures that are usable by PPM. One method, proposed by Tiuraniemi in 2002, generates two short pulses with a specific delay which is equal to desired pulse width in a first step. Then these two pulses are subtracted from each other using an analogue subtractor, result in a monocycle in the second step.

The top level architecture of the pulse generation in this method is shown in Figure 3.8. As we see in this figure, two identical and parallel pulse generation blocks are generating short pulses. These pulses are generated with a pre-determined delay which is shown by a block named as  $\tau$ . This block can be made using two inverters and a PMOS varactor which gives us the ability to tune delay time accordingly.

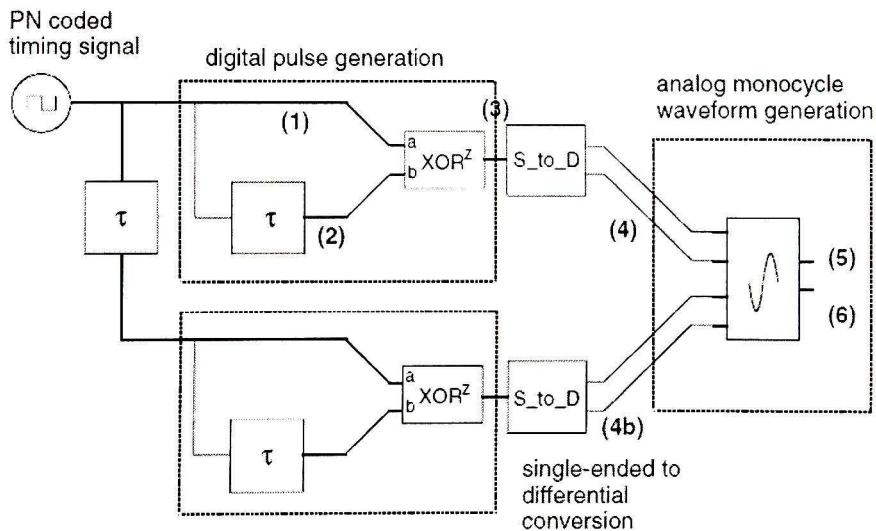


Figure 3.8. Top level design of pulse generation architecture [24].

The output of short pulse generators will be sent to two single-to-differential converter and then the result of these blocks will be sent to to analog subtractor which plays the role of analog monocycle waveform generator. Figure 3.9 shows the waveforms of different nodes of this system with the same numbering used in Figure 3.8.

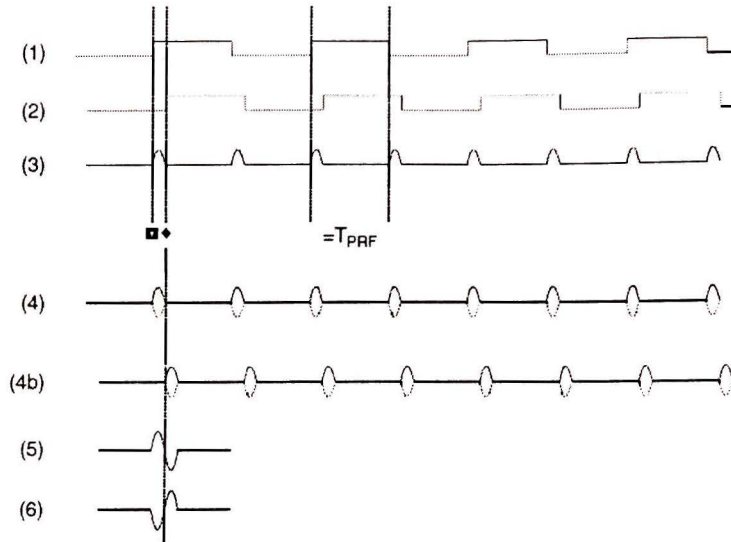


Figure 3.9. Waveform in different phases of monocycle generation presented in Figure3.8 [24].

Now that we know the top level design of the pulse generator we can study each block individually. To design pulse generators, different circuit techniques can be used. As an example, Figure3.10 shows how an XOR gate can be used for pulse generation.

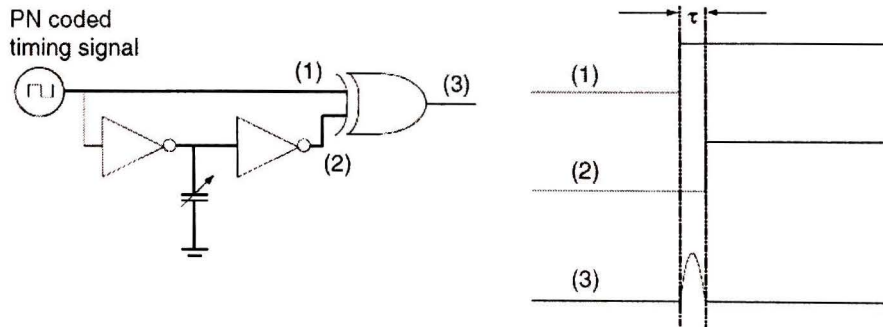


Figure 3.10. Using XOR gate for pulse generation [24].

As we know from XOR logic, the output of this gate is a logical “1” if the two inputs are in different logical levels. It is zero if both of them are either logical zero or one. Here, two inverters and a varactor play the role of a delay block. This is the same configuration that we use for the delay block between two pulse generators. Using two series inverters means that the output has the same logical level as input. The only difference is that each of the inverter gates has a delay because of the finite time it takes for the gate to change state from “0” to “1” and vice versa. This delay is also related to the capacitance at the output node of the inverter. This is why we put a varactor at the output node of first inverter. Using this varactor, we can easily determine length of delay we want. Using this

delay block, we can have different inputs to the XOR gate for specific period of time which is desired for output pulse width.

Figure 3.11 shows the method in which we can use an AND gate as the pulse generator for our system.

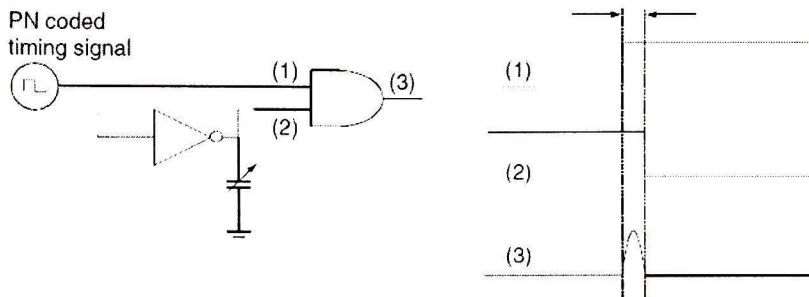


Figure 3.11. Using AND gate for pulse generation. [24]

Again, we know that the logic state of the AND gate is a logical one if both inputs are one. Here, since the second input of the gate is an inverted version of first input, it seems that the inputs have always different logical levels, so the output is always zero. But if we look at the circuit carefully we can see that there is a delay for the inverter which can be controlled using the varactor. As a result, on the positive edge of the timing signal, since it takes some delay for the other input to change its logical level, we have both of inputs in level “one”, and as a result output is “one”. This situation is called a glitch or hazard, and the length of the glitch can be conveniently determined by varactor. Also, we should be aware that when we use an AND gate, the pulse repetition frequency (PRF) will be half that for XOR case since we only have a pulse on one of edges (positive edge). However for XOR we have a pulse on both rising and falling edges.

The other gate that can be used in pulse generation is a NAND gate. Its functionality is very similar to the AND gate. The only difference is that the pulse occurs in falling edge, and because of its architecture, it operates faster than an AND gate. This is why in many cases, we use NAND instead of AND for pulse generation.

The next step is to send the output of the digital pulse generators to single-to-differential converters. These blocks then generate two identical out-of-phase pulses from each input pulse so that we will have two pair of differential pulses with a specific delay. One example of single-to-differential converter is shown in Figure 3.12. two circuits was made by Gilbert in 1997 as a mini-mixer.

In Figure 3.12, the AC-coupled signal will be applied to the gate of the differential pair and since  $M_{01}$  is diode connected, it functions as a resistor in ac small-signal analysis.

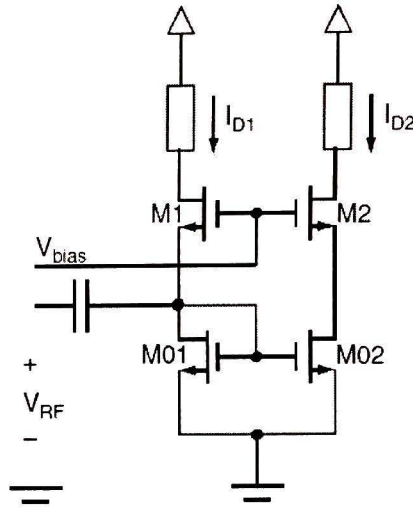


Figure 3.12. A single ended differential converter [24].

Also, we have a transconductance stage for  $M_{02}$ . This results in a  $180^\circ$  phase shift between its gate voltage and its small-signal drain-source current. Drain currents of these transistors, which are now out of phase, will be mirrored to the drain current of  $M1$  and  $M2$  with the same phase. Then they will be converted to voltages across the resistors. The voltages dropped across the resistors are in fact two pulses which have  $180^\circ$  of phase shift. Finally, the results of these single-to-differential converters will be sent to the analog waveform generator.

Prior to explaining about the analog waveform generator, we introduce the analog subtractor. Figure 3.13 shows a sample analog subtractor. In this circuit, the drain nodes of differential pairs are connected to each other in a cross-coupled way, therefore, we can write the following equations for their currents.

$$\begin{aligned} I_{out} &= I_{D5} - I_{D6} = (I_{D1} + I_{D4}) - (I_{D2} + I_{D3}) \\ &= (I_{D1} - I_{D2}) - (I_{D3} - I_{D4}). \end{aligned} \quad (3.1)$$

$$I_{out} = KV_1 \sqrt{\frac{2I_{SS}}{k} - V_1^2} - KV_2 \sqrt{\frac{2I_{SS}}{k} - V_2^2}$$

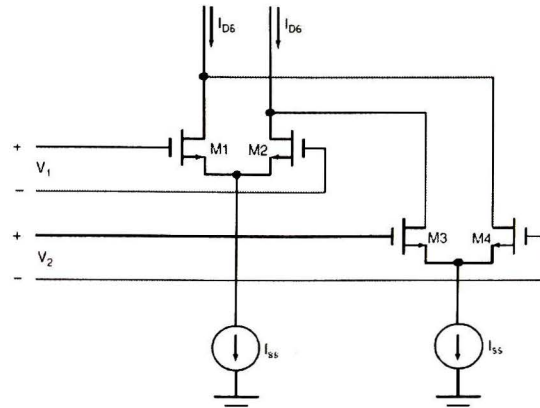


Figure 3.13. Analog subtractor [24].

$$I_{out} = KV_1 \sqrt{\frac{2I_{SS}}{k}} - KV_2 \sqrt{\frac{2I_{SS}}{k}}$$

$$\Rightarrow I_{out} = (V_1 - V_2) \sqrt{2kI_{SS}}. \quad (3.2)$$

two equations above, are valid for the case we have following condition and also transistors work in linear region:

$$V_1^2, V_2^2 \ll \frac{2I_{SS}}{k} \quad (3.3)$$

As seen from the above equations, finally, we have the output current as a function of the difference between input voltages. This means that the circuit works as a subtractor.

Having introduced the subtractor block, it is now easier to understand the monocyte waveform generator.

Figure 3.14 shows the final block of the monocyte pulse generator which is based on the subtractor. The differential pairs can be made using either bipolar or FET transistors. In the bipolar case, we will have a supposedly faster circuit, but with higher power consumption and occupying a large area. Also, for loads, we can use either active or passive loads. Active loads are harder to make, but they occupy less space. This makes active loads suitable for very large resistors since they only occupy a small piece of the semiconductor. On the other hand, active loads usually have very poor performance at higher frequencies and cannot be used at those frequencies if we want a good precision.

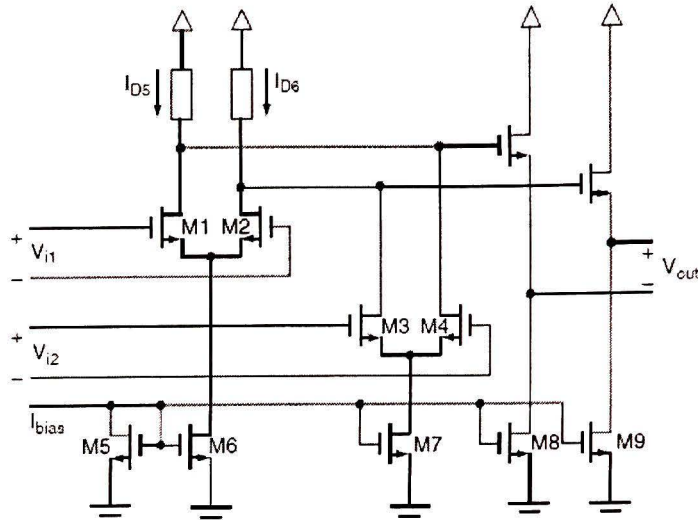


Figure 3.14. pulse generator's analog subtraction circuit [24]

### 3.3.2. Correlator

The next important block in the transceiver design for UWB systems is its receiver's correlator. This block, which was described previously, is usually a complex of different blocks. In addition to different optional blocks like amplifiers, attenuators and filters, almost all correlator circuits have two main important blocks\_ a multiplier and an integrator. As mentioned before, for the multiplier we will devote an entire Chapter to describe its design and related challenges. The other block is the integrator which is described here. The main task of the integrator is to integrate the output of the multiplier for a train of pulses. Then it sends the integration result to a comparator so that it can make a decision about the bit's logical level. As shown in Figure3.15, which demonstrates an integrator that can be used for a UWB imaging system's correlator, there are two major parts\_ integrator and integrator/holder. The first integration stage is made of a differential pair in which the drain terminals are connected to two ends of a capacitor. The function of the capacitor is to integrate output current of this differential pair.

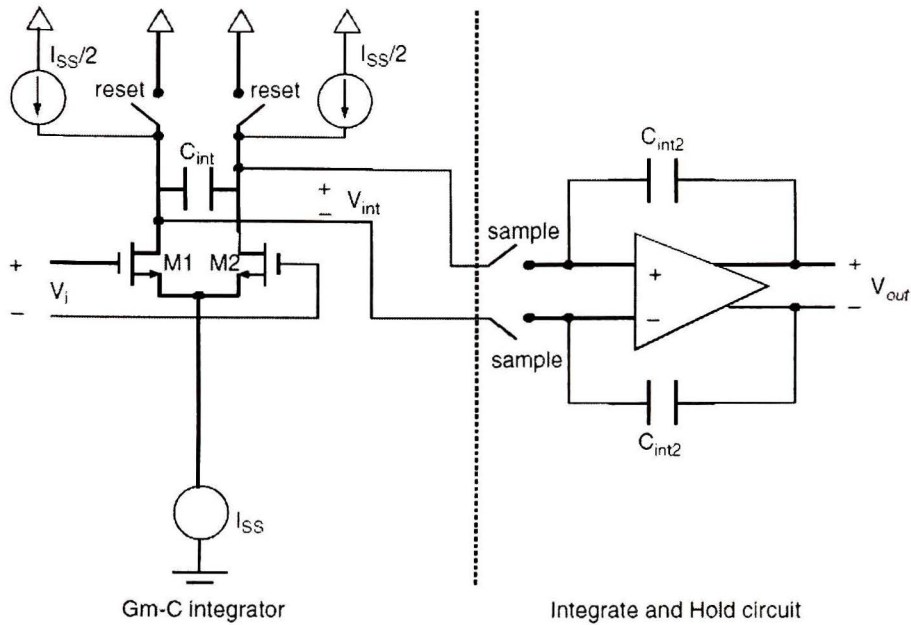


Figure 3.15. Integrator schematic which can be used in the body of correlator in UWB receiver architecture [24]

Based on the circuit schematic in Figure3.15 we can write,

$$V_{int} = \frac{I_{out}}{sC_{int}} = \frac{G_m V_i}{sC_{int}}$$

$$\text{and } \omega_{ti} = \frac{G_m}{C_{int}}. \quad (3.4)$$

Here  $V_{int}$  is the output voltage of this integrator, and  $I_{out}$  is output current of differential pair and  $C_{int}$  is capacitor which is used for integration. In this stage, there is also a pair of switches to reset the integration process. In fact, before starting the integration process, these switches will be closed so that both ends of the integration capacitor will have same voltage, and as a result the capacitor will be discharged. After a long enough period of time for the capacitor to be completely discharged, the switches will be open and the input voltages will be applied to the gate of the differential pair. These transistors will play the role of transconductance, and if input voltages are different, it will result in a difference in drain currents and consequently, a voltage will be dropped across the capacitor which can partially charge it. Since the capacitor's value in this stage is limited, it will be charged fully after several pulses, and after that, we will not have any information about the next pulses. As a result we need to store information in a place with a large capacitance. This is why we need second integration stage. The reason that we can not use only the second stage is that it is not fast enough to integrate very short

pulses of a UWB system, but it is fast enough to integrate the signal which is coming from the previous integration stage. As a result, we have a trade-off here between speed and capacity. The first stage has the speed with low capacity, and the second stage is opposite. The voltage difference between the differential inputs of I/H stage (which are the output of the first integration stage) will be fed by the operation amplifier which acts as switched-capacitor inverting integrator. It should be mentioned that the opamp should have very wide bandwidth so that it will be able to process the output of the first integrator. Finally we have Figure 3.16 which shows the schematic of a correlator that can be used for a UWB receiver system. As shown, this correlator has a Gilbert-cell multiplier as the first stage and an integrator as the second stage.

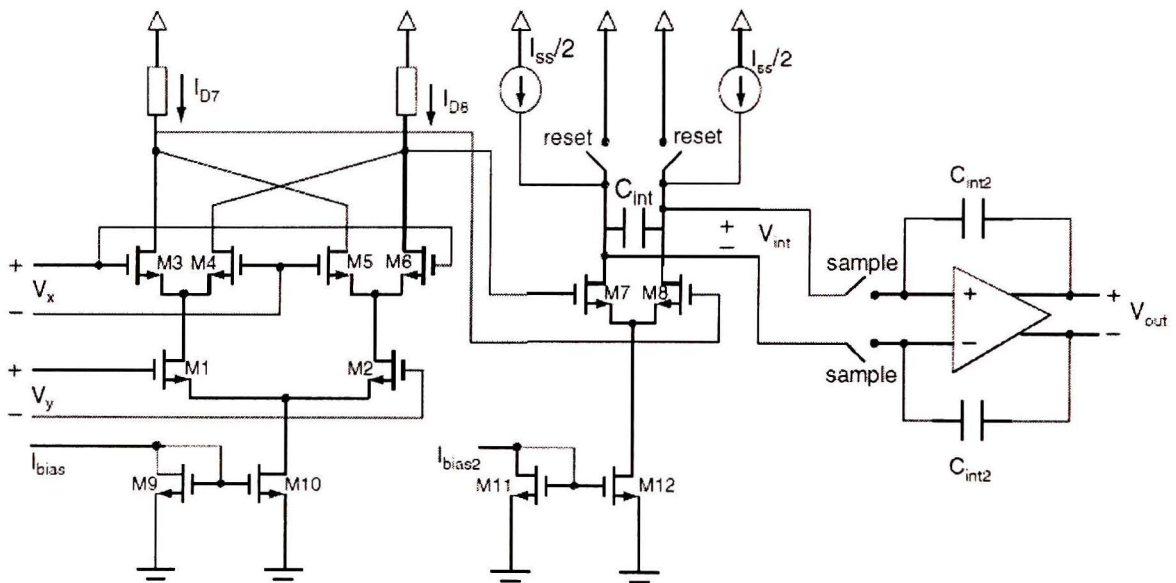


Figure 3.16. Correlator which is used in UWB received design [24].

### 3.4. UWB antennas

The antenna is an important component both for the transmitter and the receiver of a UWB system. Therefore it is useful to briefly discuss antennas which are used in these systems. In fact, as an integrated circuit (IC) designer, we do not need to know many details about design of antennas. However, since these components are in direct connection with circuits that we will design, it is beneficial to know some detail about them. Usually, UWB antennas act as filters for the transmitted signal [25]. Also, as

mentioned previously, in the sample waveform generation for the receiver we can consider the antenna as a differentiator in our design. In this section we briefly describe different requirements that an antenna should have if it is to be used in a UWB system for indoor applications. After that, some types of antenna types that can be used for this application will be described.

### 3.4.1. Antenna Characteristics

In this section we describe different characteristics of an antenna that is suitable for UWB applications. First, as mentioned before, UWB antenna take derivative of a signal passing through it. Besides that, a UWB antenna will result in a spreading signal in time domain, which will result in reducing time resolution for the entire system [28]. Generally, we should remember that antennas have more effect on the signal in UWB systems than in narrowband systems. This is because the UWB signal has a relatively wider bandwidth compared to narrow-band signals.

In antenna terminology when we call an antenna a UWB antenna, it means that we have ratio of 6:1, which means that highest frequency of antenna bandwidth is six times large than the lowest frequency. For this wide range of frequency, we should expect difficulties with impedance matching, radiation efficiency and linearity.

Another major difference between a UWB antenna and a narrowband antenna is an effect called “ringing”. Basically, for narrowband signals, since the pulse is not short in time, it will have almost the same shape after passing through the antenna. On the other hand, for UWB systems, since the pulse is very short in time-domain, after passing through the antenna, it will to some extent, lose its original shape. A typical example of this occurrence of ringing is shown in Figure3.17. As we can see in this picture, we have an unwanted signal following original signal for a period of time which is long compared to the pulse width.

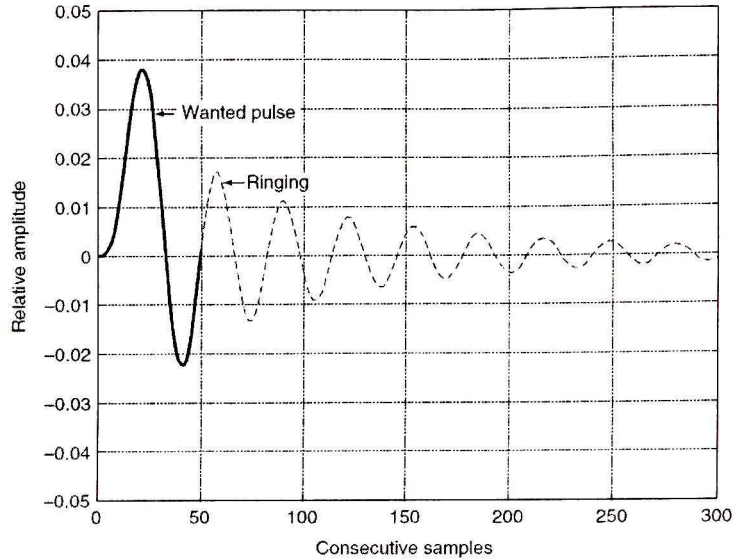


Figure 3.17. Ringing effect of antenna for UWB systems [24].

To avoid such an effect, one solution is to use low-Q, resistive antennas. Being resistive, will cause a strong attenuation and as a result, ringing will disappear faster. Also, since Q has an inverse relationship with bandwidth, lowering this parameter will result in wider bandwidth and consequently lower ringing effect. Although the drawback is that lowering Q will result in lowering antenna efficiency which results in other problems. It should be mentioned that the Q-factor of an antenna is defined as

$$Q = \frac{f_0}{f_H - f_L} \quad (3.5)$$

Here  $f_0$  is center frequency and  $f_H$  and  $f_L$  are higher and lower -3-dB frequencies of antenna bandwidth.

Finally a major difference between narrow-band and UWB antennas is that for the narrow-band case, we usually have a resonating antenna which is designed to resonate at a desired frequency. Therefore, these antennas have a narrow bandwidth. On the other hand, since UWB antennas need to be able to transmit and receive signals for a very wide band of frequency, they should not resonate at any frequency within the band, so basically, we need them to be non-resonating antennas.

There are other characteristics of antennas such as fidelity and symmetry which are important during design procedure. Fidelity means the maximum cross-correlation of the normalized incident voltage and the normalized electric field in the far-field region [29]. Also, the symmetry is a measure of the symmetry of the waveform in the far-field region

[29]. In the literature, we see different antennas which have been used for UWB applications. Here, in this Chapter, we will go through these types of antennas individually.

### **3.4.2. Antenna types**

Generally a UWB antenna either base-station or indoor-portable application should behave like a high-pass filter in frequency domain so that short sub-nanosecond pulse can pass through them without a serious change in shape. As a result of acting like a high-pass filter, we can conclude that they will act as a differentiator and the transmitted signal would be the derivative of input the signal.

Also, UWB antennas should be linear in phase as well as having a fixed phase center. Since most of the available impedance matching circuits are not linear in phase, then the antenna should be designed so that it is inherently matched. Also, the radiation characteristic of the antenna is a very important parameter in its performance. The antenna's gain should be smooth over its bandwidth so that there is no dispersion of the input signal. Also we should consider that antenna gain differs when we change the angle of receiver.

In addition to the general requirements described above, there are a few other requirements for each group of base-station or indoor-portable antennas. For example, base station antennas can be used both for indoor and outdoor applications, and generally, those which are designed for outdoor applications can be designed relatively large. Another important requirement for base-station antennas is that the radiation efficiency is very important and as a result, resistive load cannot be used. Finally, these antennas can be designed either directional or omnidirectional.

On the other hand, we have indoor-portable antennas in which the size is relatively smaller than base-station antennas, and usually, we like such antennas to be low cost. Also, if the antenna is constructed on a printed circuit board (PCB), it is more desirable. Since the antenna is small, we can conclude that it is omni-directional. Moreover, here we do not have strict sensitivity on radiation efficiency requirement and as a result, using a resistive load is allowed. A summary of a UWB antenna's requirements for both groups is presented in table 3.1.

Table 3.1.  
UWB Antenna Requirements [24]

	Base Station Antenna	Portable Antenna
Frequency Matching	2-10 GHz typical VSWR < 1.5 VSWR < 2	3-10 GHz typical VSWR <2 VSWR <3
Minimum Radiation Efficiency	50%	10%
Typical Directivity	0-30 dB	0 dB
Typical Fidelity	> 0.7	> 0.7
Size	not specified	area < 100 cm <sup>2</sup> on PCB
VSWR is voltage standing wave ratio		

#### 3.4.2. a. TEM Horn Antenna

This type of antennas which are made of two tapered metal plates, and fed by two wire TEM (Transverse Electro-Magnetic) mode transmission lines, are one of the most popular types of antennas used for UWB applications. Also we can consider TEM horns as a bent bow-tie dipole. Based on the work in [30], TEM horn antennas preserves the UWB pulse very well and also have a constant phase center. Also it was shown in [31] that the radiation efficiency, impedance matching and transient behavior of antenna are completely adjustable by changing the flaring and length of the antenna. The only problem of TEM horn antennas is spatial dispersion which is raised from non-planarity of the waveform from this type of antenna.

Two solutions have been proposed by [32] and [33] which are based on using lenses and reflectors, respectively. It is worth mentioning that the typical gain of this type of antenna is between 5 to 15dB which makes them suitable for directional base-station operation.

#### 3.4.2. b. Impulse Radiating Antenna

Impulse Radiation Antenna (IRA) is usually consists of a TEM horn feeding a parabolic reflector [33]. The main advantage of this antenna is its relatively high frequency-independent gain compared to other antennas which reaches to numbers like 25dBi. Also, this antenna is adjustable with a moving TEM horn from the focal point of the reflector. The high gain of this antenna makes it suitable for long-range base-station applications.

For this type of antenna, its high gain, together with its narrow beam makes the probability of interference very low.

### 3.4.2.c. Folded Horn Antenna

This antenna is basically a result of putting a sub-horn antenna inside the original horn antenna so that it divides antennas aperture in to two equal parts [34]. Using this technique, we can make the antenna even smaller in size. A typical folded horn antenna is shown in Figure3.18.

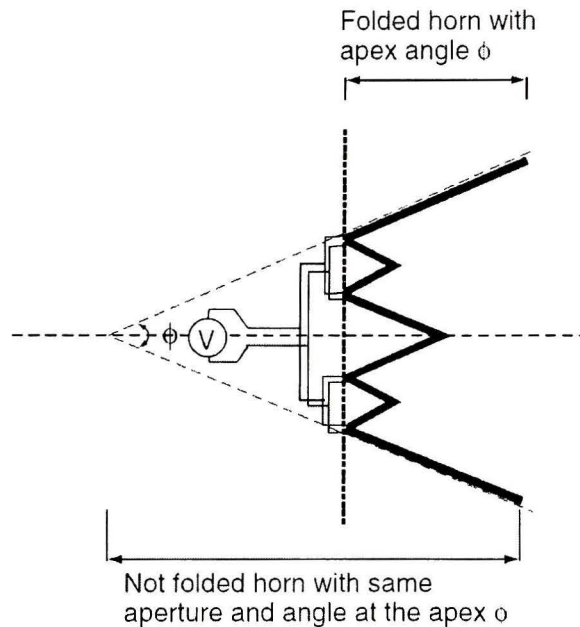


Figure 3.18. Folded horn antenna [24].

### 3.4.2.d. Dipoles and Monopoles

In [29] it was shown that using dipoles and monopoles without a resistive antenna is almost impossible for UWB systems since they will be unable to preserve the UWB pulse shape [29]. A popular antenna in this group is a bow-tie antenna in which beam-width and input-impedance are very dependent on the antenna geometry and they are almost independent of frequency. Also, the bandwidth of this antenna depends on length of plate, which is shown in Figure3.19. In fact, the flare angle and length of plate determine the lower frequency and the flare angle also determines the beam-width of the bow-tie antenna. Some of wideband bow-tie antennas are shown in Figure3.19. In this picture, we can see different terms related to the antennas' geometry.

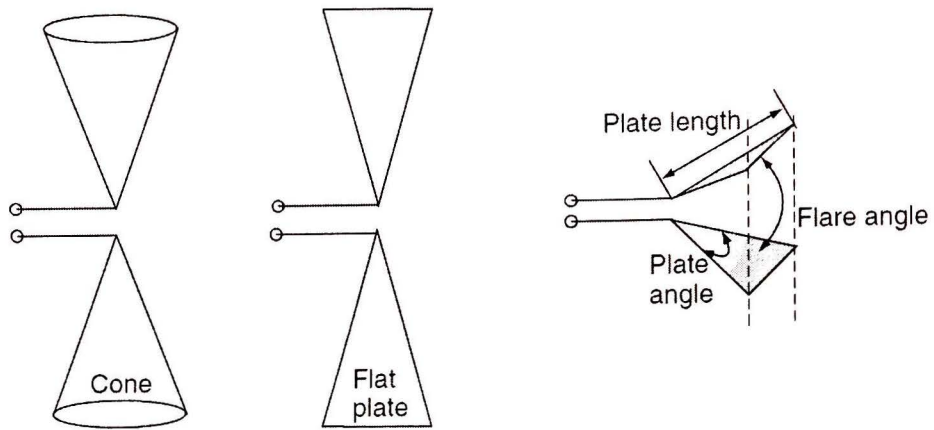


Figure 3.19. Some examples of bow-tie antenna [24]

## Chapter 4

# Ultra Wide Band Low Noise Amplifier (LNA)

In the receiver design of a UWB system, we need a low noise amplifier (LNA) as the first stage circuit. In fact, this is not only for UWB systems, but for almost any communication system, the first stage of the receiver should be an amplifier with low-noise characteristics. This is because received signal in either wired or wireless applications may be noisy and very weak, so that its signal-to-noise ratio (SNR) is very low. If the first stage of receiver is a noisy block, then there is a possibility that we lose the signal. In this case, we can say that signal is drowned in the noise. Figure 4.1 shows a typical UWB architecture and it shows where the LNA should be located in this configuration.

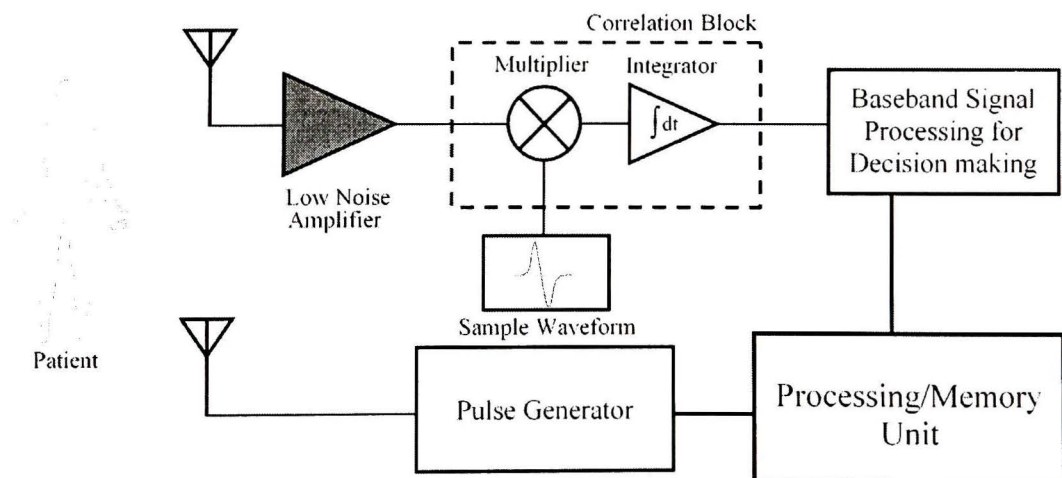


Figure 4.1. UWB LNA in medical imaging UWB system architecture [35].

In UWB systems, we also need an LNA as the very first stage of the UWB receiver. The main difference between a UWB LNA with a regular receiver LNA is in the UWB characteristics. In fact, since it is ultra-wideband, unlike narrowband LNAs, it should work for a very wide range of frequencies. In other words, different characteristics of this LNA including gain, S-parameters and noise figure (NF) should be able to meet

requirements for the ultra-wideband range of frequencies. For narrow-band designs, these parameters should have a reasonable value only for one frequency, or for a narrow band of frequencies.

To design a UWB LNA, there are several options for its circuit topology. Generally two major topologies\_ common-gate (CG) or common-source (CS) are used. Each of them can be divided to some sub-topologies like common source with inductive degeneration or common-source with an input matching network. Also, capacitive and resistive feedbacks are applicable to both CG and CS architectures.

In this Chapter we will discuss different LNA configurations in the literature and will point out the advantages and disadvantages of each configuration. We will introduce a chosen architecture and reasons our choice. Following that, a short discussion about benefits and drawbacks of this architecture and our methods to solve these problems will be presented.

By the end of this Chapter different topologies for the LNA design, together with various design techniques are introduced and explained, after which, the selected topology is introduced and discussed in detail. As a matter of fact, this Chapter is an important step for the next Chapter in which we will focus on our design and the way we improved LNA's performance using a new idea.

#### **4.1. LNA Literature Review**

There are several different circuit architectures for low-noise amplifiers (LNAs). Each circuit configuration has its own advantages and disadvantages. In this section, we discuss some of the common configuration of LNAs.

#### **4.2. Common Gate**

In [36 ], a common-gate (CG) configuration which is shown in Figure4.2 was presented. This circuit offers good output-to-input isolation, as well as wideband input matching.



showed a very good output-to-input isolation due to the selected circuit topology. This isolation was less than -70 dB over the entire bandwidth.

On the other hand, an important disadvantage of this design and other CG-based LNAs is their relatively higher noise figure (NF) compared to common-source (CS) LNAs. After writing the noise figure equations for this circuit [36], the noise figure due to only first CG stage was isolated and different methods were tried to suppress the noise figure. Regarding the noise equation, this parameter has an inverse relationship with input impedance. As a result they have tried to design the circuit and most specifically  $L_S$  and  $C_{gs1}$ , in such a way that they resonate at the center frequency of the UWB band, but they have the highest possible values for the rest of the band. Since this method is in line with improving input impedance, they did not need to find a trade-off between noise and input matching.

The second method to reduce the noise figure of the CG stage is to increase the transconductance of the first transistor. In fact, in the noise equation of the first stage, we can see that in each component,  $g_{m1}$  is in the denominator. As a result, increasing  $g_{m1}$  will help in suppressing the noise figure. On the other hand, as it was discussed before, since this transconductance has an optimum value for input matching, increasing its value might result in an adverse effect on  $S_{11}$ . Consequently, a trade off is needed when using this method. Finally we see noise figure results of this design in Figure 4.3. Here, the NF is higher than the common source designs.

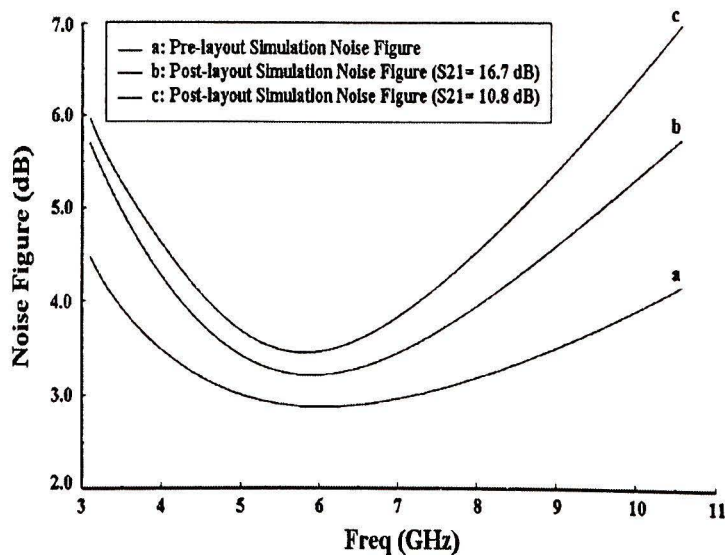


Figure 4.3. Noise figure of UWB CG-LNA proposed in [36].

Another CG-based LNA was proposed in [37]. Here, it is mentioned that typically, the higher noise figures of common-gate LNAs are one of their major drawback compared to the CS architecture. There [37], it was explained that the gate noise does not have a significant effect on the overall noise figure and it can be ignored. Ignoring this noise contribution, the NF of the CG stage in this design was:

$$\begin{aligned}
 F_{CGLNA} &= 1 + \frac{4kT\gamma g_{d0}\Delta f}{\frac{4kT}{R_S\Delta f}} \left( \frac{1}{g_m R_S} \right)^2 \\
 &= 1 + \frac{\gamma}{\alpha} \frac{g_m}{\frac{1}{R_S}} \left( \frac{1}{g_m R_S} \right)^2 \\
 &= 1 + \frac{\gamma}{\alpha} \frac{g_{mi}}{\frac{1}{R_S}} \left( \frac{1}{G_{m,eff} R_S} \right)^2.
 \end{aligned} \tag{4.4}$$

Here,  $g_{mi}$  is the MOSFET's transconductance and  $G_{m,eff}$  is the effective transconductance of the active stage at the source terminal. In a conventional CG stage, these two parameters are equal to each other, so we have:

$$G_{m,eff} = g_{mi} = 1/R_S. \tag{4.5}$$

This means that lowest value of noise would be equal to:  $1 + \gamma/\alpha$

Now if we can increase  $G_{m,eff}$  by some technique, then we can actually reduce the noise figure significantly. The authors of [37] proposed to add a  $g_m$ -boosting stage, as shown in Figure4.4, to amplify the transconductance.

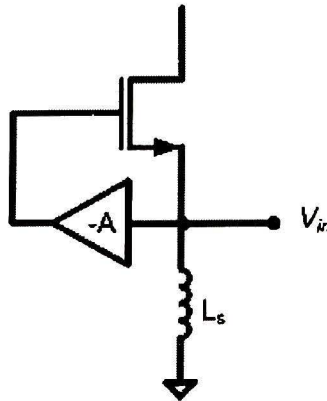


Figure 4.4 Transconductance ( $g_m$ )-boosting technique proposed in [37] to improve noise figure of CG stage.

Using this technique we can write that  $G_{m,eff} = (1+A) g_{mi}$ . Consequently, the new noise figure is given by,

$$F_{CGLNA,g_m} = 1 + \frac{\gamma}{\alpha} \frac{g_{mi}}{\frac{1}{R_S}} \left( \frac{1}{(1+A)g_{mi}R_S} \right)^2, \quad (4.6)$$

$$= 1 + \frac{\gamma}{\alpha} \left( \frac{1}{1+A} \right).$$

This result shows that using this  $g_m$ -boosting stage, the NF is significantly reduced. It was also shown that this technique will reduce power consumption by the same order, making this idea more interesting. The NF result of this design is shown in Figure 4.5. We can see in this Figure how efficient it is to add this stage for the noise figure improvement.

Although the proposed technique considerably improved the noise figure, considerably, it has its own drawbacks in the gain. As a matter of fact, as can be seen from their results,  $S_{21}$  generally has a lower value than a normal LNA with the same structure, but without using this technique.

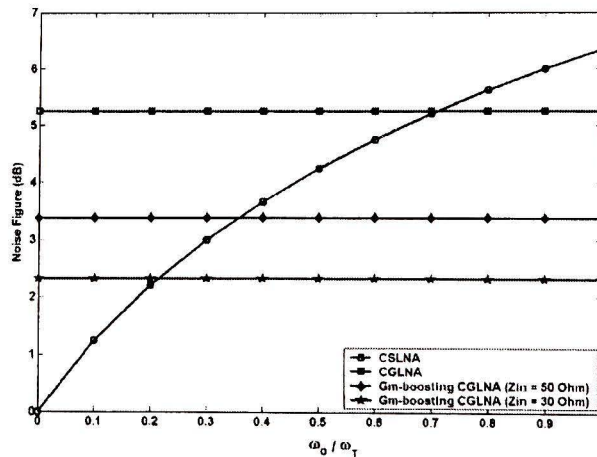


Figure 4.5 Noise figure of circuit proposed in [37] and effect of proposed idea in this work.

### 4.3. Design Techniques

#### 4.3.1. Shunt feedback

In addition to circuit topology, there are several works in LNA design which are focused on design techniques, including the addition of feedback networks. As an example, we have the addition of shunt feedback in [38] to get wideband characteristics for input

impedance plus having a flat gain all over the bandwidth. Figure 4.6.a shows the original circuit used to test the idea.

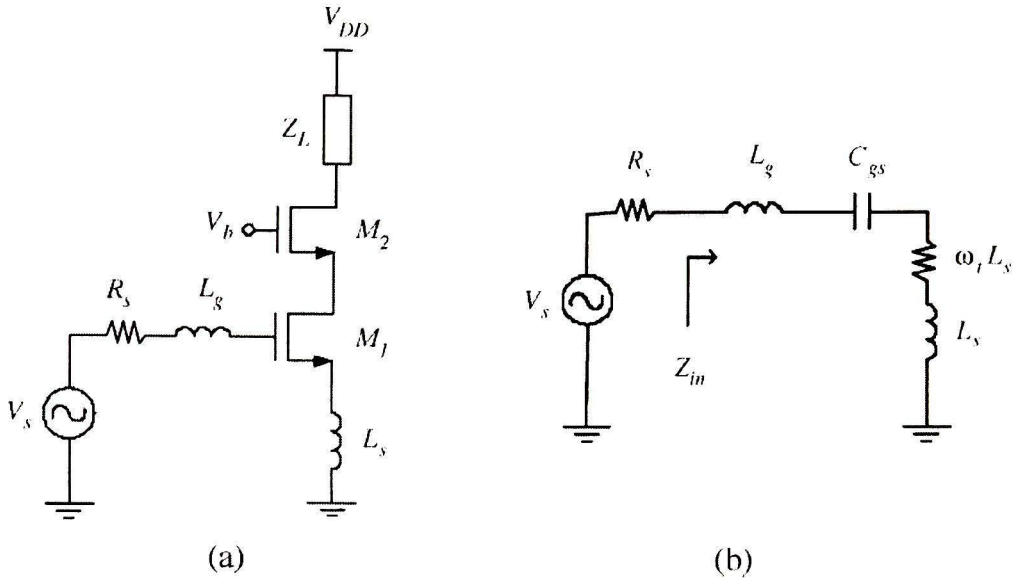


Figure 4.6. (a) Narrowband LNA topology. (b) Simple small-signal model. [38]

As we can see from Figure 4.6, we have a common source topology with source inductive degeneration. A simple small-signal equivalent circuit of the input stage is shown in Figure 4.6.b. As shown in many textbooks, this circuit's input impedance is determined by shown elements in the figure. Capacitors and inductors are designed in such a way that we have resonance at the frequency of interest. Therefore, that we will only have a real part of the input impedance which is  $L_s$ , and it is designed to be  $\sim R_s$ . To have an idea that how this circuit operates for wideband applications we have its quality factor as [39]:

$$Q_{NB} = \frac{1}{(R_s + \omega_T L_s) \cdot \omega_0 \cdot C_{gs}} \quad (4.7)$$

in which  $\omega_0$  is the resonance frequency and  $\omega_T$  is the cutoff frequency of transistor. Usually, for high-gain and low-noise applications, we prefer the Q-factor to be as high as possible. On the other hand, the -3dB bandwidth of this circuit is inversely related to its Q-factor ( $BW_{-3dB} = \omega_0 / Q_{NB}$ ). Therefore, if we want to have wideband characteristics for this circuit, then Q must be decreased.

To overcome this problem, a proposed idea in [39] is to use a shunt feedback shown in Figure 4.7.a. Its simple small-signal equivalent circuit is shown in Figure 4.7.b.



### 4.3.2. Noise Cancellation

Other than feedback there are several other techniques that are being used in the design of low noise amplifiers. In [40], Liao et al used a noise cancellation technique to reduce noise figure of the LNA, while keeping gain, linearity and matching at very acceptable values. As it is shown in Figure 4.8, they have used a common-gate stage as their first amplifying stage to easily achieve good input matching. For simplicity note that M3's biasing circuit as well as the DC current source of M1 is not shown in this picture.

The main idea of this design [40] is to cancel the noise which is generated by M1 by M2 and M3 so that its effect in output would be negligible. Also  $L_1$ ,  $L_2$  and  $L_3$  are used to cause more resonances over the bandwidth, so they cause a boosting of the bandwidth. Finally, we have the output stage which includes M4 and a current source connected to its source. This stage is only for testing and measurement, and as a matter of fact, M4 and the current source below it, together with  $C_{hp}$ , form a high pass  $gm$ -stage which is responsible for removing lower frequencies.

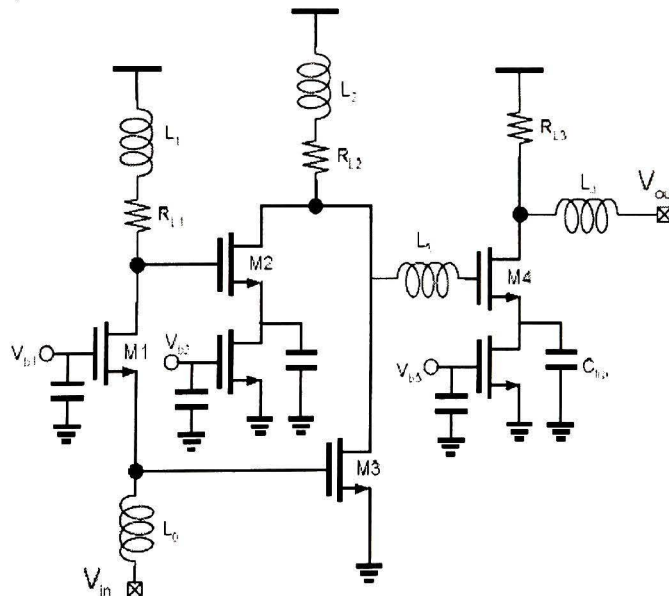


Figure 4.8. Proposed broadband noise cancelling LNA [40]

To cancel noise which is generated due to M1, we need to know its equivalent at the output node, and then we will try to make this expression equal to zero. M1's noise at the output node is equal to,

$$I_{n,out} = \frac{I_{n,M1}}{1 + g_{M1}R_S} (g_{M2}R_{L1} - g_{M3}R_S). \quad (4.10)$$

As a result, to make this expression equal to zero and considering that  $I_{n,M1}$  has always a non-zero value, we need to satisfy following condition,

$$g_{M2}R_{L1} = g_{M3}R_S. \quad (4.11)$$

After satisfying this condition, the major noise contributors in this circuit are  $R_{L1}$ , M2 and M3. It has been shown in [40] that the noise of M2 and  $R_{L1}$  are related to  $R_{L1}$ 's value. The following expression shows the final noise figure for this circuit, after cancelling M1's noise figure.

$$NF = 1 + \frac{R_S}{R_{L1}} \left( 1 + \frac{\gamma}{\alpha} \frac{1}{g_{M2}R_{L1}} \right) + \frac{\gamma}{\alpha} \frac{1}{g_{M3}R_S} \quad (4.12)$$

Finally, we have Figure 4.9 in which it is shown that how much M1 contribution to the noise figures changes before and after applying the noise cancellation technique.

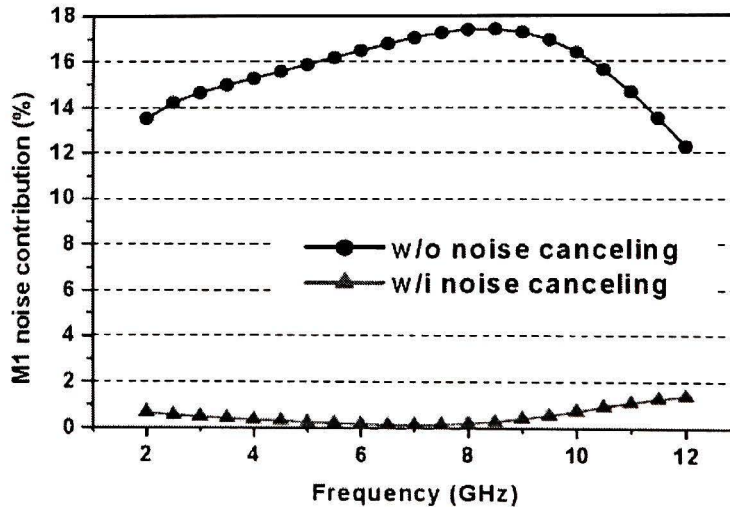


Figure 4.9. Simulated noise contribution of M1 with and without noise cancelling. [40].

Also, other characteristics of this circuit shows that it can satisfy almost all of requirements including gain, linearity, and input and output matching. The only problem of this design is its high power consumption due to added circuitry which makes it unsuitable for low-power applications. Also, using a few inductors results in a big increment in chip area, which makes the circuit inappropriate for applications that are area constrained.

### 4.3.3. Distributed Amplifiers

Besides the different techniques and topologies that are introduced up to now, there are distributed amplifiers for wideband applications [41]. Basically, in this category of LNAs, we cascade a number of amplifying stages together, and each stage provides a portion of gain for amplification. In this design methodology, since input and output parasitic capacitances of active devices are absorbed in the distributed structure, then the LNA's bandwidth will be much more than  $f_T$  of each transistor. ( $f_T$  is transistor unity-gain frequency)

Here, we have shown in Figure 4.10 from [40], the main DA structure using two input and output transmission lines coupled by the transconductance of the MOSFETs.

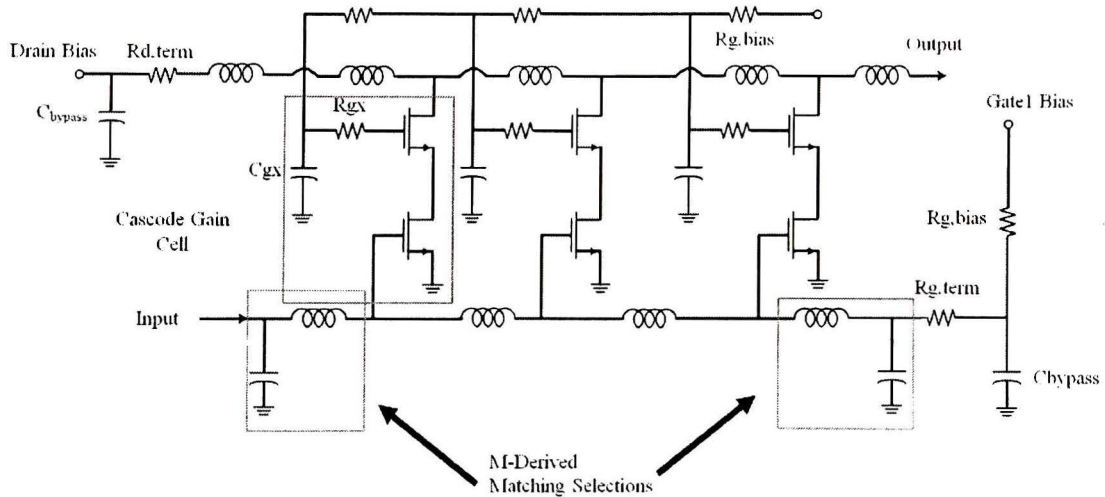


Figure 4.10 Schematic circuit diagram of cascade CMOS distributed amplifier [41].

As the RF input signal travels in gate line, each transistor is fed in its gate and as a result, they amplify the signal into their drains. If the amplified signals are designed to be in-phase with each other, they will be added together in the output line. Both input and output transmission lines are made by lumped inductors. Using this design, these authors succeeded to design an LNA which works from 0.6 to 22 GHz which is a very impressive by wide bandwidth. Also, their gain and noise figure, as well as input matching, are satisfactory. On the other hand, because of using multiple stages, their power consumption is very high and it is only appropriate for special applications in which

bandwidth is critical and power consumption is not a concern. Again, because of multiple stages, the chip area is much bigger than normal LNAs which lead to another limitation.

#### 4.4. Common Source

Finally, we discuss the common-source configuration of an LNA design. In fact, this configuration should have been introduced earlier, but since the designed LNA in this work is based on this configuration, it is preferred to be studied last. Basically, the main characteristics of an LNA, as understood from its name, are high amplifying ability (high gain) and low noise figure. A major problem with common-gate (CG) configuration is its minimum possible noise figure. In fact, the noise factor ( $F$ ) of a CG LNA is  $F \geq 1 + \gamma/\alpha$ . This minimum value for noise factor is so high that can result in ignoring other good specifications of CG stages. On the other hand, CS stages have a way lower the minimum noise figure which makes them good candidates for LNA design.

Here, in this part of the Chapter, we will go through different topologies of CS stages, and finally, we will select the best one to be used for our LNA. Since the CS stage is not wideband by nature we need to add some circuitry to make it wideband. Moreover, unlike the CG stage in which input matching could be achieved by using the  $1/g_m$  adjustment, here, we need to come up with a new idea so that it will result in better matching. As an initial step, first we try was to add a shunt resistor at the gate of the CS stage so that it will result in a very wideband matching, as shown in Figure4.11.

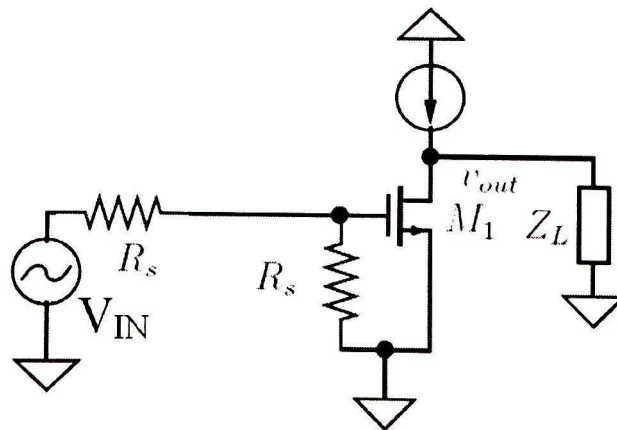


Figure 4.11. LNA with a shunt input resistor [42].

Adding a resistor right after signal source will result in worsening noise figure, and since this resistor is placed in parallel, it also degrades the gain. Simulation results show that

this type of LNA cannot have a noise Figure less than 6 dB which makes it unsuitable for many applications, including the one in [42]. However, in some of very wide-band commercial applications in which gain and noise figure are lower levels of priority than bandwidth, this type of LNA can be used.

Another wideband configuration of CS LNAs is when a shunt feedback resistor is added between gate and drain of the amplifying transistor. This design is shown in Figure 4.12.

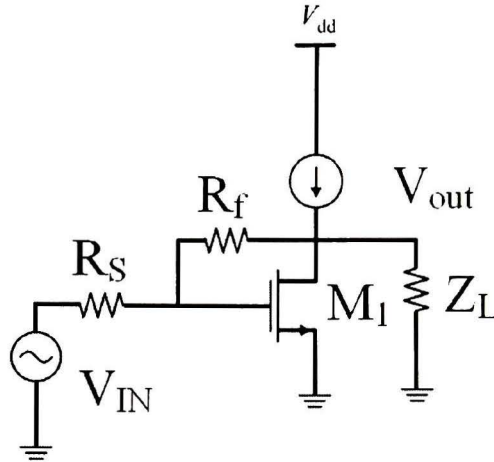


Figure 4.12. LNA with a resistive shunt feedback.

In this design,  $R_f$ 's value is normally larger than  $R_S$  in the previous design, resulting in a lower noise figure. The following equation shows the voltage gain expression of the circuit shown in Figure 4.12.

$$Gain = \left(\frac{1}{2}\right) \left( \frac{1 - g_m R_f}{1 - R_f / R_L} \right) \quad (4.13)$$

As we can see from the equation above, this gain is related to the value of the feedback as well as the transconductance of the transistor. Of course, we should be careful that these two parameters are limited from the input matching constraint. Both of these values should be chosen so that they satisfy following equation related to the signal source resistance,

$$R_S = \frac{R_f - R_L}{1 + g_m R_L}. \quad (4.14)$$

Although, in this design, the noise figure and gain have reasonable values; when we go to very high frequencies, both of these parameters degrade and are not anymore good. In later works, the authors in [42,43] replaced the resistor  $R_f$  with a common drain (CD) stage which can compensate mentioned problems to some extent, but it still suffers from additional noise figure caused by the feedback resistor or the CD stage, which is its substitute.

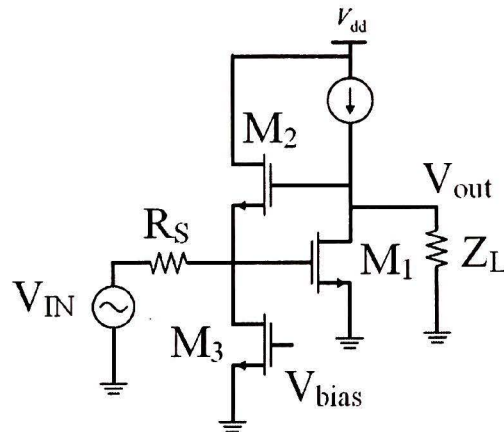


Figure 4.13. LNA with shunt feedback provided by M2.

Up to now, we have seen a few of configurations that are used for the common-source topology. In all of these circuits, a resistor is used for matching. Although they have resulted in acceptable characteristics, all of them suffer from relatively high noise figure compared to LNAs without those matching circuits. The above explanation resulted in an effort to find a lossless (or at least nearby lossless) matching network which acts as a substitute for the present methods.

Since the network is needed to be lossless, it should be made by inductors and capacitors. Also, since it is going to be used for input matching, it should generate a real component equal to the source resistance. One idea is the use of inductive degeneration that is shown in Figure4.14. We can see from this picture, and it can also be easily derived that the input impedance of this circuit is:

$$Z_{in} = \frac{1}{sC_{gs}} + sL_g + sL_S + \frac{g_m L_S}{C_{gs}}. \quad (4.15)$$

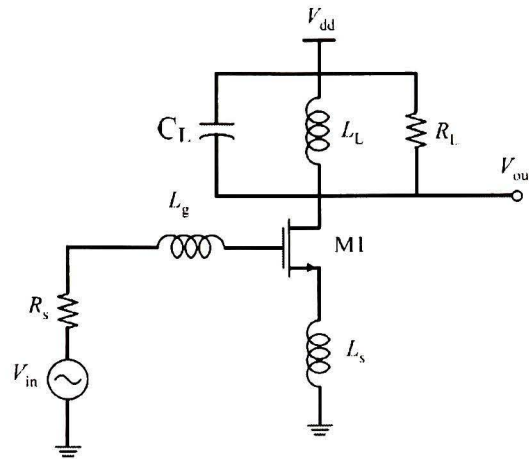


Figure 4.14. An inductively degenerated LNA.

As shown in the above expression, the real part of the input impedance is equal to  $\frac{g_m L_S}{C_{gs}}$ , which should be matched to the source resistance. In this configuration,  $L_g$  is put in the gate of M1 so that we have an additional degree of freedom. Basically, in the design of this type of amplifier, the series combination of  $L_g$  and  $L_S$  is designed to resonate with  $C_{gs}$  (gate-source parasitic capacitance of the transistor) at the desired frequency.

Putting  $L_S$  as the inductive degeneration component also affects the noise figure. In general, if we assume that the LNA circuit is a two port network in which  $L_S$  is added to it as another two-port network, we can show that noise correlation matrix will be [44-46],

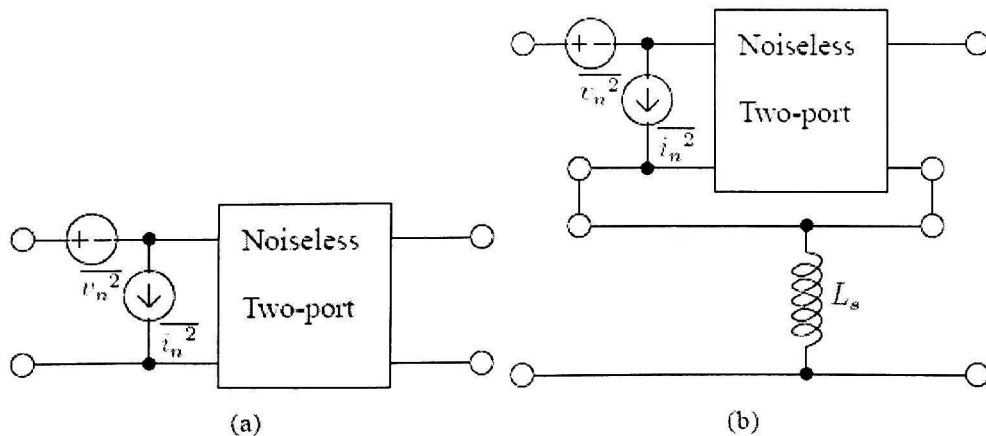


Figure 4.15. (a) two port noise model of MOSFET (b) source degenerated MOSFET represented by a two-port.

$$C_{m,0} = \frac{1}{2\Delta f} \begin{bmatrix} \overline{v_n^2} & \overline{v_n i_n^*} \\ \overline{v_n^* i_n} & \overline{i_n^2} \end{bmatrix} = 2kT \begin{bmatrix} C_{11,0} & C_{12,0} \\ C_{21,0} & C_{22,0} \end{bmatrix}$$

$$\begin{aligned}
&= 2kT \begin{bmatrix} R_{n,0} & \frac{F_{min,0} - 1}{2} - R_{n,0}Y_{opt,0}^* \\ \frac{F_{min,0} - 1}{2} - R_{n,0}Y_{opt,0} & R_{n,0}|Y_{opt,0}|^2 \end{bmatrix} \\
&= 2kT \begin{bmatrix} G_{n,0}|Z_{opt,0}|^2 & \frac{F_{min,0} - 1}{2} - G_{n,0}Z_{opt,0}^* \\ \frac{F_{min,0} - 1}{2} - G_{n,0}Z_{opt,0} & G_{n,0} \end{bmatrix} \quad (4.16)
\end{aligned}$$

in which,

$$R_{n,0} = \frac{\overline{v_n^2}}{4kT\Delta f} \quad \text{and} \quad G_{n,0} = \frac{\overline{i_n^2}}{4kT\Delta f}. \quad (4.17)$$

Now, when we add  $L_s$  for inductive degeneration, as shown in Figure 4.15.b, these matrices will change as follows,

$$\begin{aligned}
C_m &\approx 2kT \begin{bmatrix} C_{11,0} + 2\omega L_s \zeta \{C_{12,0}\} + \omega^2 L_s^2 C_{22,0} & C_{12,0} + sL_s C_{22,0} \\ C_{21,0} - sL_s C_{22,0} & C_{22,0} \end{bmatrix} \\
&= 2kT \begin{bmatrix} R_n & \frac{F_{min} - 1}{2} - R_n Y_{opt}^* \\ \frac{F_{min} - 1}{2} - R_n Y_{opt} & R_n |Y_{opt}|^2 \end{bmatrix} \\
&= 2kT \begin{bmatrix} G_n |Z_{opt}|^2 & \frac{F_{min} - 1}{2} - G_n Z_{opt}^* \\ \frac{F_{min} - 1}{2} - G_n Z_{opt} & G_n \end{bmatrix} \quad (4.18)
\end{aligned}$$

The above matrices show that  $R_n$ ,  $Y_{opt}$  and  $Z_{opt}$  will change due to addition of  $L_s$  while  $G_n$  keeps its value. What was shown above is that adding  $L_s$  will give us another degree of freedom to control noise figure of LNA and to find an optimum point for this parameter, together with others.

Beside the above-mentioned advantages of adding inductive degeneration to the LNA architecture, the circuit shown in 4.14 still has some serious problems for wideband applications. First, in the input impedance calculation, we have ignored  $C_{gd}$ 's effect due to Miller's theorem. However, this capacitance might have a significant effect if the gain of the first stage (M1) is high enough. To overcome this problem, a new approach is to

add a cascode stage right after first stage. Since the impedance seen from M1's drain is now approximately equal to  $1/g_{m2}$  as it is shown in Figure 4.16, Miller's effect will be considerably degraded for the input node and as a result, ignoring  $C_{gd}$ 's effect in input impedance calculations would not cause a significant error.

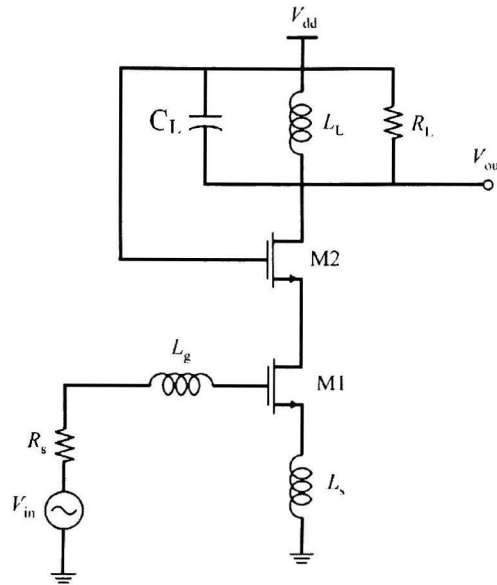


Figure 4.16. Inductively-degenerated cascode LNA.

Adding a cascode stage has other advantages including improvement of output-to-input isolation which will result in lower dependence of the input impedance on the load impedance and also improved LNA's stability.

As discussed before, in this design, the input matching network is supposed to be lossless. On the other hand, since we make  $L_g$  as an on-chip component, its quality factor is limited and as a result, it will cause losses in the input network, resulting in a higher noise figure. It should be mentioned that during the on-chip design of inductors, higher Q-factors are achievable for smaller inductors. On the other hand, we know that  $L_g$  is designed to resonate with the gate-source capacitance of M1. This means that if we can find a way to increase the  $C_{gs}$  value, we can decrease  $L_g$ 's inductance and consequently have a better quality factor.

It is also known that increasing the width of a transistor, but keeping its length constant will result in a higher gate-source capacitance. The main problem of this method is that increasing width of M1 will result in more power consumption, which is undesirable for

our low-power design. Another method is the addition of an auxiliary capacitor in parallel with  $C_{gs}$  so that they will be added together, as shown in Figure 4.17.

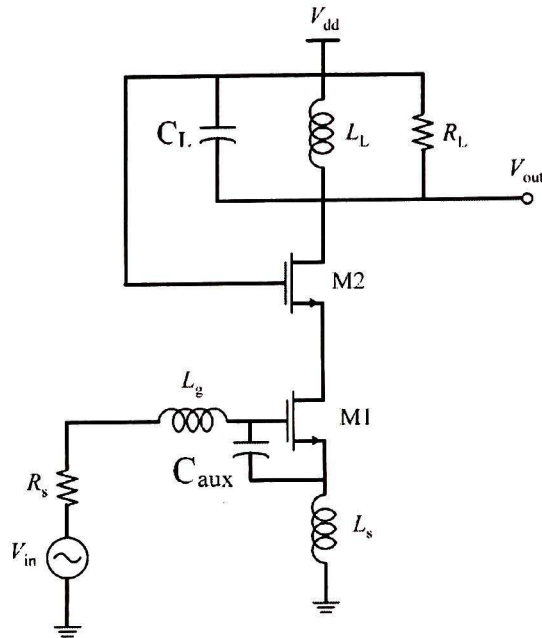


Figure 4.17. an inductively-degenerated cascode LNA with auxiliary capacitor in parallel with  $C_{GS}$ .

In the design of  $C_{aux}$ , we should be careful that this capacitor should not be very big or then the voltage gain will be degraded. Also, another disadvantage of adding  $C_{aux}$  is its effect on the unity gain frequency of the circuit, since we know that this frequency for M1 is equal to,

$$\omega_T = \frac{g_m}{C_{gs} + C_{aux}}. \quad (4.19)$$

As a result, adding this capacitor will result in limitation of this frequency. Based on the above explanations, we need to choose this capacitor's value carefully so that it won't have a bad effect on the LNA's performance.

#### 4.5. Chebyshev Broadband Matching

The final step of improvement for the inductively-degenerated LNA architecture is making the input matching broadband, while keeping it lossless. Proposed ideas that can satisfy broadband matching requirements together with keeping other parameters with good values are based on the design of multiple-order filters using reactive elements. Generally, Butterworth and Chebyshev 2<sup>nd</sup> and 3<sup>rd</sup> order filters have shown reasonable results [52]. It depends on the designer's decision to choose the filter type and its order,

with respect to the design requirements. Usually, in filter design, we have to find an optimum case for the values of the elements and the filter complexity. Basically filters must generate multiple resonance frequency over bandwidth to provide broadband matching. In this work, we chose a 3<sup>rd</sup> order Chebyshev filter which was first proposed in [47] and is shown in Figure4.18.

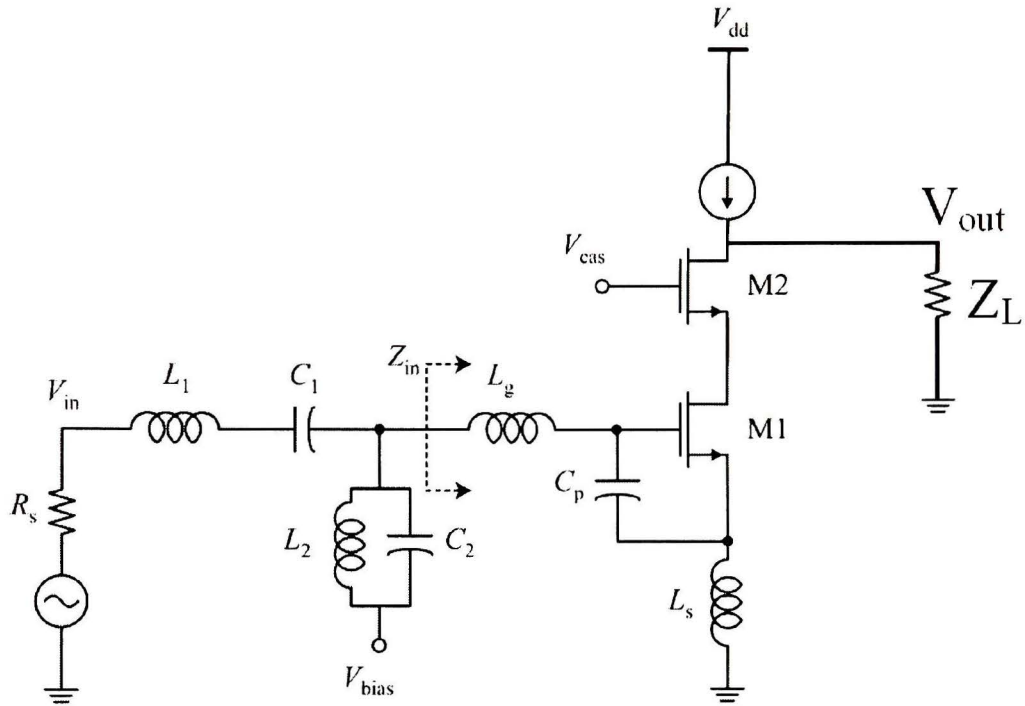


Figure4.18. Chebyshev broadband matching network [47].

# Chapter 5

---

## Design of an Ultra Wide Band LNA

---

### 5.1. Introduction

Now that we know the general architecture to be used for the LNA's design, we can go through different design aspects in detail and see what requirements we have for this design. In this Chapter, we will review the important design parameters of LNA, including gain, bandwidth, noise Figure, linearity, input and output matching and power consumption. Each parameter will be introduced briefly at first, and then the UWB requirements of this parameter will be studied. Finally, it will be described that how we have optimized our design regarding the specific parameter.

Being familiar with different parameters and their role in the LNA's performance, a new idea that made this design special will be explained in detail. Then, we will describe how adding two inductors can help us boosting both bandwidth and gain of this LNA, while keeping other parameters with acceptable values. The effect of adding each new element will be shown and reasons for changes in the gain and bandwidth curve will be explained in detail. Finally in this Chapter we will see the design procedure of this circuit. This will be followed by its layout, and simulation and measurement results together with discussions on comparison of these results.

### 5.2. LNA Design Parameters

In this section, we will go through the important parameters in the design of our LNA and the UWB application requirements of these parameters.

### 5.2.1. Linearity

Although CMOS scaling helped designers to achieve better gain and noise figure together with lower power consumption, there are also disadvantages when we are dealing with newer technologies. One of these problems directly affects the linearity of our circuit. Since the LNA is the first block of the receiver front-end right after the antenna, any distortions which are generated in the LNA will be propagated through the entire receiver. As a result, during the design of an LNA, beside considering gain and noise figure as the most important parameters, we should also consider linearity in the design to meet application requirements.

With technology scaling, there is usually a reduction of the voltage supply resulting in a reduction in voltage headroom. This means that the received signal is limited by a smaller voltage headroom and the LNA might go to saturation if signal goes higher than this voltage.

Note that scaling does not only limit the voltage headroom. The Input referred Third-order Intercept Point (IIP3) and the 1-dB Input Compression Point (ICP) are two useful parameters that be used to can determine the linearity performance of circuit. Also IIP3 is based on third-order intercept point with the first order values. The problem with scaling is that for transistors with shorter minimum channel length, the optimum point for the third-order intercept point for devices occurs at higher current density.

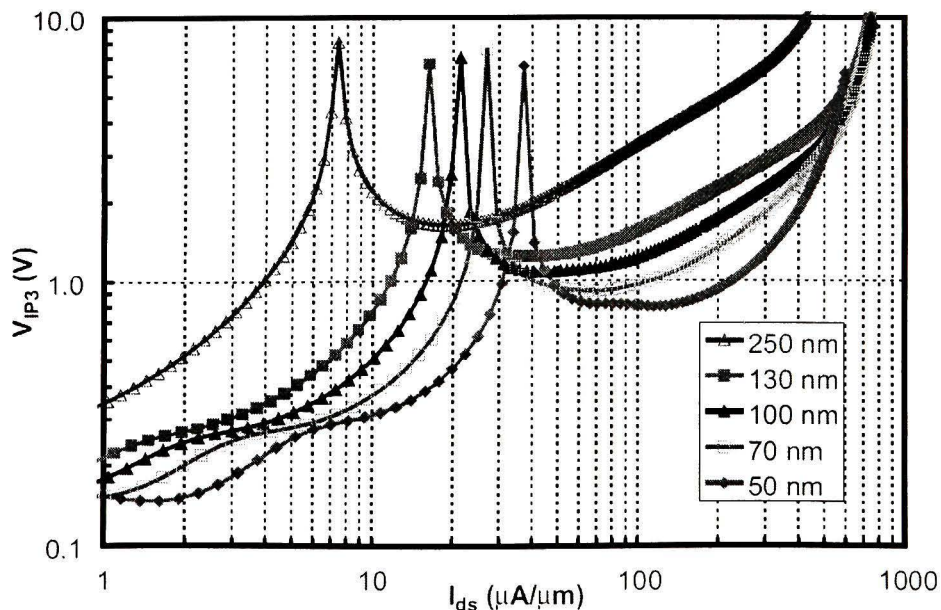


Figure 5.1. Simulated 3<sup>rd</sup> order voltage intercept point for different CMOS technologies. [48]

In Figure5.1 from [48], plots of  $V_{IP3}$  vs. current density of transistor with different channel length are shown. Here,  $V_{IP3}$  is the input voltage amplitude at which the first- and third-order output voltage amplitudes are equal, and it can be written as,

$$V_{IP3} = \sqrt{\frac{24g_m}{g_{m3}}} , \tag{5.1}$$

in which  $g_{m3}$  is second derivative of  $g_m$ .

Problems related to reduction in voltage headroom and increasing optimum current density have resulted in several efforts to find ways to enhance linearity for different RF circuits. For LNAs, among the various proposed circuit techniques, the most efficient one proposed in [49] uses a derivative superposition. In this work, the authors added a parallel transistor operating near the weak-inversion region. This transistor has a third-order coefficient which is almost equal, but with opposite sign of original transistor. This results in cancellation of the third-order term that makes a significant improvement in the circuit’s linearity. To make this clearer, Figure5.2 shows proposed circuit.

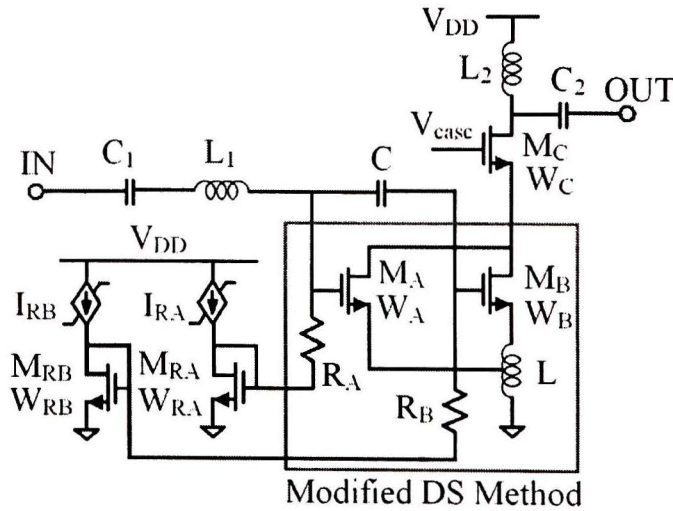


Figure5.2 Simplified schematic diagram of CMOS LNA using modified DS mode [redrawn from 49].

As we can see here both  $M_A$  and  $M_B$ 's sources are connected to a tapped inductor. Note that the tapped inductor can be replaced by two series inductors if area usage is not very important. Considering following expression for the drain current of the original transistor:

$$i_d(v_{gs}) = g_1 v_{gs} + g_2 v_{gs}^2 + g_3 v_{gs}^3 + \dots , \tag{5.2}$$

in which  $g_1$  is transistor transconductance and  $g_2$  and  $g_3$  are higher-order coefficients for the strengths of corresponding nonlinearities. In this circuit,  $M_A$  and  $M_B$  are designed in a way that a large portion of  $g_3$  of the original transistor can be cancelled out by  $g_2$  and  $g_3$  of the auxiliary device. Also, the tapping point gives us another degree of freedom for adjusting the design more precisely. In [49] it was shown that using this technique, the 20dB improvement in IIP3 is achievable with cost of only a fraction of dB increase in noise figure.

Other than this technique in [49], there are other successful works for linearity enhancement of LNAs which are mostly circuit techniques including active post-distortion or using a folded IMD sinker in the body of main circuit.

For our application of interest, since the signal level is not going to be as high as 0dBm which is limit of most of wireless systems, linearity is not a big issue and in some cases it can be even sacrificed when optimizing other important parameters such as noise figure and gain.

### 5.2.2. Noise Figure

Since we are to design a low-noise amplifier, one of the most important parameters to be optimized during design procedure is noise-figure. Basically, there are two major noise sources that determine LNA's noise figure: noise of the common-source stage transistor and noise of the input-matching network [49]. In fact, regarding Friis's formula we have,

$$F = F_1 + \frac{F_2 - 1}{G_1} + \frac{F_3 - 1}{G_1 G_2} + \frac{F_4 - 1}{G_1 G_2 G_3} + \dots + \frac{F_n - 1}{G_1 G_2 G_3 \dots G_{n-1}} \quad (5.3)$$

This shows that for any system that is made of multiple stages, as long as gain of each stage is larger than unity, then the noise of each of the following stage has less importance than the previous stage. As a result, during noise optimization, we assume that the noise generated due to the cascode stage and the load impedance are not significant. Further as shown in [50], this noise can be considered as an offset in the noise figure curve.

The noise figure of the input network is basically because of the limited quality factor of its inductors. These limitations will results in losses which can be modeled as resistors in series with the lossless inductor. Generally, for smaller inductors, high quality factors are

achievable for inductors designed and fabricated on-chip. As a result, during noise modeling of LNA, we can simply consider smaller inductors similar to bond-wire or slab inductors in which their loss is not significant. As discussed in last Chapter, the final topology that is decided for UWB LNA is shown in Figure5.3.

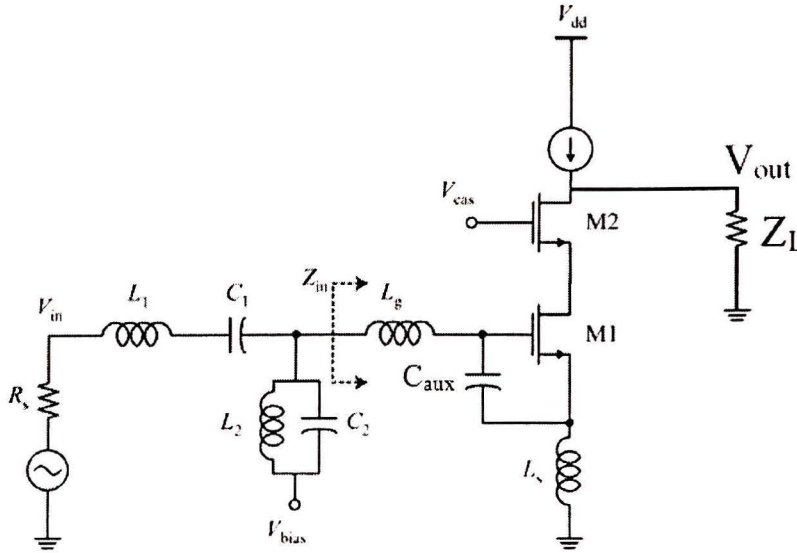


Figure5.3. Main configuration of UWB LNA

Without considering the noise generated due to the input network inductor, the first stage noise of this LNA can be modeled using the circuit shown in Figure5.4. Using this model we can write noise factor of LNA knowing that noise factor is total output noise power divided by the output noise power due to the source alone.

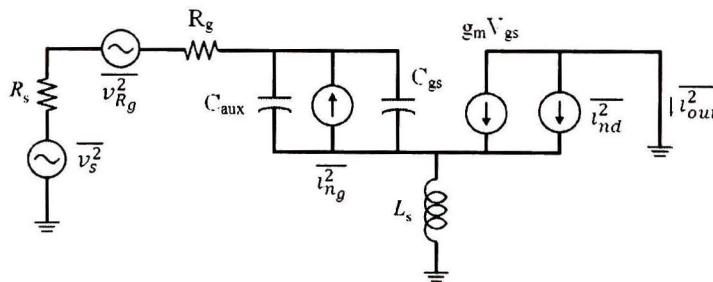


Figure5.4. Small signal model of inductively degenerated LNA shown in Figure5.3 without considering input matching network.

As it is demonstrated in this figure, the major noise sources of M1 are the drain current noise or channel noise, and the gate noise. Also, noises due to  $R_s$  and  $R_g$  can be expressed as:

$$\overline{v_s^2} = 4kTBR_s \quad \text{And} \quad \overline{v_g^2} = 4kTBR_g \quad . \quad (5.4)$$

Now considering the definition of noise factor, we have,

$$F = 1 + \frac{\overline{v_{R_g}^2} |G_m(j\omega)|^2 + \overline{i_{n_g}^2} |T(j\omega)|^2 + \overline{i_{n_d}^2} |D(j\omega)|^2}{\overline{v_s^2} |G_m(j\omega)|^2} \quad (5.5)$$

$$+ \frac{\overline{i_{n_g} i_{n_d}^*} T(j\omega) D^*(j\omega) + \overline{i_{n_d} i_{n_g}^*} D(j\omega) T^*(j\omega)}{\overline{v_s^2} |G_m(j\omega)|^2} .$$

in which  $G_m$  is general transconductance transfer function of this stage,  $T$  is the relationship between gate noise current and its output contribution and  $D$  is the same thing for drain noise. Now, using small-signal model presented in Figure5.4 we can write each one of these parameters to simplify noise figure expression. At the resonant frequency, which is when following equation is true,

$$\omega_0^2 (C_{gs} + C_{aux})(L_g + L_s) = 1, \quad (5.6)$$

$G_m$ ,  $T$  and  $D$  can be written as,

$$|G_m(j\omega_0)|^2 = \frac{g_m^2}{\omega_0^2 C_t^2 \left( R_s + R_g + \frac{g_m L_s}{C_t} \right)^2}, \quad (5.7)$$

$$D(j\omega_0) = \frac{R_s + R_g}{R_s + R_g + \frac{g_m L_s}{C_t}}, \quad (5.8)$$

$$T(j\omega_0) = \frac{R_s + R_g + j\omega_0(L_g + L_s)}{R_s + R_g + \frac{g_m L_s}{C_t}} \times \frac{g_m}{j\omega_0 C_t}. \quad (5.9)$$

and Defining:

$$O = R_s + R_g + \frac{g_m L_s}{C_t}, \quad L_t = L_s + L_g, \quad R = R_s + R_g \quad \text{and} \quad Q_s = \frac{\omega_0 L_s}{R} \quad (5.10)$$

We get

$$\frac{D \times T^*}{|G_m|^2} = \frac{R}{O} \left( \frac{R + j\omega_0 L_t}{O} \frac{g_m}{j\omega_0 C_t} \right)^* \frac{\omega_0^2 C_t^2 O^2}{g_m^2} = R^2 (j + Q_s) \frac{\omega_0 C_t}{g_m} \quad (5.11)$$

$$\frac{T \times D^*}{|G_m|^2} = \frac{R + j\omega_0 L_t}{O} \frac{g_m}{j\omega_0 C_t} \left( \frac{R}{O} \right)^* \frac{\omega_0^2 C_t^2 O^2}{g_m^2} = R^2 (-j + Q_s) \frac{\omega_0 C_t}{g_m} \quad (5.12)$$

$$\frac{|T|^2}{|G_m|^2} = \left( \frac{R + j\omega_0 L_t}{O} \frac{g_m}{j\omega_0 C_t} \right) \left( \frac{R + j\omega_0 L_t}{O} \frac{g_m}{j\omega_0 C_t} \right)^* \frac{\omega_0^2 C_t^2 O^2}{g_m^2} \quad (5.13)$$

$$= R^2 (1 + Q_s^2)$$

and

$$\frac{|D|^2}{|G_m|^2} = \frac{R}{O} \left( \frac{R}{O} \right)^* \frac{\omega_0^2 C_t^2 O^2}{g_m^2} = R^2 \frac{\omega_0^2 C_t^2}{g_m^2} \quad (5.14)$$

We can rewrite noise factor expression as:

$$F = 1 + \frac{\overline{v_{Rg}^2}}{v_s^2} + R^2 \left[ (1 + Q_s^2) \frac{\overline{l_{ng}^2}}{v_s^2} + \frac{\overline{l_{nd}^2}}{v_s^2} \frac{\omega_0^2 C_t^2}{g_m^2} + \frac{\overline{l_{ng} l_{nd}^*}}{v_s^2} (-j + Q_s) \frac{\omega_0 C_t}{g_m} + \frac{\overline{l_{nd} l_{ng}^*}}{v_s^2} (j + Q_s) \frac{\omega_0 C_t}{g_m} \right] \quad (5.15)$$

And then, using  $\overline{l_{ng} l_{nd}^*} = -\overline{l_{nd} l_{ng}^*}$  because of being purely imaginary, and also using

$$\overline{l_{nd} l_{ng}^*} = j|c| \sqrt{\overline{l_{ng}^2 l_{nd}^2}} \quad (5.16)$$

in the expression for F, we get,

$$F = 1 + \frac{\overline{v_{Rg}^2}}{v_s^2} + R^2 (1 + Q_s^2) \frac{\overline{l_{ng}^2}}{v_s^2} + \frac{\overline{l_{nd}^2}}{v_s^2} R^2 \frac{\omega_0^2 C_t^2}{g_m^2} - 2 \frac{|c| \sqrt{\overline{l_{ng}^2 l_{nd}^2}}}{v_s^2} R^2 \frac{\omega_0 C_t}{g_m} \quad (5.17)$$

Replacing each noise power source with its equivalent based on circuit elements, the final result will be:

$$F = \frac{R}{R_s} \left( 1 + R \frac{\gamma \omega_0^2 C_t^2}{\alpha^2 g_{d0}} \chi \right), \quad (5.18)$$

where

$$\chi = \frac{\alpha^2 \delta}{5\gamma} (1 + Q_s^2) \frac{C_{gs}^2}{C_t^2} + 1 - 2|c| \frac{C_{gs}}{C_t} \sqrt{\frac{\alpha^2 \delta}{5\gamma}}, \quad (5.19)$$

$$Q_s = Q_{s0} \frac{C_{gs} R_s}{C_t R}, \quad \omega_{T0} = \frac{g_m}{C_{gs}}, \quad \alpha = \frac{g_m}{g_{d0}},$$

$$C_t = C_{gs} + C_{aux}, R = R_s + R_g, \alpha = \frac{g_m}{g_{d0}}, \omega_{T0} = \frac{g_m}{C_{gs}}, \omega_T = \omega_{T0} \frac{C_{gs}}{C_t} = \frac{g_m}{C_t},$$

$$Q_s = Q_{s0} \frac{C_{gs} R_s}{C_t R} = \frac{1}{\omega_0 C_t R},$$

$$\text{and } Q_{s0} = \frac{1}{\omega_0 C_{gs} R_s}.$$

It can be shown that all of factors which are engaged in LNA's noise can be expressed as a function of over-drive voltage or auxiliary capacitor. As an example, we have gate resistance of the MOSFET which can be written as a function of  $V_{od}$ :

$$R_{g,fet}(V_{od}) = \frac{R_{\square} W(V_{od})}{12n^2 L} = \frac{R_{\square} W_f^2}{12W(V_{od})L}, \quad (5.20)$$

in which  $R_{\square}$  is the sheet resistance of poly-silicon,  $n$  is number of fingers and  $W_f$  is width of a single finger. It is shown in [50] how all the other parameters of the small-signal model, which are important in the noise factor equation can be expressed as a function of one of these two parameters mentioned above. Regarding this fact, it is possible to write the noise factor based on these parameters and then optimize the general expression. In this procedure, drawing the noise figure based on  $V_{od}$  and  $C_{aux}$  is very useful as it is used in [50] to find perfect combination which results in optimum noise figure.

Up to now, the optimization is only done for noise figure alone, but in a LNA design, we have to consider different performance parameters like power, gain and bandwidth. Based on what parameter we are considering when optimizing the noise figure, the optimization method will change.

To consider an additional constraint to optimization, we need a measure for that constraint and then we have to relate this measure to one of two basic parameters,  $V_{od}$  or  $C_{aux}$ , to be able to optimize noise figure considering that parameter. For example, to be able to apply power into our constraint,  $R_g$  is a good candidate to be a measure for power as well as having relationship with over-drive voltage, as described before. In following expression, we note that increasing the width of each transistor will result in more current drawn by this device, and will result in increasing gate resistance.

$$R_{g,fet}(V_{od}) = \frac{R_{\square} W(V_{od})}{12n^2 L} = \frac{R_{\square} W_f^2}{12W(V_{od})L} \quad (5.21)$$

The same concept can be used for gain and bandwidth. For gain, we have to find an expression for the general transconductance of the LNA which is a function of over-drive voltage, auxiliary capacitance or both of them. This equation is,

$$G_m = \frac{g_m(V_{od})}{2\omega_0 C_t (C_{aux}, V_{od}) R_s}. \quad (5.22)$$

And finally to be able to relate noise figure and bandwidth, the quality factor of a series resonance network is an appropriate choice which is related to the auxiliary capacitor and is also inversely related to bandwidth. As it will be explained later in input matching network, one of the multiple resonances which will result in wideband behavior of UWB LNA happens between  $L_g$ ,  $L_s$ , gate-source capacitance and auxiliary capacitance, as shown in Figure5.5.

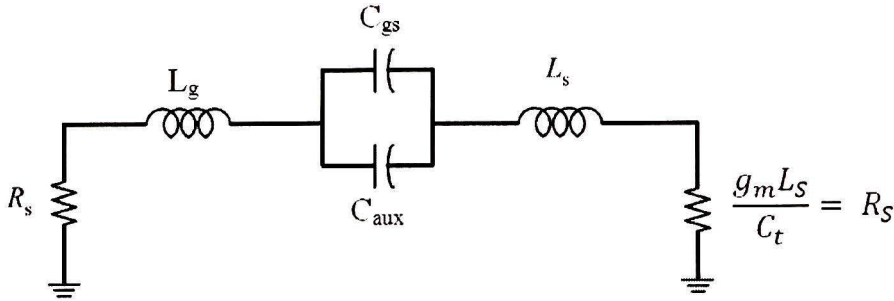


Figure5.5. RLC representation of LNA input impedance network.

The quality factor of this RLC resonance network is given by,

$$Q_B = \frac{1}{2\omega_0 C_t R_s}, \quad (5.23)$$

in which  $C_t = C_{gs} + C_{aux}$ .

The next step in the noise figure optimization is to optimize the noise figure of the input network. As stated before, smaller inductors and capacitors can be assumed as lossless elements which does not significantly affect the noise figure. The Main reason for considering the input network in the noise figure analysis is that large inductors which their low quality factor will result in losses that contribute in noise factor of whole LNA. Each one of these inductors can be divided to two parts including spiral inductor and bond wire inductor, with both of them having their own losses. Their quality factor can be written as,

$$Q_{ind} = \omega \frac{L_{g,ind}}{R_{g,ind}} \quad \text{and} \quad Q_{bw} = \omega \frac{L_{g,bw}}{R_{g,bw}}. \quad (5.24)$$

The parasitic resistances  $R_{g,ind}$  and  $R_{g,bw}$  can be expressed in terms of the quality factor of the input network by requiring a power match at the LNA's input. This is out of the scope of this work, but an example is presented in [50].

### 5.2.3. Input Matching

In designing a narrowband LNA, the reactive part of the input impedance is resonated at the carrier frequency and as a result, the optimum noise figure can be achieved at that frequency [51-53]. On the other hand, for wideband and ultra-wideband circuits, resonance should happen for the whole bandwidth. This fact results in the necessity of an input matching network in UWB LNA structures.

For our circuit shown in Figure 5.3, the input impedance can be written as,

$$\begin{aligned} Z_{in}(s) &= \frac{1}{s(C_{gs} + C_p)} + s(L_s + L_g) + \omega_T L_s \\ &= \frac{s^2(L_s + L_g)(C_{gs} + C_p) + s\omega_T L_s(C_{gs} + C_p) + 1}{s(C_{gs} + C_p)}. \end{aligned} \quad (5.25)$$

Here, we see that the real part is  $(\omega_T L_s)$  in which  $\omega_T$  is equal to  $\frac{g_m}{(C_{gs} + C_{aux})}$ . The LNA should be designed in a way that this part will be exactly (or as close as possible) equal to the source resistance. This will ensure that we have a good impedance matching. The reactive part is responsible for generating resonances all over the bandwidth to satisfy the input reflection coefficient required. In LNA designs a normal value for  $S_{11}$  is less than -10dB. Using this value, we can calculate in-band ripple of this filter as,

$$|\Gamma|^2 = 1 - \frac{1}{\rho_p}, \quad (5.26)$$

in which  $\Gamma$  is the reflection coefficient and  $\rho_p$  is in-band ripple. For -10dB reflection coefficient,  $\rho_p$  should have value less than 0.46dB.

To choose filter type and its components' values, in addition to the ripple value, we also need to know about required resonance frequencies. Figure 5.6 shows small-signal equivalent circuit for the input matching network of the designed LNA.

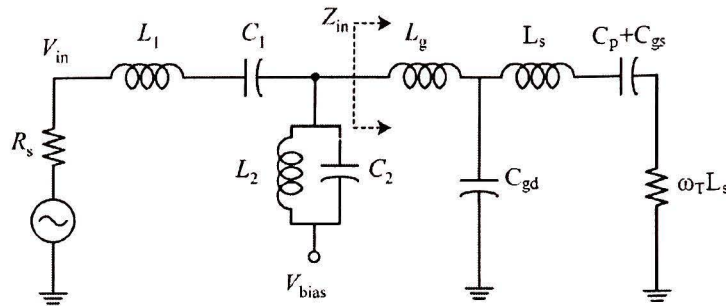


Figure 5.6. Schematic of LNA input network.

Based on what is shown in the above Figure we note that there is a series resonance between  $L_g$  and parallel combination of  $C_{gd}$  and an impedance that is the series combination of  $L_S$  and  $C_p+C_{gs}$ . Also  $C_{gd}$  is participating in two other resonances. The first one is a parallel resonance between  $L_S$  and  $C_{gd}$  and the second one is a series resonance between  $L_g$  and equivalent impedance between  $L_S$  and  $C_{gd}$ .

Now that we have discussed the resonance factors and the required in-band ripple of the filter, we can choose the filter type and the elements' values. Based on various books such as [53], which are extensively describing classic filter design, an appropriate filter should be chosen to meet the filter complexity and the requirements of the elements' values requirements. For example, if we try to make filter very simple and do not consider the elements' values, we might see that the required capacitor for  $C_{gs}+C_{aux}$  is so big that it will drastically degrade the LNA's gain. On the other hand, if we try to focus only on the elements' values, the filter might become a very complicated high-order one.

#### 5.2.4. Gain Analysis

In this section, the voltage gain of the proposed UWB LNA will be calculated. Different factors which are important in gain analysis will be introduced and some weaknesses of proposed configuration regarding gain and bandwidth will be explained. Following that, the idea which is proposed in this work will be introduced, and its effect on noise and bandwidth will be explained during a zero-pole analysis. Finally, results of applying the new idea will be compared to old results to show how efficient it is.

To calculate the gain of this LNA, the circuit is split into three stages. The first stage - the CS stage - is the important one from the gain point of view. The second stage - the CG stage (cascode transistor), can be considered as a current buffer as well as an output-to-input isolator. Finally, there are the load stage and the voltage buffer, which are only for measurement and loading purposes.

We start with small-signal model for first stage which is shown in Figure 5.6. For the  $\pi$  small-signal model, the current gain of the common-source stage is " $\beta = z(\pi) \cdot g_m$ " and here,

$$Z_\pi = \frac{1}{s(C_p + C_{gs})} \quad (5.27)$$

Now if we consider that the gate current is equal to the gate voltage ( $V_G$ ) divided by the gate-source resistance which is equal to  $\omega_t L_s$ , then the drain current  $i_d$  can be written as,

$$i_d = \frac{V_G g_m}{s(C_p + C_{gs})\omega_t L_s} \quad (5.28)$$

Assuming that the transfer function of Chebyshev filter is  $F(s)$ , then the drain current will be

$$i_d = \frac{F(s)V_{in}g_m}{s(C_p + C_{gs})\omega_t L_s} \quad (5.29)$$

It should be mentioned here that  $C_{gd}$  has not been considered in the gain analysis. Although M1 has a significant  $g_m$  which results in a large capacitor in the gate noise of this transistor due to Miller's theorem, the cascode stage above M1 and its low input impedance, which is the load impedance for first stage, makes the Miller effect of  $C_{gd}$  very small so that it can be neglected. Miller capacitance  $C_M$  is equal to,

$$C_M = C_{gd}(1 + g_m(r_o || R_L)) \quad (5.30)$$

Here, for the common-source stage,  $R_L = 1/g_{m2}$  is small enough to make the Miller capacitance negligible. Using the above equations, the LNA's gain would be given by

$$\frac{v_{out}}{v_{in}} = \frac{-F(s)g_m}{s(C_p + C_{gs})\omega_t L_s} * \frac{(sL_L + R_L)}{1 + sR_L(C_{db2} + C_{gd3}) + s^2 L_L(C_{db2} + C_{gd3})} \quad (5.31)$$

Considering this gain equation, it can be seen that for higher UWB frequencies, the gain of the LNA will degrade significantly due to last term of the denominator, which is,  $s^2 L_L (C_{db2} + C_{gd3})$ . This degradation becomes more serious when trying to increase the gain from values around 10 dB reported in [47], to higher values such as 18.6 dB that we have achieved in our design.

In fact, even if the poles and zeros remain in their original place, increasing the mid-band gain will reduce the 3-dB bandwidth. However, we can increase the mid-band gain by increasing the transconductances of the transistors in the gain stage. A limitation of this method of gain boosting would be the larger parasitic capacitances which will result in smaller (more undesirable) poles. As a result, we need to find a way to move the undesired poles out of the bandwidth of interest.

To solve this problem, we added two inductors. Each of the inductors will affect the gain curve by means of adding or displacing some poles and zeros so that the unwanted poles which are generated from the parasitic capacitors will be cancelled or moved outside of the bandwidth.

Figure 5.7 shows the completed LNA circuit after adding the auxiliary inductors. As it will be explained later, adding these elements will help bandwidth extension for higher gain values.

In first step,  $L_D$  is put between cascode and buffer stages to split the capacitance seen from  $M_2$ 's drain. Therefore, the buffer stage will be isolated from the cascode stage, so the capacitance seen from  $M_2$ 's drain node will be only  $C_{db2}$  instead of  $(C_{db2} + C_{gd3})$ . Consequently, in the gain equation,  $s^2 L_L (C_{db2} + C_{gd3})$ , will be reduced to  $s^2 L_L (C_{db2})$ . Also, since  $C_{db2}$  is much smaller than  $C_{gd3}$ , then, even considering the Miller effect, the gain reduction will be much smaller.

The new gain equation of the LNA, which is calculated with  $L_D$  taken into account, will be,

$$\frac{v_{out}}{v_{in}} = \frac{-F(s)g_m}{s(C_p + C_{gs})\omega_t L_s} * \frac{(R_L + sL_L)(1 + s^2 L_D C_{gd3})}{1 + sR_L C_{gd3} + s^2 (L_L + L_D) C_{gd3} + C_{db2} (R_L + sL_L) (s^2 L_D C_{gd3} + 1)} \quad (5.32)$$

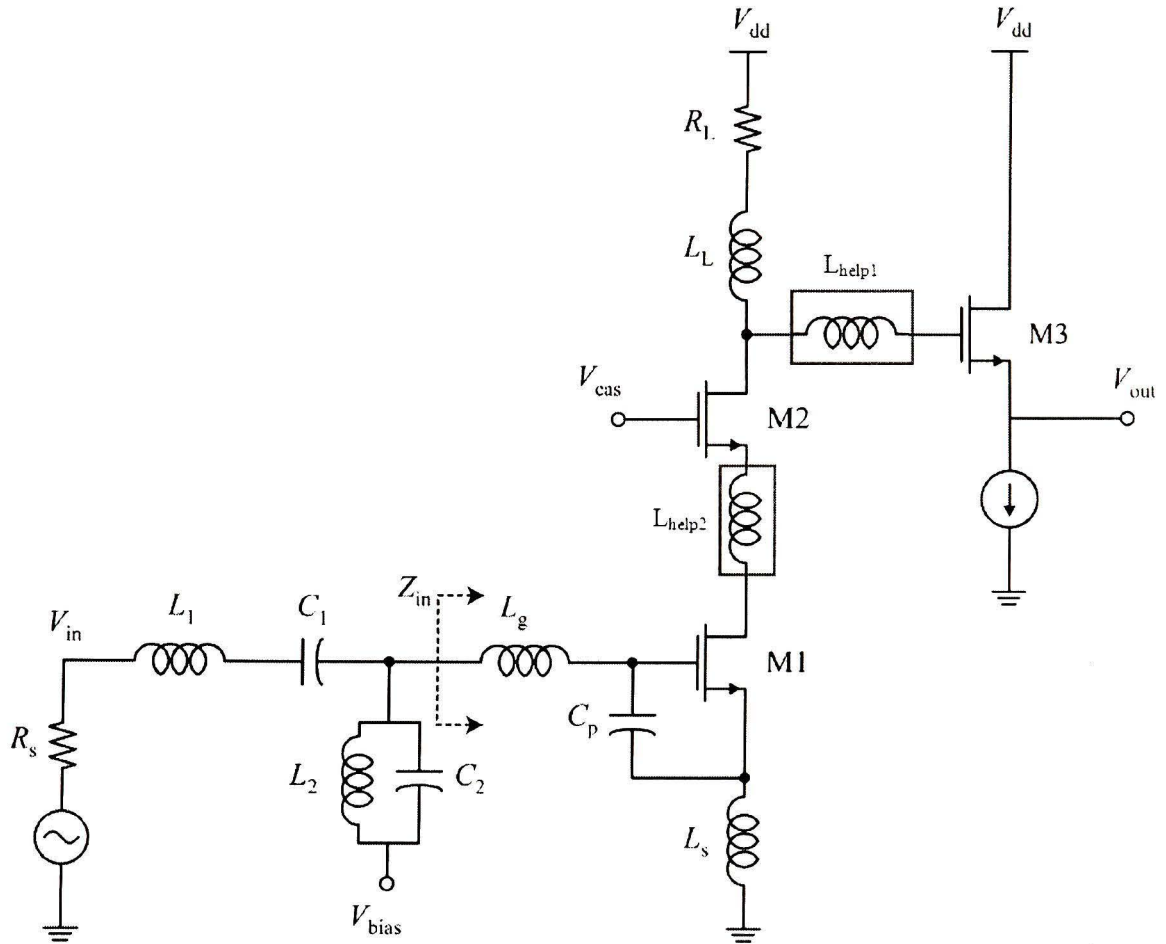


Figure 5.7. Completed LNA circuit after addition of both auxiliary inductors.

This expression shows that with an appropriate choice of  $L_D$ , degradation of the LNA's gain at higher frequencies can be prevented. Consequently, a wider flat gain curve can be achieved. From another point of view, if we consider the step response of this circuit, then isolating the buffer stage from the cascode stage and splitting  $C_{db2}$  and  $C_{gd3}$  from each other results in much smaller capacitance to be charged and discharged every cycle [53.5]. This means shorter transient times in time domain and wider bandwidths in frequency domain.

To explain more precisely, a pole-zero analysis for both cases, with- and without- $L_D$ , has been carried out to show actual effect of this inductor on the gain of circuit. The results are shown in Figure 5.8. As shown, there are some poles and zeros generated due to placement of  $L_D$ . In fact adding  $L_D$  adds two poles and two zeros (one of zeros is a twin one) to this circuit. It actually adds more than two pairs, but the other zero-pole pairs

happen at the same frequency and so cancel each other's effect. Consequently, they are not important for our analysis. An appropriate design for  $L_D$  will cause poles and zeros in specific frequencies that will help to increase and widen the gain curve.

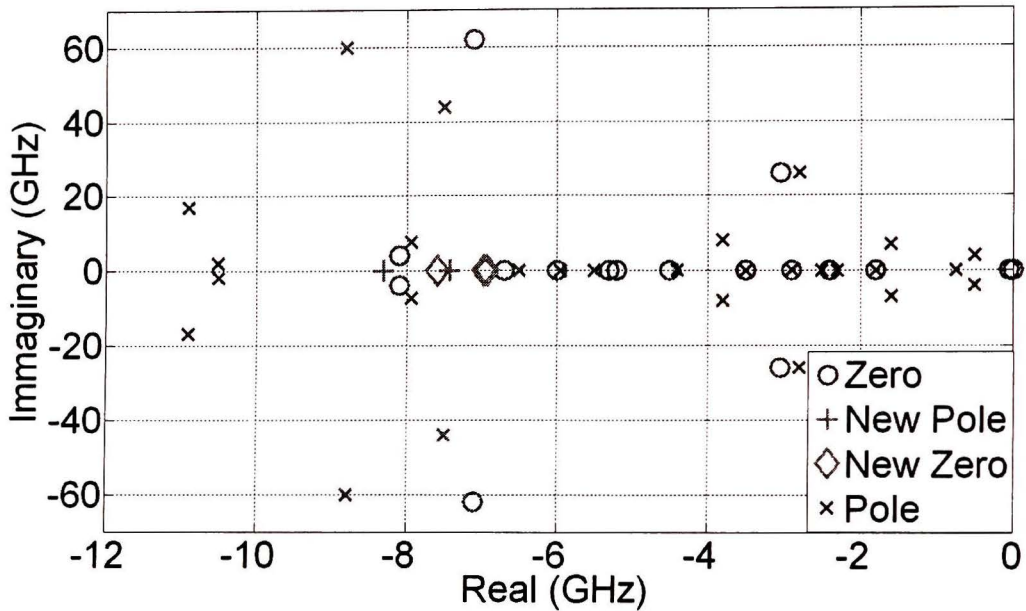


Figure 5.8. Pole zero analysis results before and after putting  $L_D$ . Two poles, one zero and one twin zero are generated as a result of putting  $L_D$ .

In our circuit, we have designed  $L_D$  in such a way that the added poles and zeros are as follows.

New Pole (GHz)	New Zero (GHz)
7.419	6.937(twin)
8.306	7.592

The pole at 7.419GHz and the zero at 7.592GHz are close enough to approximately cancel each others' effect and consequently would not have any significant effect on the gain amplitude or phase curves. In contrast, the other pole and zero have very different effect. The zero at 6.937GHz, which is a twin zero, not only prevents the gain to decrease for higher frequencies, but it also results in an increase of the gain amplitude for frequencies beyond 6.94GHz at a rate of 20dB/decade. This increase will continue until

the next pole at 8.306GHz, which stops the gain increment, and after that, a twin pole at 8.7GHz will cause a sharp decrease in gain until the end of bandwidth.

To summarize, the gain curves for LNA before and after putting  $L_D$  is shown in following Figure 5.9. We can see the impressive effect of this component, as explained above.

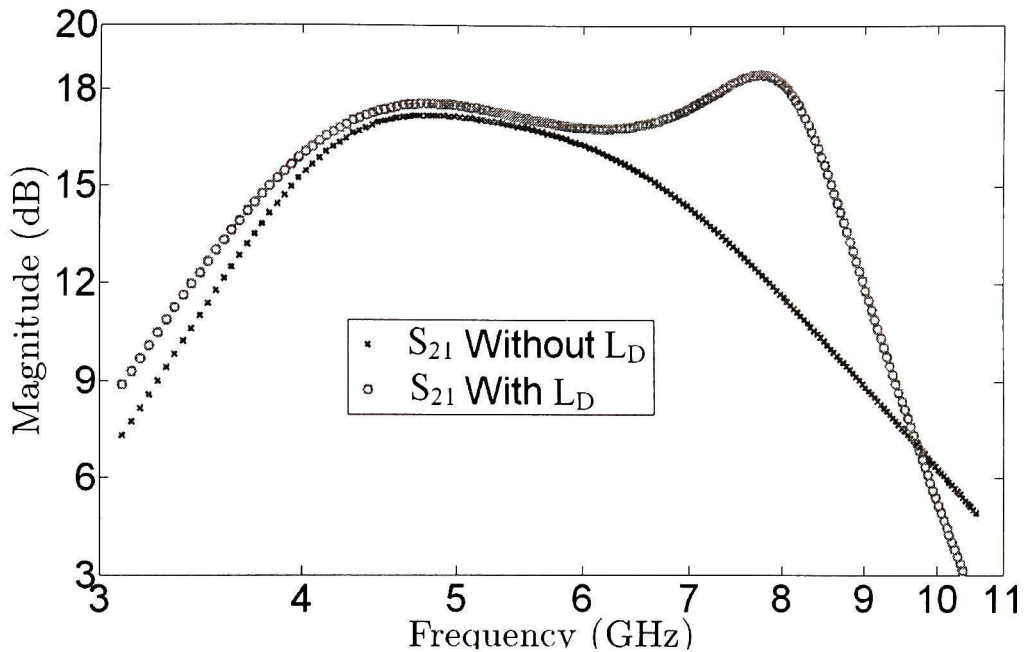


Figure 5.9. A comparison of gain curves before and after putting  $L_D$ . As it is shown, due to adding this new inductor, gain has much higher values for higher frequencies compared to the case without  $L_D$ .

In addition to the maximum gain value, gain flatness is another important concern in the design of amplifiers. Adding  $L_C$  as the second new component to this LNA is an effort to achieve the required gain flatness.

Before discussing the effect of  $L_C$ , we briefly describe the cascode stage. Because it is usually a current buffer, we expect that a cascode transistor does not have any effect on the high-frequency gain. The main reasons for us to choose a cascode stage for this LNA are - first to isolate input and output, second, to reduce the effect of  $C_{gd1}$ , and finally to increase the low-frequency gain to some extent. Despite all the above advantages, there are some drawbacks for the cascode stage. Most importantly, some parasitic capacitances which degrade the gain, NF and linearity will be created due to the placement of this element. In fact putting  $L_C$  will help to compensate to some extent, this degradation. This inductor  $L_C$ , together with  $C_{gd1}$  and  $C_{gs2}$ , can form a broadband  $\pi$ -section LC network. As

a result, it can resonate with the capacitors to produce broadband operation for the LNA [54].

Again for design of this inductor,  $L_C$ , a pole-zero analysis has been performed to choose the value in a way such that LNA gain becomes flatter and also less steep for frequencies at the UWB high frequency end.

As shown in Figure 5.10, adding  $L_C$  has caused three poles to be displaced and also one pole to be generated. In addition, two pole-zero pairs have been generated, but these are not important for our analysis since they cancel each other.

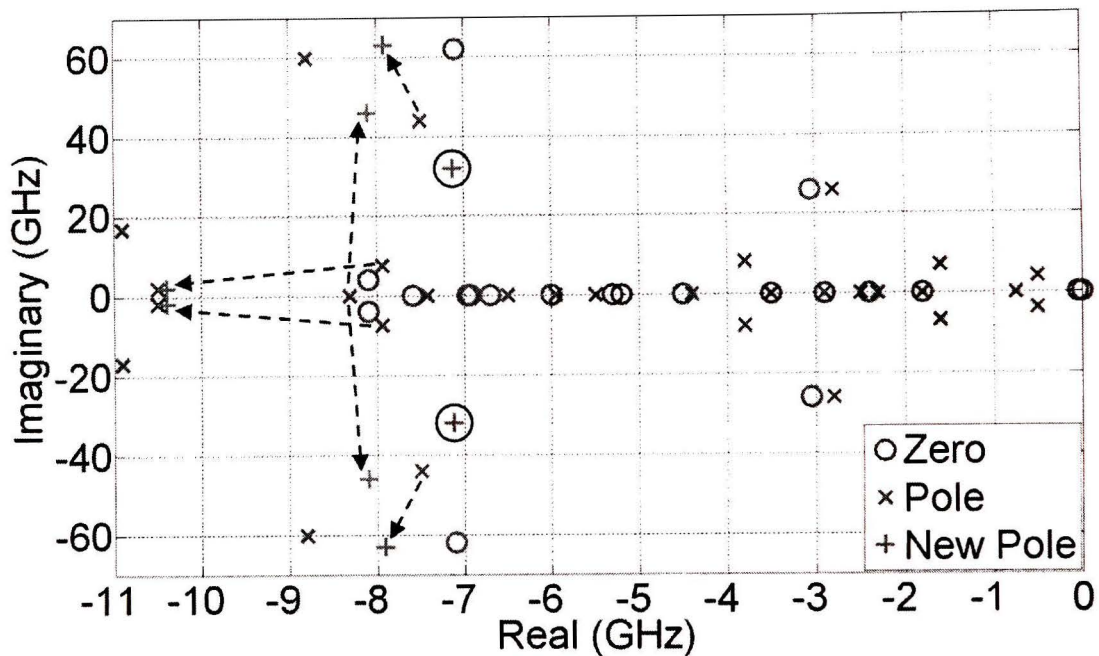


Figure 5.10. Pole zero analysis results before and after putting  $L_C$ . As it is shown, one new pole is generated and 3 poles are displaced. These changes caused gain curve to be more flat as well as a little improvement in very high frequencies of the band.

Among the three poles that have been displaced, two of them do not make any significant change. The first one is a pole at 8.3GHz which is moved to 8.1GHz. Also, there is another pole which is moved from 7.52GHz to 7.91GHz. Again for this pole, the change is not large enough to make a significant difference in the gain curve. On the other hand, the displacement of the third pole is a very effective one. This pole is moved from 7.94GHz to 10.4GHz. This means that the gain drop will be less sharp for frequencies between 7.94 to 10.4GHz by 20dB/decade. And lastly, the most important effect of  $L_C$  is the pole which is generated at 7.13GHz. Since this pole is designed to be very close to the

twin-zero that was generated due to the addition of  $L_D$ , it can cancel out one of the zeros and as a result, there will be no gain increment from this frequency, 7.13GHz, until 8.1GHz, which is start of the gain decrease. This will make gain curve flatter than the previous case. To illustrate these explanations, the gains of the LNAs are shown in Figure 5.11 both with and without  $L_C$ . Here, we can see that with both  $L_C$  and  $L_D$ , the gain curve is quite flat. From this gain curve, the final gain of the designed LNA has an impressive peak value of 18.6dB.

To demonstrate amount of improvement in gain of this LNA with the added components, a comparison between our design and that in [47], is shown in Figure 5.12. In [47], the structure of LNA is the same as ours, except for the two added inductors  $L_D$  and  $L_C$  in our design. Also, it is worth noting that the DC current of the design in [47] is 5mA, resulting in 9mW power consumption (supply is 1.8V). In our design, the current is only 3.3mA, resulting in only 4mW power consumption.

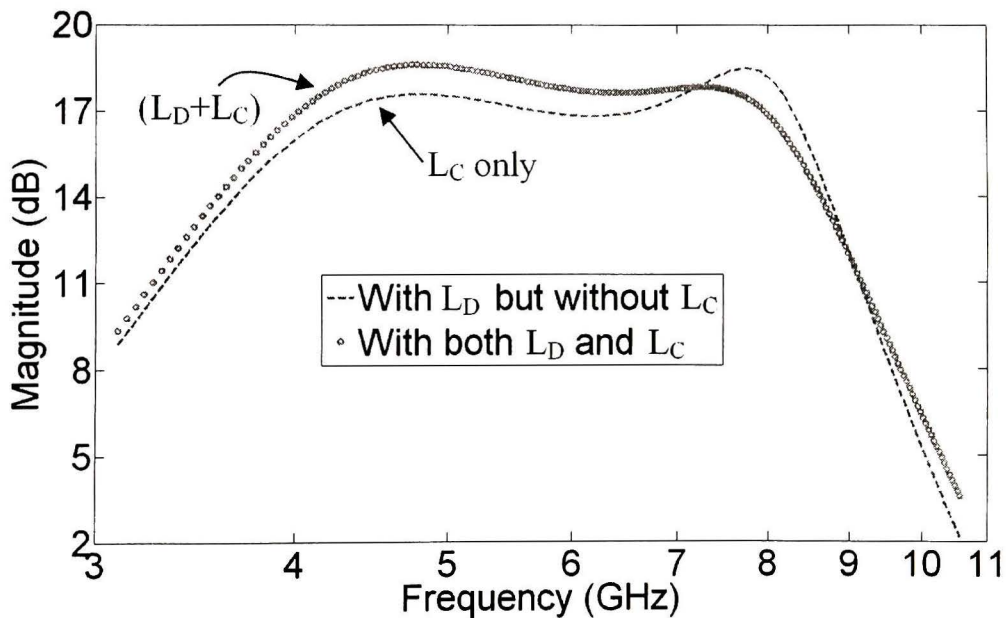


Figure 5.11. A comparison of gain curves before and after putting  $L_C$ . As it is shown, due to adding this new inductor, gain is more flat compared to the case without  $L_D$  and also it has higher values for frequencies in high-end of the band.

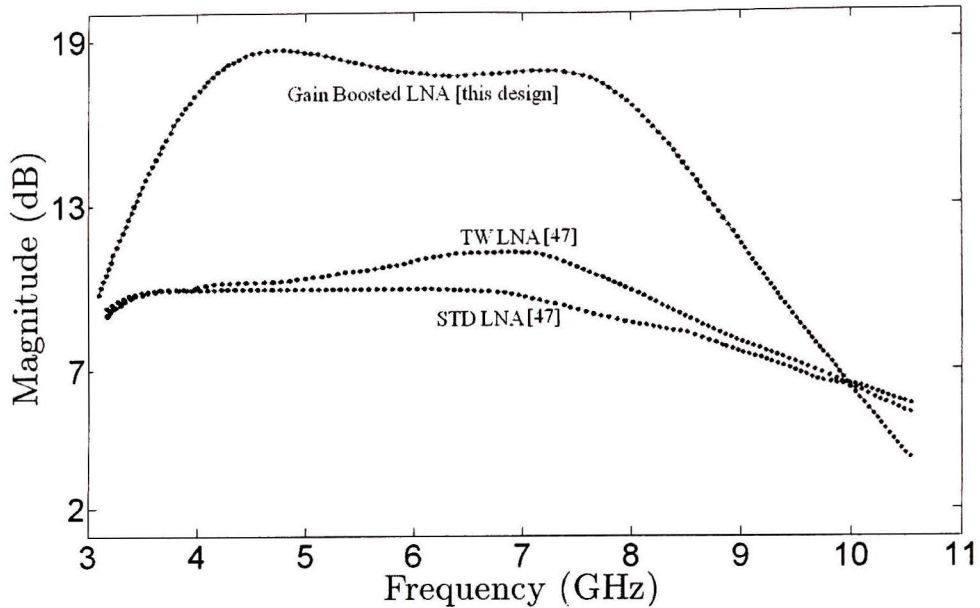


Figure 5.12. Gain comparison between this design and the LNA design which is presented in [47]. Both designs use exactly the same topology and the only difference is that in our design two inductors have been added.

### 5.3. Design Procedure

Now that we have analyzed all of aspects of our LNA, we can design LNA components. For the input matching circuit, the theory and equations on how to choose the elements' values were already described. During simulations, we decided to slightly sacrifice  $S_{11}$  to get a better noise figure and gain. This was done by making  $C_p$  a bit smaller than its optimum value for  $S_{11}$ . The final values for the input matching network were -  $L_1=1.45\text{nH}$ ,  $L_2=1.47\text{nH}$ ,  $L_g=128\text{pH}$ ,  $L_s=130\text{pH}$ ,  $C_1=310\text{fF}$ ,  $C_2=21\text{fF}$  and  $C_p=11\text{fF}$ .

Next, the bias current should be set to meet the power consumption specifications. Power consumption is fixed at  $4\text{mW}$  and as a result, the bias current would be  $\sim 3.3\text{ mA}$ . Using this bias current, we could determine which transistor width gives optimum point for best combination of NF and gain which final value was  $W_1=240\mu\text{m}$ .

The next component to be characterized is  $M_2$ . We should make  $M_2$  as small as possible to make its parasitic capacitance low. A lower limit for the size of  $M_2$  can be set by its noise contribution. Also, since  $M_2$  has a non-zero  $V_{ds}$ , it has an effect on linearity. In this

design, we chose  $W_2 = 160 \mu\text{m}$ . It should be mentioned that for both  $M_1$  and  $M_2$ , the minimum length, which is  $130\text{nm}$ , has been chosen.

The next part to be characterized is the load stage. In the previous section, details on how we determine the  $L_D$  and  $L_C$  values were presented. Also,  $R_L$  is chosen with regards to the voltage headroom. Here, we have  $L_D = 6.93\text{nH}$ , and  $R_L = 90\Omega$ . Now that we have all of elements values, from simulations, we can find the frequency in which  $L_c$  should resonate, and as a result, we can choose a value for  $L_c$  to compensate for degradations in gain at that frequency. Here, we set  $L_c = 480 \text{ pH}$ .

Finally, we have the buffer stage, which neglecting its small effect on attenuating the voltage-gain, is useful for output matching, in addition to having a flat gain, as mentioned before. For the buffer stage, the only important point is that we need to make sure that our chosen values guarantees  $S_{22}$  lower than  $-10\text{dB}$ . Since from the output node, the impedance is equal to  $1/g_{m3}$ , we need to set the  $W_3$  in a way such that  $g_{m3} = 1/50$ . In our design, we chose  $W_3 = 48 \mu\text{m}$ .

The bias voltages for  $M_1$  and  $M_2$  are set externally. In this way, by manually varying the bias voltages, we can see effect of changing the transistors' bias conditions on the LNA's performance. Also, the current source is designed using a current mirror.

Using above design, following simulation results are achieved for UWB LNA. Figure5.13 shows the input reflection coefficient for the designed LNA. As shown, the results are quite good for  $3.2\text{GHz} - 10.6\text{GHz}$ , with  $S_{11} < -10\text{dB}$ .

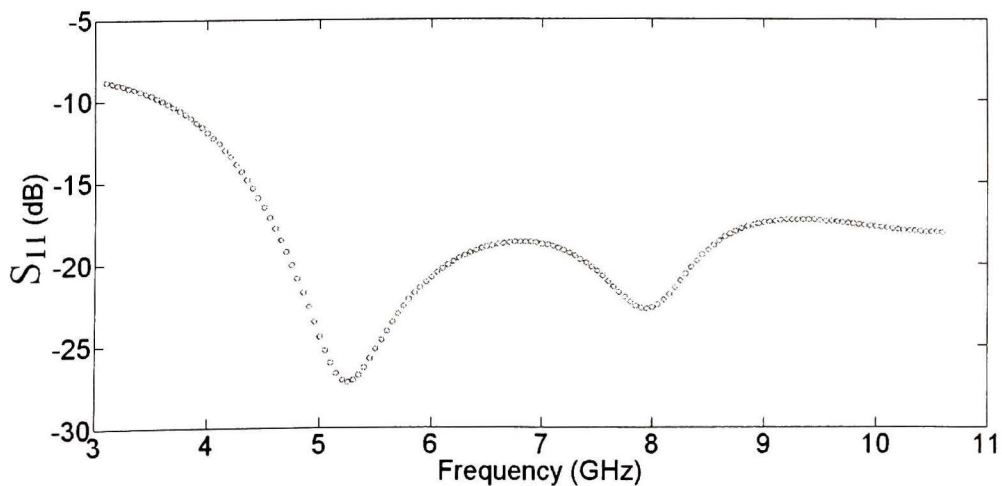


Figure5.13. Input reflection coefficient versus frequency.

Figure 5.14. shows the effect of new added inductors on power gain. As we see, not only is the maximum gain increased, but the gain is flat over a wider range of frequencies. As shown in Figure 5.14, the 3dB band is 3.5 to 9.1 GHz, with a peak gain of 18.6 dB.

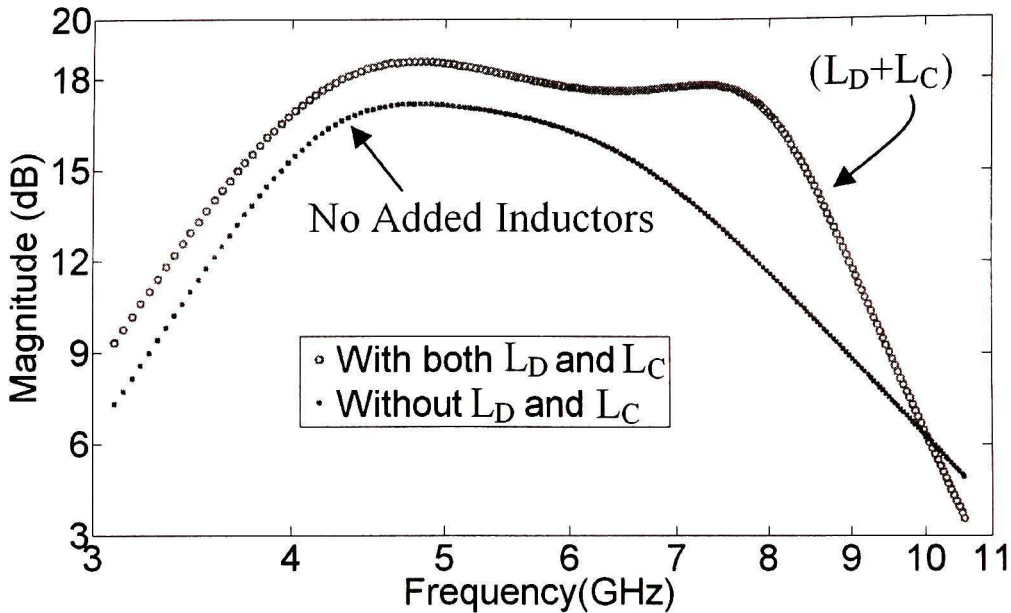


Figure 5.14. Power gain of LNA for cases with and without LD and LC.

Figure 5.15 shows inverse isolation of this LNA, which as we observe, is completely acceptable and always below -34 dB, indicating excellent isolation. The Cascode stage has a significant effect on output-to-input isolation of this circuit.

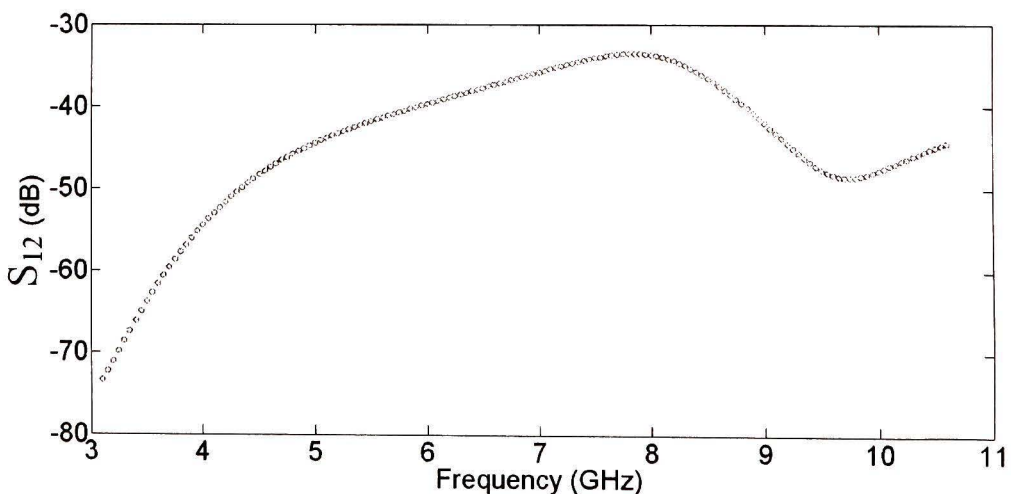


Figure 5.15. Inverse isolation of LNA versus frequency.

Figure 5.16 shows the output reflection coefficient, and for the whole band, a very good output matching is achieved and  $S_{22}$  is always below -10dB.

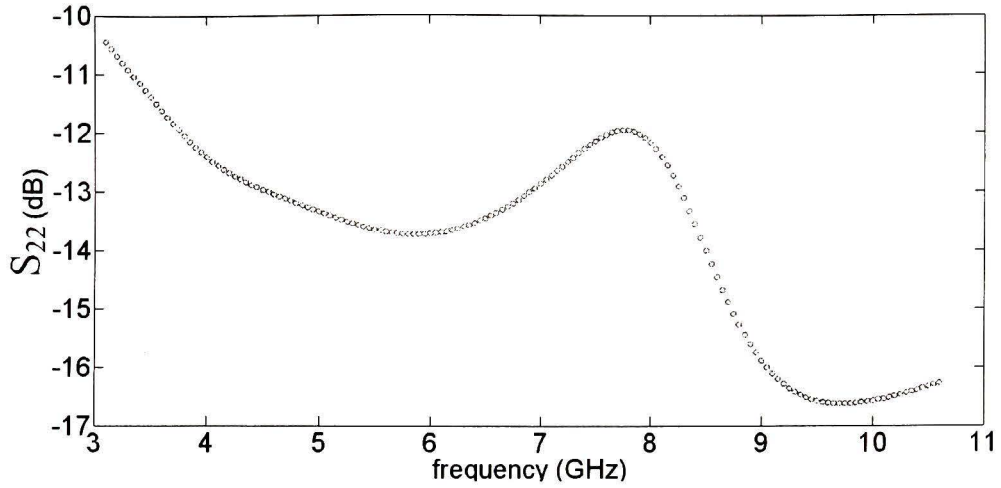


Figure 5.16. Output reflection coefficient versus frequency.

The noise performance of this LNA is shown in Figure 5.17. Usually, for UWB LNAs, the average NF is more important than the minimum noise figure,  $NF_{min}$ . Here, the  $NF_{min}$  is equal to 3.3 dB and average NF is 4.7 dB, which are both very good values for this circuit.

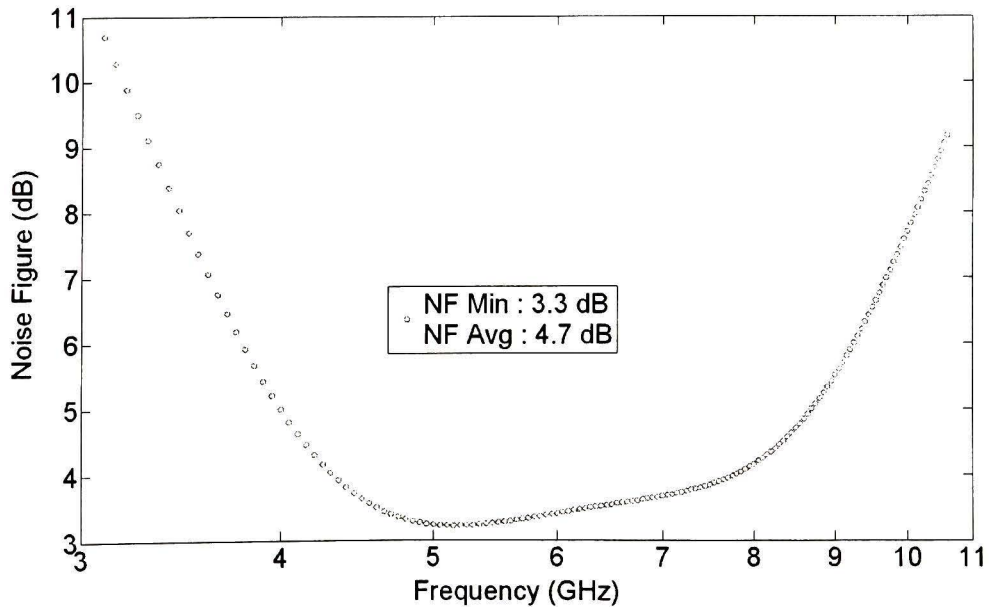


Figure 5.17. Noise figure of LNA versus frequency

Finally, we have Figure 5.18 which shows the IIP3 results. This parameter, which indicates the linearity of our design, is quite impressive. Here, the IIP3 is -0.97 dBm, determined at 6GHz.

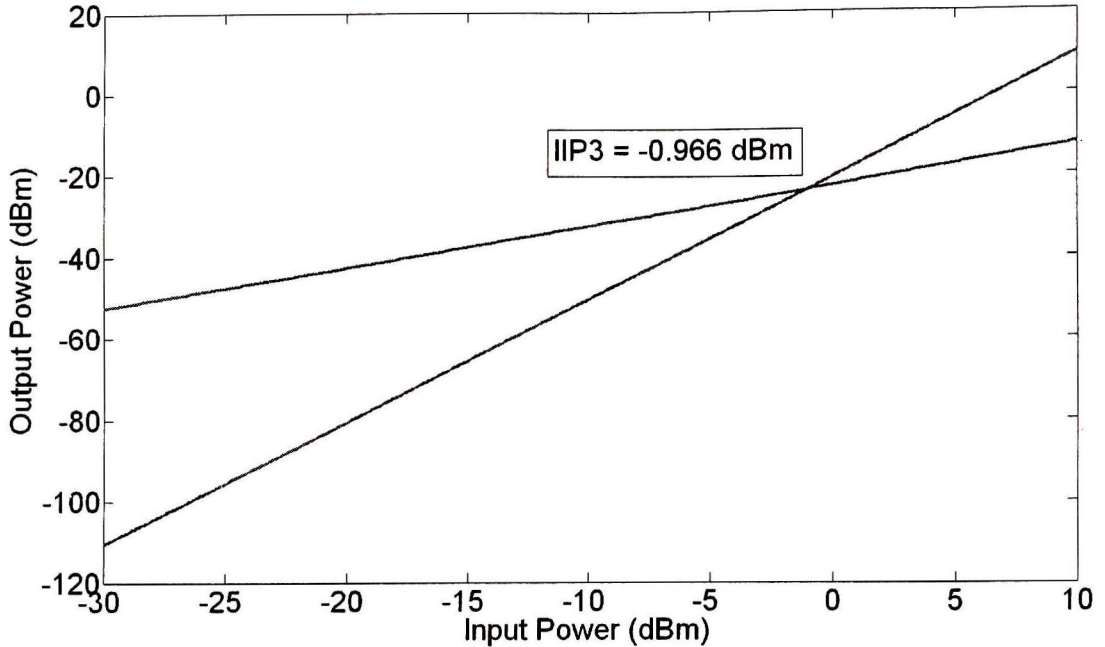


Figure5.18. Third-order intercepts point of LNA.

#### 5.4. Layout

The layout design was done using the Virtuoso Layout Editor tool available in the Cadence package. Figure5.19 shows a screen capture of the layout. Generally, it has three main sections including two LNAs and one calibration structure. To make a clear comparison between conventional LNA and LNA after the addition of both inductors, both of them are laid out to be compared. Also, for calibration purposes, some structures have been added to the layout. The core two-stage amplifier occupies an area of  $1.3 \text{ mm}^2$ . The inductors were laid using the top metal layer since it has the least sheet resistance. Also, since it is furthest away from the substrate, then it has the least parasitic capacitance. The tool provides a parasitic extraction function, which can be used for post layout simulations. However, this function did not work at the time the layout was being done.

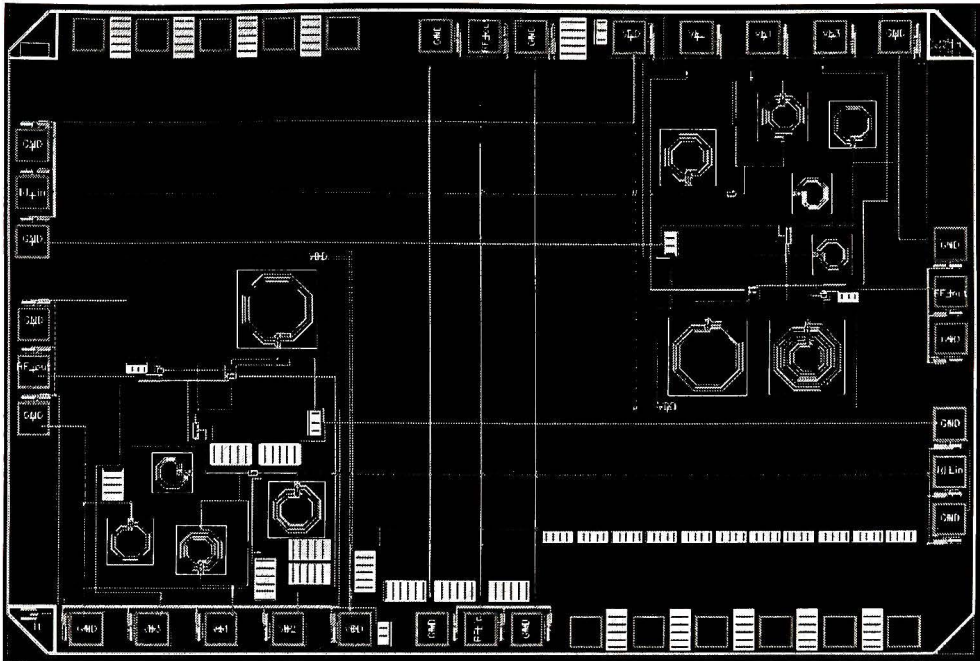


Figure 5.19. Layout of Designed LNA with and without auxiliary inductors. The one in the bottom left is the original circuit and the one on top right is the LNA after addition of both  $L_D$  and  $L_C$ .

## 5.5. Measurement Results

Figure 5.20 shows a photograph of the complete layout of two LNAs. Part "a" shows the original circuit and what is shown in part "b" is our LNA after addition of both  $L_D$  and  $L_C$ . All of inductors and top level metals can be clearly seen, which includes those are used for input matching network as well as load inductance and additional inductors,  $L_D$  and  $L_C$ . Moreover, input and output pads and DC biasing pads are clearly shown in this photograph.

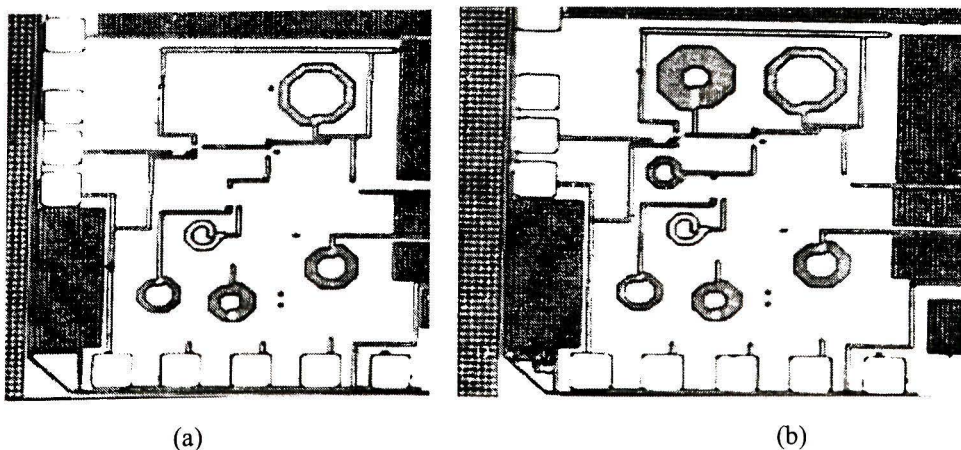


Figure 5.20. Photograph of (a) the original LNA. (b) the LNA with added inductors.

After Layout completion, post-layout simulation must be performed to see how parasitic elements due to interconnections affect the performance. At the time of submission, since the Cadence kit was not able to extract parasitic elements including capacitance, inductance and resistance, this stage was done manually. First, length and width of all metal layers that are used should be measured and then, using according coefficients for each metal layer, it is possible to estimate parasitic elements for each path. Normally, as we go to higher metal layers, both parasitic resistance and capacitance decreases. Also, metal pieces that form RF signal path have higher importance. In this layout, it is tried to use MA and E1 for the most of longer connections, and lower level metals like M1 and M2 are only used for very short paths.

Both LNAs are probed on-wafer using Cascade Microtech Ground-Signal-Ground RF probes (model 40A-GSG-150-LPW). The scattering parameters were measured using an Agilent PNA N5230a, calibrated using Open-Short-Thru-Load method with a Picoprobe CS-5 calibration substrate. The DC voltages were provided by an HP4156B Semiconductor Parameter Analyzer. The complete measurement setup is shown in Fig. 5.21.

As shown in this figure, DC voltages are provided by means of five DC probe holders which are connected to Semiconductor Parameter Analyzer. DC bias voltages could have been designed internally, however, external biasing is chosen. This is because it enables us to sweep DC voltages to compensate changes that happened to circuit due to process variations. A vacuum setup is considered to stick DC probe holders to probe station.

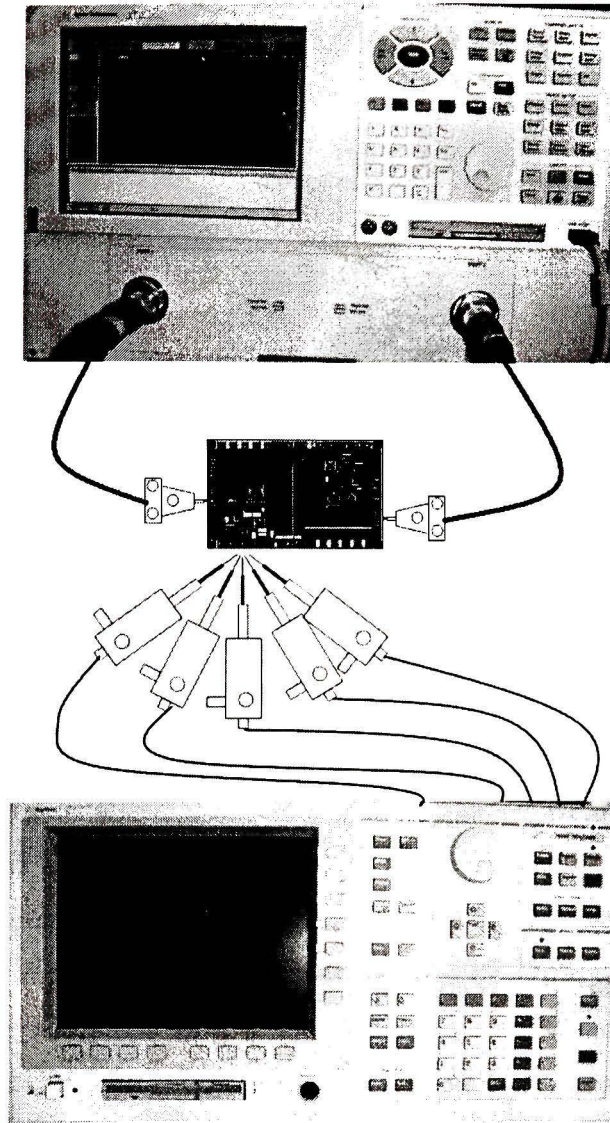


Figure 5.21. Complete test setup for the measurement of the scattering parameter

Measurement setup which is shown in Figure 5.21 is used first for calibration. For this purpose, the calibration substrate is put as Device Under Test (DUT) and after performing SOLT calibration, data is saved in a network analyzer. Then, the calibration substrate is replaced by the chip and main measurement can be done. Network analyzer automatically performs de-embedding with regards to results from calibration stage, and as a result, shown scattering parameters in the network analyzer would be the final results after de-embedding.

Also Figure 5.22 shows the probe station together with DC probe holders, which makes the test setup clearer.

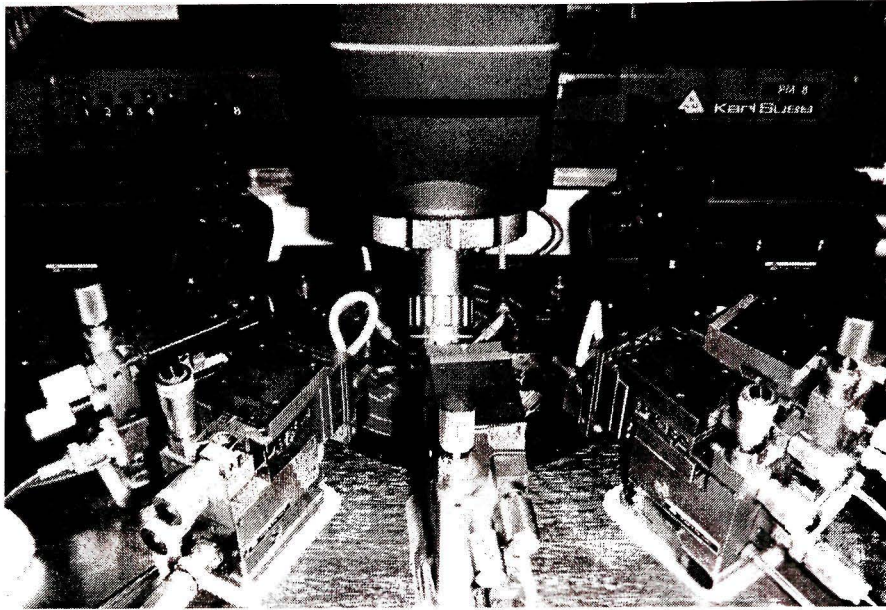


Figure 5.22. The probe station together with DC probe holders

Figure 5.23 shows simulation and measurement results of  $S_{21}$  for the designed LNA. As it is shown in this figure, measured  $S_{21}$  has almost the same flatness that simulation results predicted before. The only differences between these two curves are first, zero and pole locations and second,  $S_{21}$  magnitude in a specific range of frequency. The reason for pole and zero displacement is mainly because of reactive elements which are generated due to layout interconnections. These elements, as it was described before, are modeled manually in simulation. Consequently, it is possible that their model is not very precise, resulting in a change in poles and zeros' location. On the other hand, we have five and seven inductors for the initial and final LNAs which are designed. These inductors have been modeled in Cadence with a quality factor which is not necessarily equal to their real quality factor. Again, due to lack of modeling precision, usually quality factor of fabricated inductors are lower than simulation, and consequently, poles and zeros will be affected by this difference.

The same thing is true about  $S_{21}$  magnitude. In fact the peak value as well as  $S_{21}$  magnitude for 4.4 GHz to 8.3 GHz is about 1 dB less than simulation results and this can have several reasons.

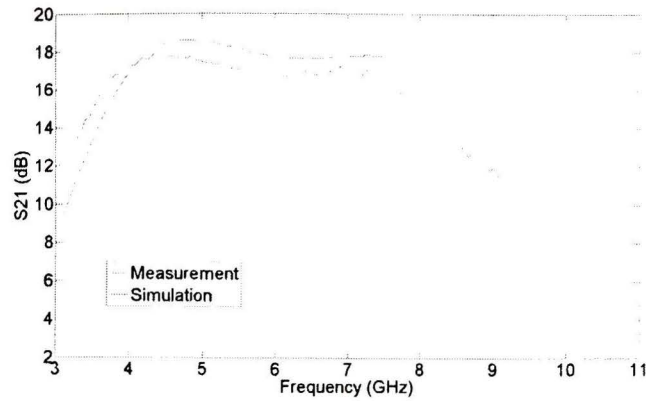


Figure 5.23. Measurement and simulation results for  $S_{21}$ .

One of the reasons can be because of modeling of parasitic resistance due to the interconnection. As it was mentioned before, this modeling is not very precise and it is possible that it has caused part of the loss. Also, normally, fabricated inductors have lower quality factor than those in simulation, resulting in more resistive part and consequently more losses due to this reason. None of above effects can be removed during calibration or de-embedding. Of course there are several loss factors such as cables and connection losses between RF and DC probes, but all of these, can be removed by de-embedding and calibration.

Figure 5.24 shows measured  $S_{21}$  for both with and without additional inductors ( $L_D$  and  $L_C$ ) and it confirms effectiveness of adding these elements which was predicted by simulation results.

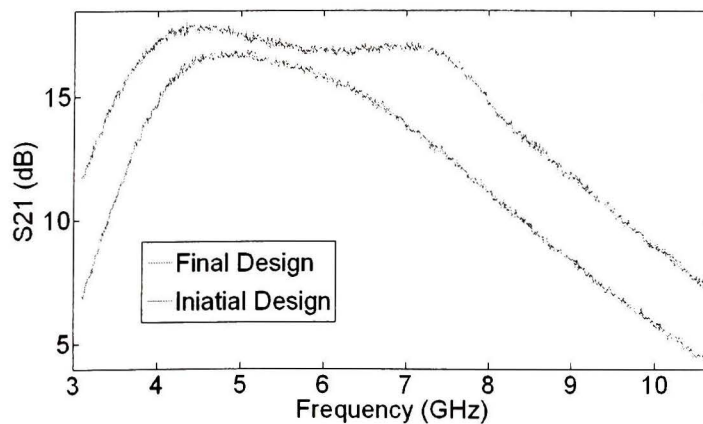


Figure 5.24.  $S_{21}$  for both LNAs. As shown, the LNA with added inductors shows flatter gain curve.

Also, Figure 5.25, 5.26 and 5.27 show input and output reflection coefficient and output-to-input isolation respectively.

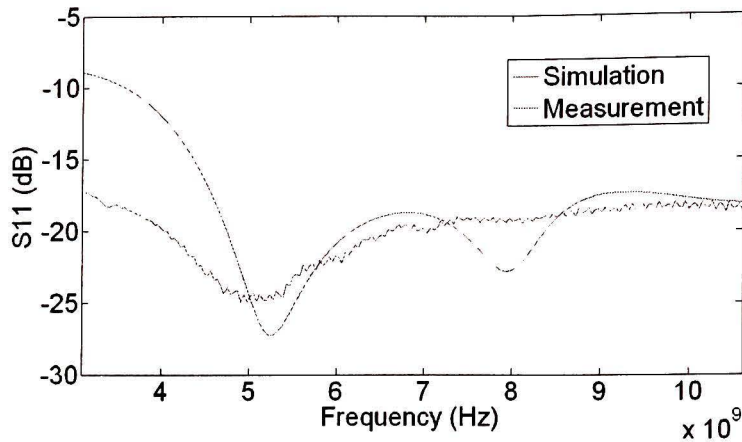


Figure 5.25. Simulation and measurement results of  $S_{11}$ .

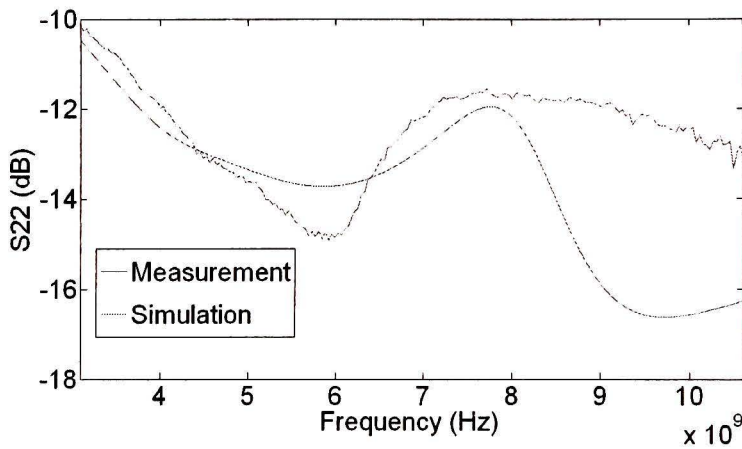


Figure 5.26. Simulation and measurement results for  $S_{22}$ .

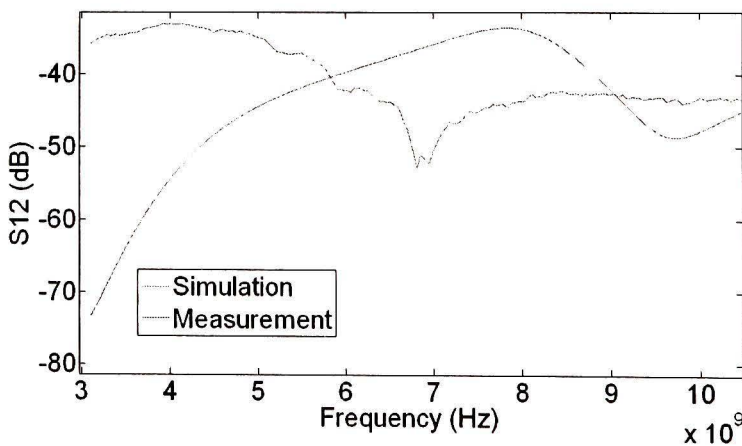


Figure 5.27. Simulation and measurement results of  $S_{12}$ .

For  $S_{11}$  and  $S_{12}$  the simulation and measurement results are not highly correlated, however, since the most important point about these parameters is being lower than a specific value, this difference is acceptable while  $S_{11}$  is lower than -10 dB and  $S_{12}$  is

lower than -30 dB. These figures show that the fabricated chip has a very good input and output matching as well as excellent out-to-in isolation.

Figure 5.28 shows the test setup for measuring noise figure of the LNA. First we need to de-embed noise which is generated due to the cables and then considering these noises, we can calculate LNA's noise. Here, first we connect noise source to one port of Agilent N8975a noise figure analyzer. Then, the cable which is connected to the output will be connected to noise source in one end, and to the second port of NF meter in the other end. Using this configuration, we can de-embed the noise cause by output cable. Next step would be addition of input cable. In this stage this cable acts as the DUT. NF meter can calculate gain of this cable which is a negative number as we expected. Also in this stage we calculate noise figure of input cable independently.



Figure 5.28.a. measurement setup for output cable de-embedding and NF-meter calibration.



Figure 5.28.b. Test setup for measurement of NF and gain for input cable.

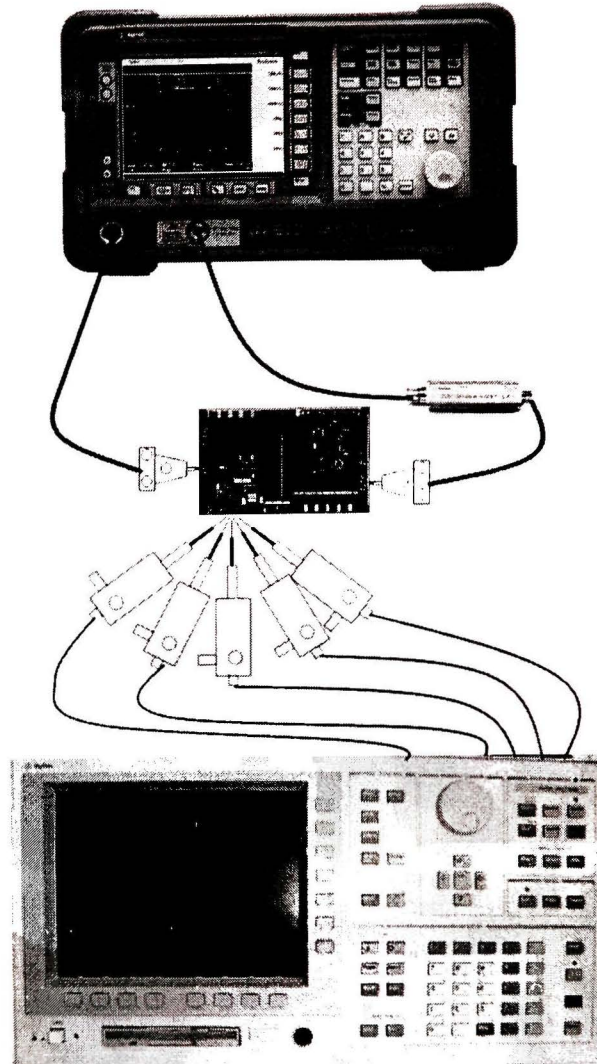


Figure 5.28.c. Test setup for LNA noise figure measurement.

Finally, when we add LNA to this setup as DUT, we can calculate noise of the whole system. This noise figure includes noise from both input cable and LNA. To calculate noise of LNA separately, we can use data from last stage and following formula for noise of a multi-stage system:

$$F_{total} = F_1 + \frac{F_2 - 1}{G_1} + \frac{F_3 - 1}{G_1 G_2} + \frac{F_4 - 1}{G_1 G_2 G_3} + \dots \quad (5.33)$$

Of course, this formula is for noise factor and we have to use noise factor in our calculations, and then, replace it with noise figure. Here,  $F_1$  is noise factor of input cable,  $G_1$  is input's cable gain and  $F_{total}$  is total noise factor that NF meter gives us. Our goal is to calculate  $F_2$  which is noise factor of LNA and after that, we can convert this value to

noise figure. Results are shown in Figure 5.29, in which simulation results are also shown for sake of comparison. The main reason for difference between simulation and measurement results is due to added noise of DC voltage supply as well as lack of precision in our calculations during de-embedding process.

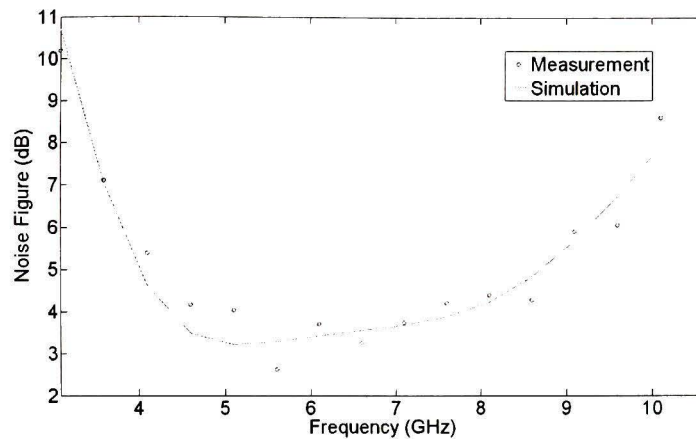


Figure 5.29. LNA's Noise figure measurement and simulation results.

## Chapter 6

# Ultra Wide Band Mixer Design

As previously mentioned, to design a UWB receiver front-end, we need a multiplier as the major block for correlation purposes. Unlike narrowband systems in which receiver has a mixer to down-convert RF signal to IF (Intermediate Frequency), for UWB systems, there is no carrier and the UWB mixer is in fact operating as a multiplier to find the correlation between two UWB pulses.

Figure 6.1 shows a typical configuration of a UWB system including the multiplier. As shown in this picture, the output signal of LNA, which is an amplified version of received signal, will be correlated with a sample signal which is generated using other correlation blocks. The output of this block will be sent to an integrator so that using its output, decision making can be performed.

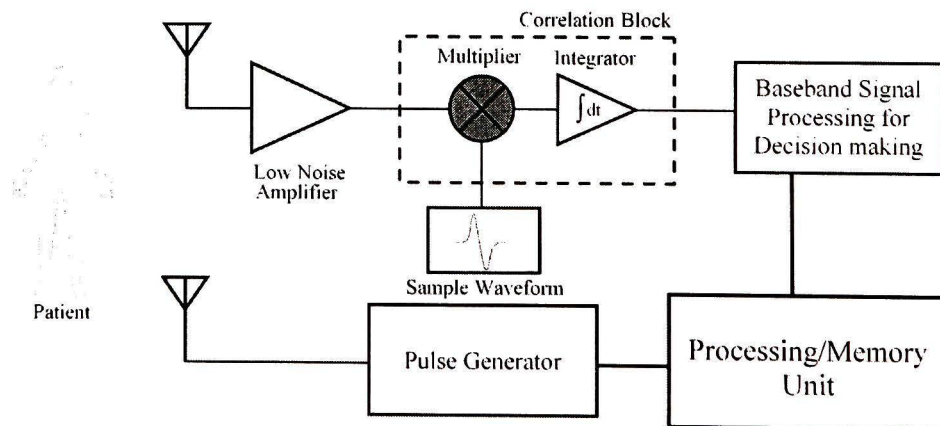


Figure 6.1. UWB Mixer in medical imaging UWB system architecture.

In our application, based on what we need from mixer, different topologies can be used. But in general, there are some specific parameters which are important in every mixer design. The main parameters\_ conversion gain, noise figure and linearity should be carefully considered in every mixer design. In some cases, depending on how we connect

the mixer, we may need to have perfect input and output matching. For wireless applications, we need our transceiver to dissipate as low as power as possible so that batteries can work longer [56, 57]. Since mixers are usually one of the most power hungry blocks in the receiver architecture, it is critical to take power into consideration during mixer design.

In this Chapter, first, we will review different types of mixers and the reasons why a mixer based on the Gilbert-cell topology is used. Next part will be a literature review of different low-power designs of the Gilbert cell. At the end of this section, the final topology used in this work will be introduced. Knowing the topology, different advantages and disadvantages will be investigated and different aspects of this design will be reviewed.

Having reviewed the topology, we will then have three sections on different parameters of the mixer, including noise, linearity, gain and matching and possible ways to optimize mixer design for these parameters. Finally, the design procedure will be explained and simulation results will be provided, followed by layout and measurement results.

## 6.1. Mixer Topologies

Based on what is commonly presented in text books on RF integrated circuit design, the mixer's main purpose is to take the RF signal from a frequency to either a higher or a lower frequency based on whether it is an up- or a down-conversion mixer. This is usually done using an additional signal which is provided by a local oscillator. The basic idea is shown in Figure6.2 below.

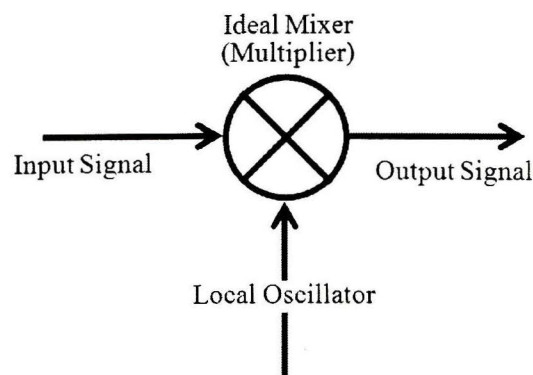


Figure 6.2. basic Idea of a Mixer

Mixing can be done using various methods from a simple transistor to a complicated double double-balanced mixer. Basically, other than the simple transistor configuration, or configurations which are based on diodes, there are a few structures which are mostly used for design of mixers.

First, we have an unbalanced mixer, which is shown in Figure 6.3. Here, we use non-linear relationship between drain current and gate-source voltage of a transistor to mix signal which is coming from M1 with signal at M2’s gate voltage. Of course, since the LO signal is off for half of the cycle, M3 is designed and its gate voltage is same as M2 but with a 180 phase shift.

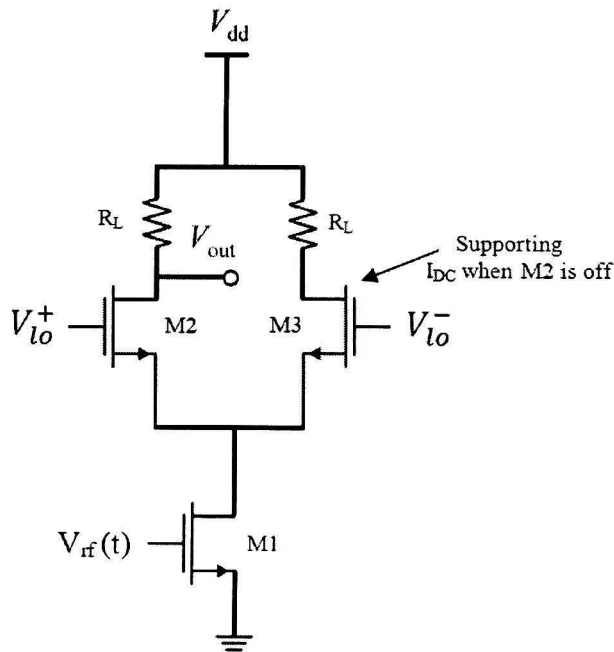


Figure 6.3. An unbalanced Mixer

The output voltage of this circuit will be [60],

$$\begin{aligned}
 V_o(t) &= V_o^+(t) = R_L(I_{DC} + g_m A_{rf} \cos \omega_{rf} t \left( \frac{1}{2} + \sum_{n=1}^{\infty} \frac{\sin\left(\frac{n\pi}{2}\right)}{\frac{n\pi}{2}} \cos(n\omega_{lo} t) \right) \\
 &= R_L \left( \frac{I_{DC}}{2} + \frac{g_m A_{rf} \cos \omega_{rf} t}{2} + \frac{2I_{DC}}{\pi} \cos \omega_{lo} t + \left( \frac{2g_m A_{rf}}{\pi} \right) \cos \omega_{rf} t \cdot \cos \omega_{lo} t + \dots \right)
 \end{aligned}
 \tag{5.34}$$

A drawback of this topology is that RF and LO feed-through, which are basically effects of these signals, will appear in the output. Also, the conversion gain for this topology will be,

$$G_c = \frac{1}{2} \frac{R_L \left( \frac{2g_m A_{rf}}{\pi} \right)}{A_{rf}} = \frac{g_m R_L}{\pi} \quad (5.35)$$

Next is a single-balanced mixer which has a differential configuration for the output voltage. This output will be the difference between drain of M2 and M3 as shown in Figure6.4.

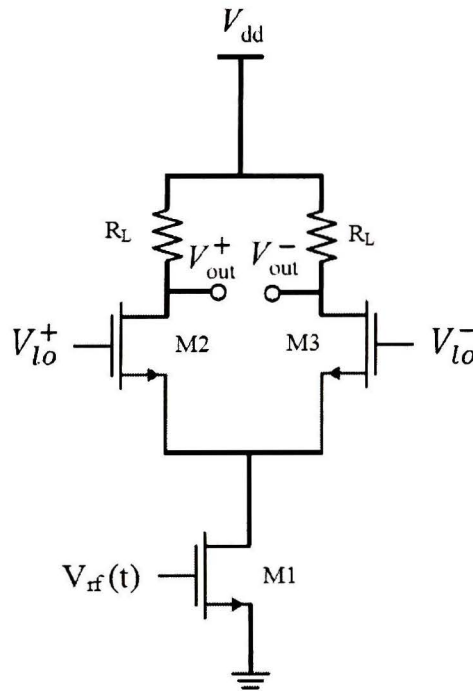


Figure6.4. Single Balanced Mixer

Here since we have a differential output, the RF component in output signal is eliminated, resulting in no RF-feed through.

$$\begin{aligned} V_o(t) &= V_o^+(t) - V_o^-(t) \\ &= 2R_L(I_{DC} + g_m A_{rf} \cos \omega_{rf} t) \left( \sum_{n=1}^{\infty} \frac{\sin\left(\frac{n\pi}{2}\right)}{\frac{n\pi}{2}} \cos(n\omega_{lo} t) \right) \quad (5.36) \end{aligned}$$

In addition, compared to unbalanced mixer, conversion gain  $G_c$  is doubled, is again a result of being differential.

$$G_c = \frac{1}{2} \frac{R_L \left( \frac{2g_m A_{rf}}{\pi} \right)}{A_{rf}} = \frac{g_m R_L}{\pi} \tag{5.37}$$

Finally, we have double balanced mixer or Gilbert Cell, which is the most popular mixer configuration. Figure6.5 shows a typical Gilbert cell in which everything including RF and LO stages are differential. Writing the output voltage equations for this circuit, we see that because of this circuit differential structures in the LO and RF stages, both RF and LO feed-throughs are eliminated, resulting in a greatly improved mixer. Here, for Figure6.5 we have,

$$I_{if+}^+(t) = \left( \frac{I_{DC}}{2} + \frac{g_m A_{rf} \cos \omega_{rf} t}{2} \right) + (I_{DC} + g_m A_{rf} \cos \omega_{rf} t) \left( \sum_{n=1}^{\infty} \frac{\sin \left( \frac{n\pi}{2} \right)}{\frac{n\pi}{2}} \cos (n\omega_{lo} t) \right) \tag{5.38}$$

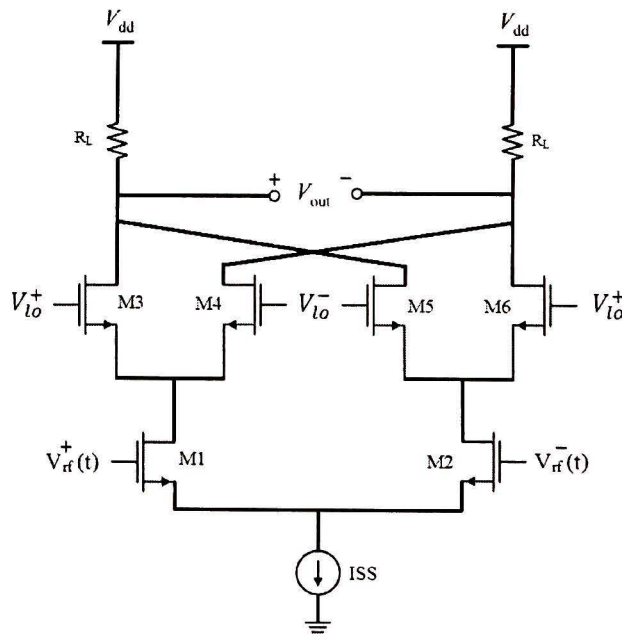


Figure6.5. Double Balanced Mixer , Gilbert Cell.

$$I_{if+}^-(t) = \left( \frac{I_{DC}}{2} + \frac{g_m A_{rf} \cos \omega_{rf} t}{2} \right) - (I_{DC} + g_m A_{rf} \cos \omega_{rf} t) \left( \sum_{n=1}^{\infty} \frac{\sin \left( \frac{n\pi}{2} \right)}{\frac{n\pi}{2}} \cos (n\omega_{lo} t) \right) \tag{5.39}$$

$$I_{if-}^+(t) = \left( \frac{I_{DC}}{2} - \frac{g_m A_{rf} \cos \omega_{rf} t}{2} \right) + (I_{DC} - g_m A_{rf} \cos \omega_{rf} t) \left( \sum_{n=1}^{\infty} \frac{\sin\left(\frac{n\pi}{2}\right)}{\frac{n\pi}{2}} \cos(n\omega_{lo} t) \right) \quad (5.40)$$

$$I_{if-}^-(t) = \left( \frac{I_{DC}}{2} - \frac{g_m A_{rf} \cos \omega_{rf} t}{2} \right) - (I_{DC} - g_m A_{rf} \cos \omega_{rf} t) \left( \sum_{n=1}^{\infty} \frac{\sin\left(\frac{n\pi}{2}\right)}{\frac{n\pi}{2}} \cos(n\omega_{lo} t) \right) \quad (5.41)$$

As a result we will have:

$$\begin{aligned} I_{if}^+(t) &= I_{if+}^+(t) + I_{if-}^+(t) \\ &= I_{DC} + 2g_m A_{rf} \cos \omega_{rf} t \left( \sum_{n=1}^{\infty} \frac{\sin\left(\frac{n\pi}{2}\right)}{\frac{n\pi}{2}} \cos(n\omega_{lo} t) \right) \end{aligned} \quad (5.42)$$

$$\begin{aligned} I_{if}^-(t) &= I_{if+}^-(t) + I_{if-}^-(t) \\ &= I_{DC} - 2g_m A_{rf} \cos \omega_{rf} t \left( \sum_{n=1}^{\infty} \frac{\sin\left(\frac{n\pi}{2}\right)}{\frac{n\pi}{2}} \cos(n\omega_{lo} t) \right) \end{aligned} \quad (5.43)$$

and finally, the output voltage will be [60]

$$\begin{aligned} V_o(t) &= R_L \cdot [I_{if}^+(t) - I_{if}^-(t)] \\ &= 4g_m A_{rf} \cos \omega_{rf} t \left( \sum_{n=1}^{\infty} \frac{\sin\left(\frac{n\pi}{2}\right)}{\frac{n\pi}{2}} \cos(n\omega_{lo} t) \right) \end{aligned} \quad (5.44)$$

It can be seen from the above equation that RF and LO feed-throughs are not present in the output signal. Finally, we have conversion gain of this circuit given by,

$$G_c = \frac{1}{2} \frac{4R_L \left( \frac{2g_m A_{rf}}{\pi} \right)}{A_{rf}} = \frac{4g_m R_L}{\pi} \quad (5.45)$$

This conversion gain is two times that of a single balanced mixer and four times that of the unbalanced mixer. Considering all of the above advantages, most of mixers designed and implemented by RF IC designers are based on this specific topology.

## 6.2. Literature review

Beside the advantages which were described for the Gilbert cell mixer, in general, circuits based on this topology dissipate more power than other topologies. In other words, power consumption is always an important issue in design of mixers based on Gilbert cell. There have been several efforts to overcome this problem, and each new idea solved the problem to some extent, but it also has its own drawbacks. Here, in this section, we will go through different circuit topologies or design techniques proposed in these works, and finally, we will introduce the chosen one to explain about its features in the next Chapter.

The first work [57] which is shown in Figure 6.6, is basically stacking a LNA below the mixer to reuse the current and share power. In this way, the power consumption of both circuits is considerably reduced. The main problem of this design is the need to increase the supply voltage to have enough voltage headroom for signal swing. With technology scaling, which results in very low voltage supplies, this idea cannot be easily implemented.

The next work [58] is similar, in which mixer is combined with an oscillator. Again for this work, mixer cell has been put on top of a VCO to reduce power consumption, but with the cost of higher voltage supply. This design is shown in Figure 6.7.

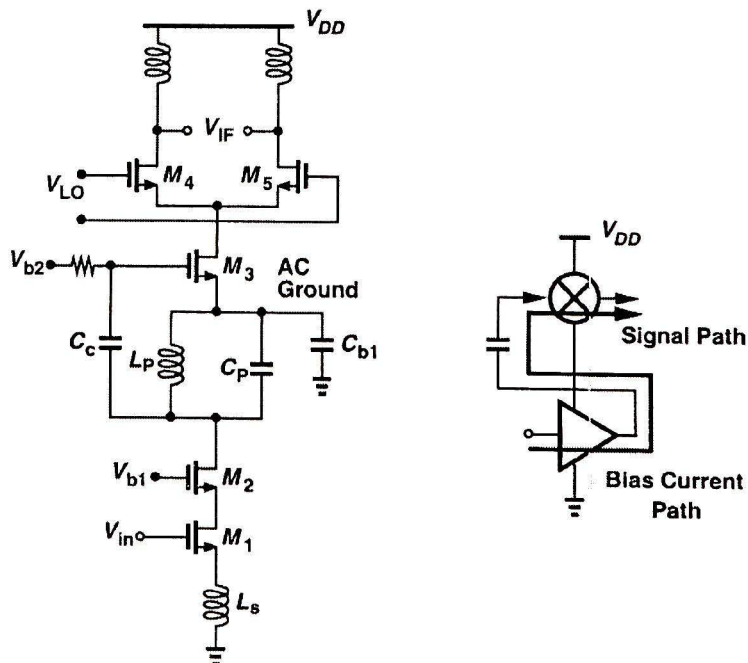


Figure 6.6. Stacked Mixer on top of an LNA proposed in [57]

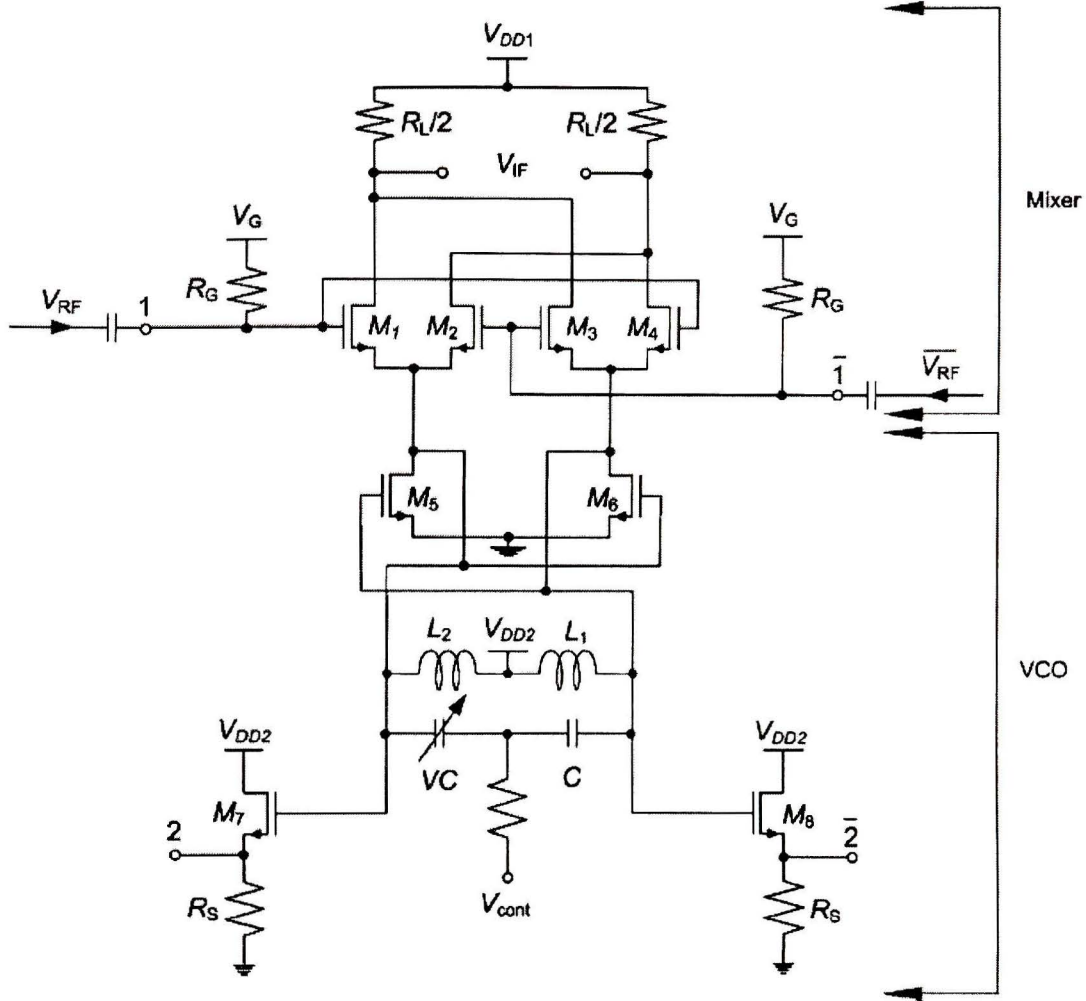


Figure 6.7. Stacked Mixer and Oscillator proposed in [58]

Beside the voltage headroom problem these two circuits need large capacitors to provide perfect AC ground, causing another disadvantage for this group of ideas. Another idea proposed in [58, 59] is to use high-Q passive components in LC tanks, to make their loss as low as possible. Since increasing the quality factor of inductors will result in narrower -3dB bandwidth, this idea is not suitable for wideband applications. Moreover, the addition of inductors or transformers will significantly increase the cost and area consumption.

Another novel idea to reduce power consumption of the mixer is using the body contact of MOSFET as the RF input terminal to achieve lower voltage supply and consequently lower power consumption. One example of this technique is reported in [60].

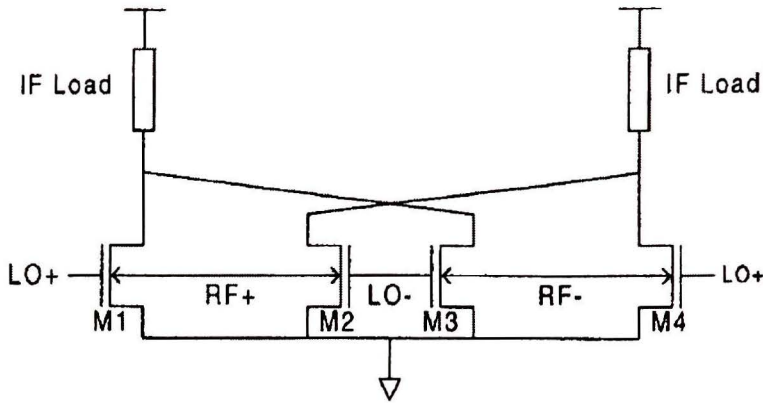


Figure 6.8. Bulk driven Mixer proposed in [60].

As we can see in above figure, since both RF and LO signals are applied to one transistor, the voltage supply can be much lower than in a conventional Gilbert cell which was shown in Figure 6.5. Although the idea looks very attractive, there are some issues which should be considered, including the need of a twin well technology as well as accurate modeling of the back gate, the parasitic p-well resistance and the deep n-well diodes.

Next group of works on improving Gilbert cell architecture, mostly focused on power reduction, are concentrated on folded structures for the Gilbert mixer. An example of this structure is shown in Figure 6.9. As we can see in this figure, since LO and RF stages are not stacked on top of each other, the voltage headroom is not an issue anymore and the power supply can be reduced to some extent, resulting in better performance in terms of power.

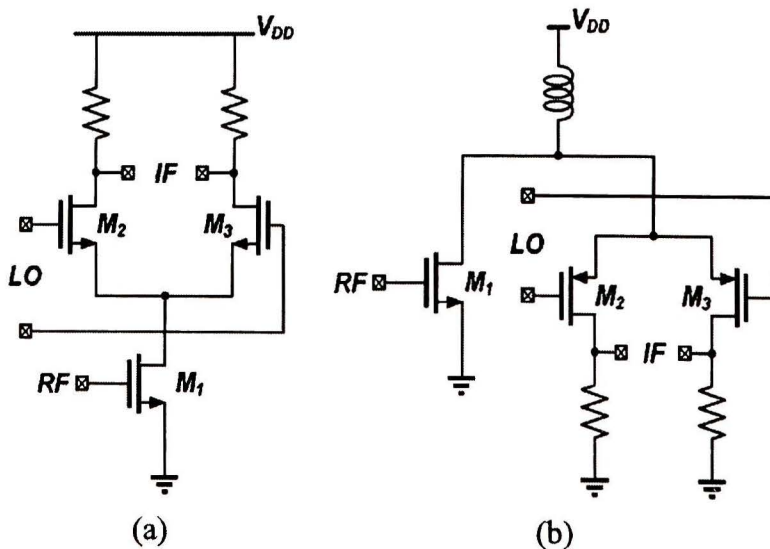


Figure 6.9. comparison of conventional and folded configurations for Gilbert cell [61].

In [61], we see an example of use of this configuration in which current reuse techniques and current bleeding are also used in their design to improve other parameters like gain and linearity. Figure 6.10 shows the design which is proposed in [61]; and since they have used mentioned techniques, power dissipation is not reduced significantly despite use of folded configuration.

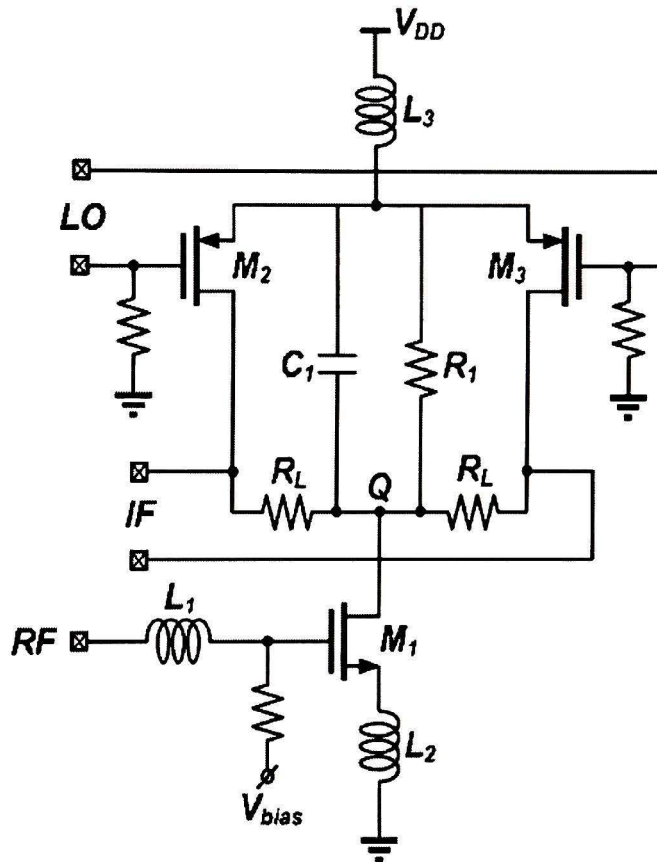


Figure 6.10. folded cascode mixer proposed by Hsieh et al in [61].

Another approach in the design of mixers is to bias the transistors in the sub-threshold region. This was done before for LNAs, and in examples like [62] the designers have significantly reduced power while keeping other parameters unchanged. This idea is also applied to Gilbert mixers in some works like [63], which resulted in much better power performance, but a drastic increase in the noise figure.

Basically, when a transistor is operating in the super-threshold saturation region, the drift mechanism is the dominant for current transport and that is the reason for quadratic relationship between drain current and gate-source voltage. On the other hand for the sub-threshold region, since diffusion mechanism dominates in current transport, the

relationship between drain current and gate-source voltage becomes exponential, which results in higher  $g_m$  to  $I_{DS}$  ratio compared to super-threshold mode. Figure 6.11 which is from [64] shows the increase of this ratio clearly.

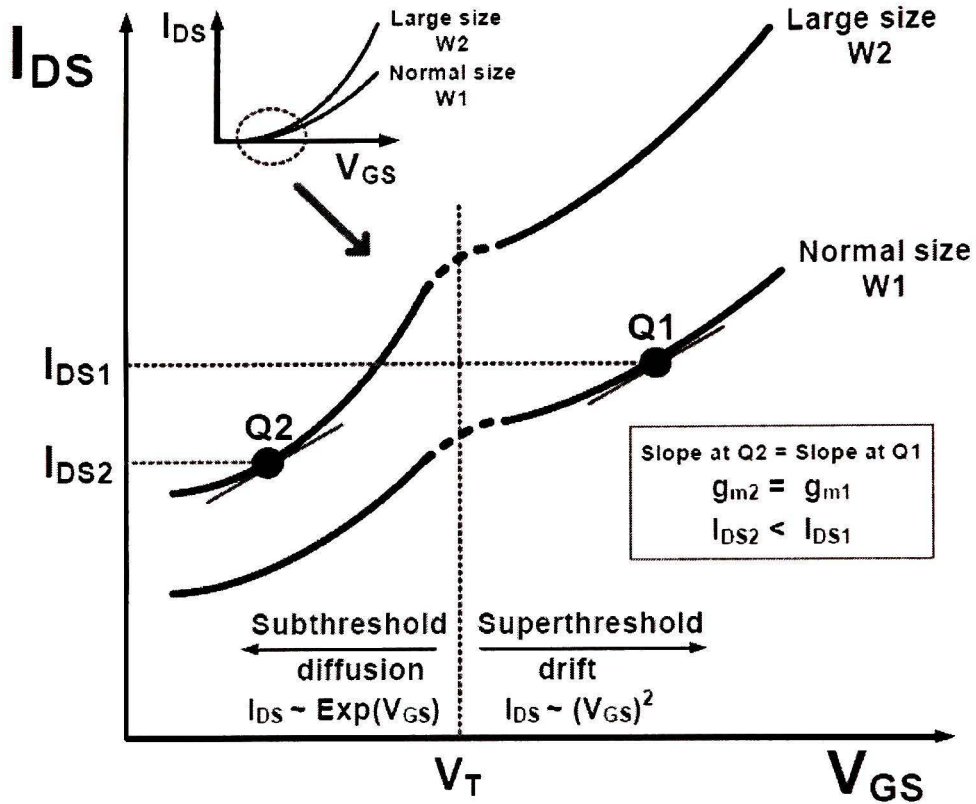


Figure 6.11. characteristic graph of drain current vs gate-source voltage around threshold voltage for two different sizes of transistor [64].

As shown in this figure, for two different transistors with two different widths, a similar transconductance can be achieved for either super- or sub-threshold regions. This means that with increasing transistor width, we can compensate  $g_m$  reduction caused by reducing gate-source voltage and as a result achieve much lower power dissipation.

In [64], a modified version of the Gilbert cell mixer is proposed and this is shown in Figure 6.12.

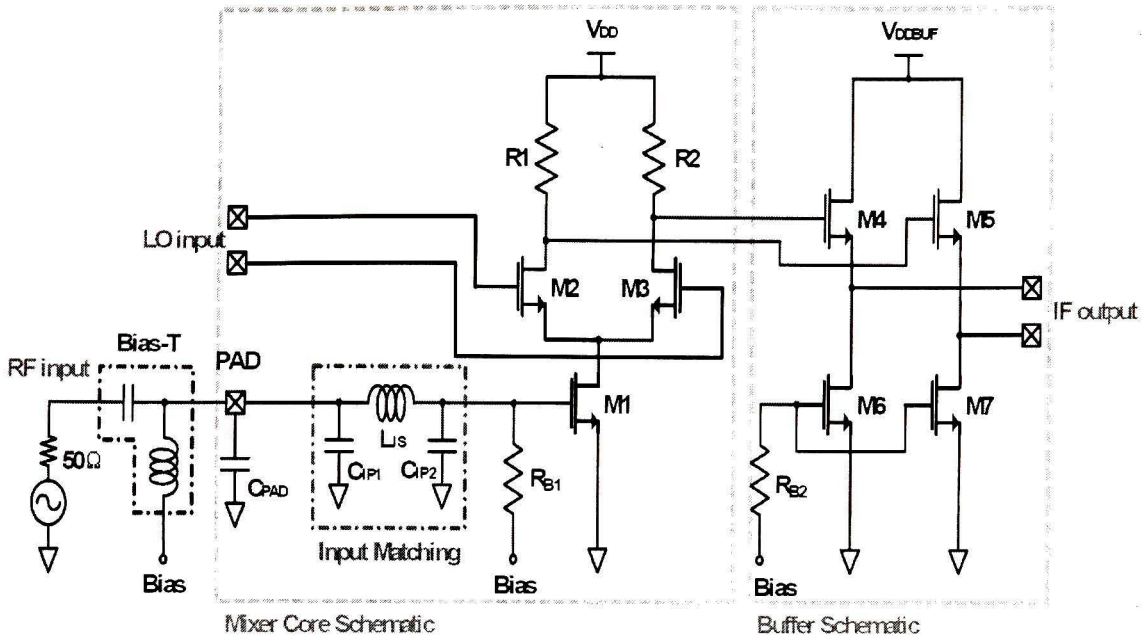


Figure 6.12. Circuit schematic proposed by Lee and Mohammady in [64].

In this circuit, the authors have biased the LO stage in the sub-threshold region to benefit from the above-mentioned advantages. In addition, since the  $g_m$  of the LO transistor becomes higher, steeper LO signal in zero crossing can be provided and as a result, conversion gain will be improved. Furthermore, as will be explained later, since the zero crossing slope of LO signal is increased, one type of switching noise which is generated in LO stage will be considerably reduced, resulting in an improvement in the noise performance.

In [65], an interesting new mixer configuration recently proposed. First, they have used a folded structure for power reduction. Also they used stacked NMOS-PMOS technology to maximize transconductance for a constant DC current. Additionally, DC decoupling is used between the LO and RF stages so that their biasing are completely independent of each other, unlike conventional Gilbert cell configuration in which, LO stage is on top of RF stage, and as a result, its biasing is related to the RF stage, so the LO current must be kept high so that enough transconductance can be provided for the RF stage. In the RF stage, we have a resistive feedback,  $R_f$ . The main purpose of this resistive feedback is to boost the bandwidth and ease the biasing since it applies self biasing to this stage. In addition, this resistor helps to achieve a good matching for the input without the need for a matching network.

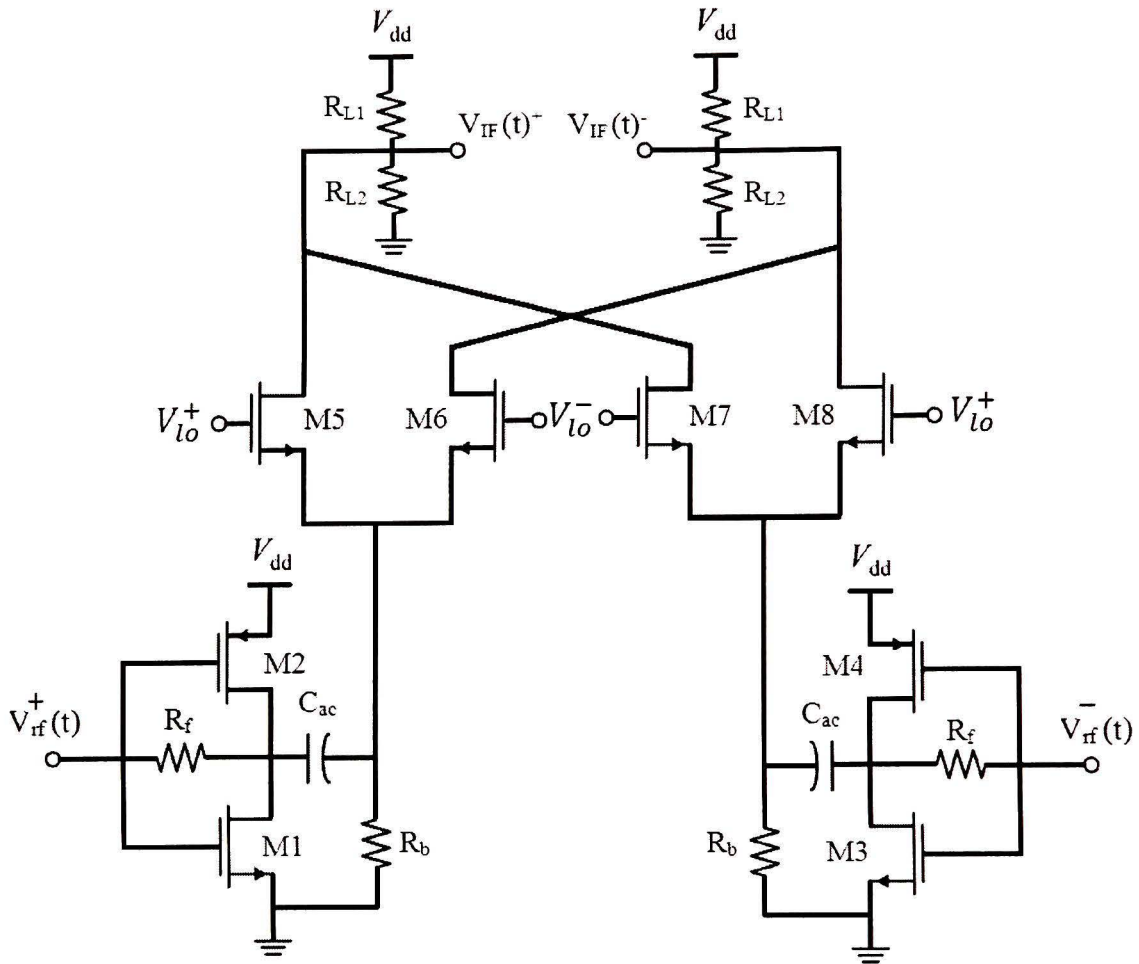


Figure 6.13. UWB folded-cascode mixer proposed in [redrawn from 65].

As mentioned before,  $C_{AC}$ 's task in this circuit is to completely decouple the RF and LO stages. There is also an interesting point in the design of the load resistance of this mixer. As shown, instead of one resistor for each half-circuit, two parallel resistors have been used so that process variations will be cancelled out. Finally we have  $R_b$  at the source of the LO switches as a path to ground for the minimum current flowing through the LO transistor because of non-ideal switching, and also for adjusting the source potential of these switches.

Considering all these advantages, the above configuration was selected for the design of the UWB mixer in this work. It should be mentioned that despite all of the advantages described, there are some serious drawbacks which should be solved for this configuration, including input matching for higher frequencies in the UWB band as well

as power consumption, which is always an issue in the Gilbert cell. In this work, we try to overcome these problems with the aid of circuit techniques or additional elements.

### **6.3. Mixer Design Parameters**

Now that we know about different mixer topologies and also selected configuration that we are going to design our block, the mixer design can start. We will first introduce the major parameters which are important in the design of mixer and then the design procedure will be explained.

#### **6.3.1. Noise Figure**

The mixer noise can be divided to three major groups\_ output load, input transconductance and switches noise. From another point of view, we can divide the mixer noise to low frequency and high frequency noise. Here, we discuss about low-frequency noise at first, and second, high-frequency noise will be investigated.

Although in our design, intermediate frequency is set at high frequencies like 100 or 200 MHz, and flicker noise is not effective in this range of frequency, but it is still instructive to know more about noise mechanisms in low-frequency since they can help in understanding high-frequency noise.

##### **6.3.1. a. Load Noise**

First, we have load noise which only happens for zero-IF receivers in which flicker noise in the loads competes with the signal [66]. This noise can be lowered by using PMOS transistors instead of NMOS since the PMOS's flicker noise is less than NMOS due to the sub-surface current transport. Also, if voltage headroom is not a serious issue in the design, poly silicon resistors can be used since they do not have much flicker noise.

##### **6.3.1. b. RF Transconductance Noise**

The next low-frequency noise generator is transconductance noise. The noise of this transistor accompanies signal and as a result will be translated in frequency. As a result, white noise and its odd harmonics will be down converted to IF or DC (in case we have a



It should be noted that this noise is independent of gate-source voltage of MOSFET based on experimental proof in [69, 70].

To make the explanation simpler and without loss of generality, we can assume that the transistors switch very fast so that with a very small change in voltage, the current changes completely from negative to positive ( or from zero to highest value), like that shown in Figure6.15.

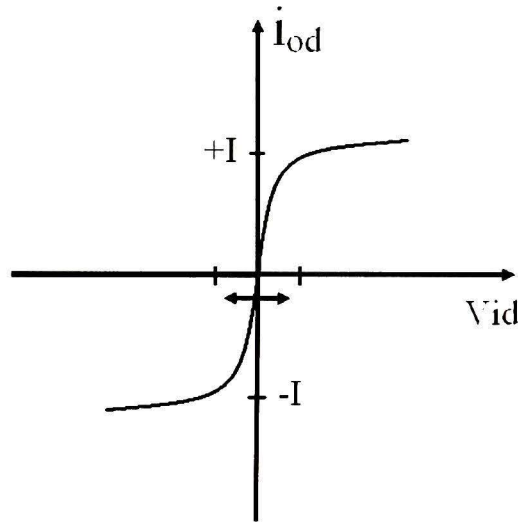


Figure 6.15. Assumed I-V characteristics of the switch.

Based on this model, when we don't have any noise, in the positive half cycle, M1 in the circuit of Figure6.14 will be on and M2 will be off. For the other half-cycle, this would be reversed. In this mode of operation, the switches act very fast. Considering noise will be like applying a modulation in the time that M1 and M2 are switching, and this will result in an advanced or a retarded zero crossings of square wave signal by,

$$\Delta t = V_n(t)/S, \quad (5.46)$$

where S is the slope of the LO voltage at the switching time. This will result in a new component in the waveform of the output in addition to LO feed-through. Spikes with random time  $\Delta t$  and amplitude of  $2I$  (which is twice the amplitude of LO square-wave) and at the frequency of  $2\omega_{LO}$  will appear in the output waveform because of switch's direct-noise. Figure6.16.b. illustrates the above explanations.

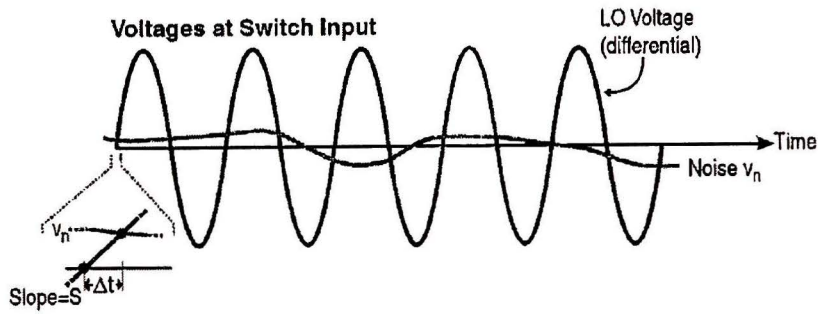
Over one period, the average value of the output current is:

$$i_{o,n} = \frac{2}{T} \times 2I \times \Delta t = \frac{2}{T} \times 2I \times \frac{V_n}{S} = 4I \frac{V_n}{S \times T} , \quad (5.47)$$

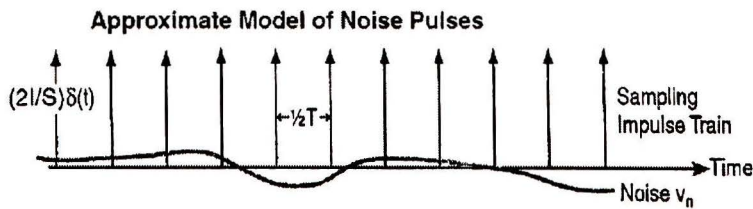
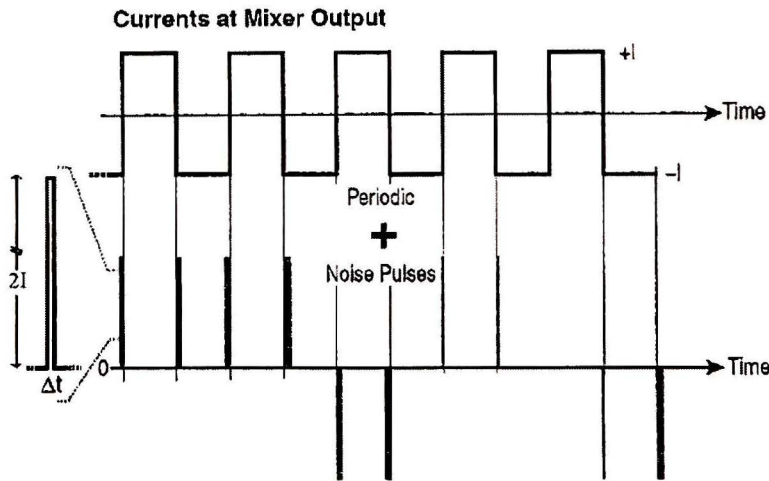
in which  $T=2\pi/\omega_{LO}$ . In [68], it is shown that considering direct noise, the frequency spectrum of the baseband noise current at the output is,

$$i_{o,n}(f) = \frac{4I}{ST} V_n(f) = \frac{1}{\pi} \cdot \frac{I}{A} \cdot V_n(f) . \quad (5.48)$$

To indicate noise figure of the circuit, the output SNR (signal-to-noise ratio) is a good candidate. In [68], it is shown that the SNR for the output is:



(a)



(b)

Figure 6.16.a switch input voltage, b. mixer output current decomposed into noiseless response and pulse of noise. [68]

$$SNR_1 = \frac{S \times T}{2\pi(V_{GS} - V_t)} \cdot \frac{V_{in}}{V_n} = \frac{2A}{(V_{GS} - V_t)} \cdot \frac{V_{in}}{V_n} \tag{5.49}$$

in which  $A$  is the LO's amplitude. Using this equation, it is noted that increasing the waveform slope at the zero crossing,  $S$ , as well as its period, improves the SNR, or, in other words, the noise performance. Although, all the above calculations were performed for a single-balanced mixer, they are also true for a double-balanced (Gilbert Cell) except for the LO feed-through which does not appear in the output in a Gilbert mixer. Figure 6.15 shows the mixer's output spectrum in the presence of direct noise for a single balanced mixer. For the Gilbert cell, there is no component in the LO frequency since the LO feed through does not exist.

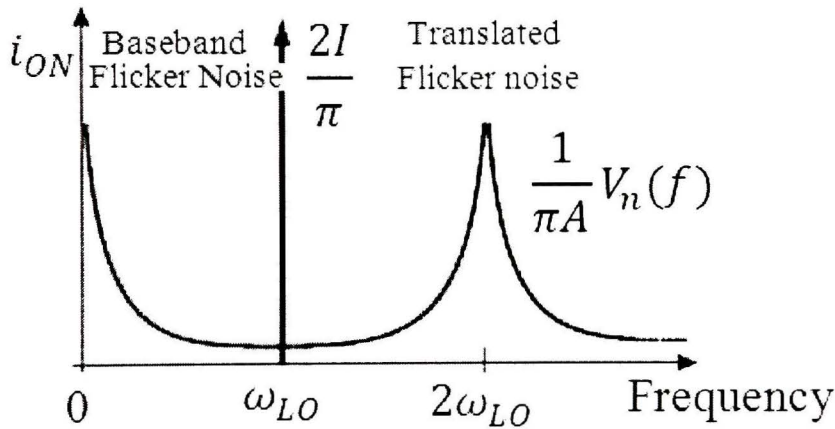


Figure 6.17. Mixer output spectrum in presence of direct noise. [68]

**6.3.1.d. Indirect Noise**

The previous explanations show that flicker noise or low-frequency noise in the output can be eliminated if we have an ideal square-wave LO waveform which has an infinite slope at zero-crossing. On the other hand, an increasing slope will result in some consequences which will cause another mechanism for noise that depends on the frequency and the circuit's capacitance and this is called “indirect noise”.

To explain the indirect noise mechanism, using again the single balanced mixer shown in Figure 6.14 is instructive. As shown in this figure, the noise of the switches is modeled in the gate of one of the transistors. In this way, when M1 is on, both  $V_n$  and the biasing voltage  $V_H$  are in its gate, but in the second half-cycle, when M2 is turned on, only  $V_H$

appears in its gate. Considering this, we can calculate voltage in the source of the switches, with the assumption of a source follower stage. This voltage charges exponentially to  $V_n$  in one half-cycle, and it discharges to zero in the other, as shown in Figure6.18.a.

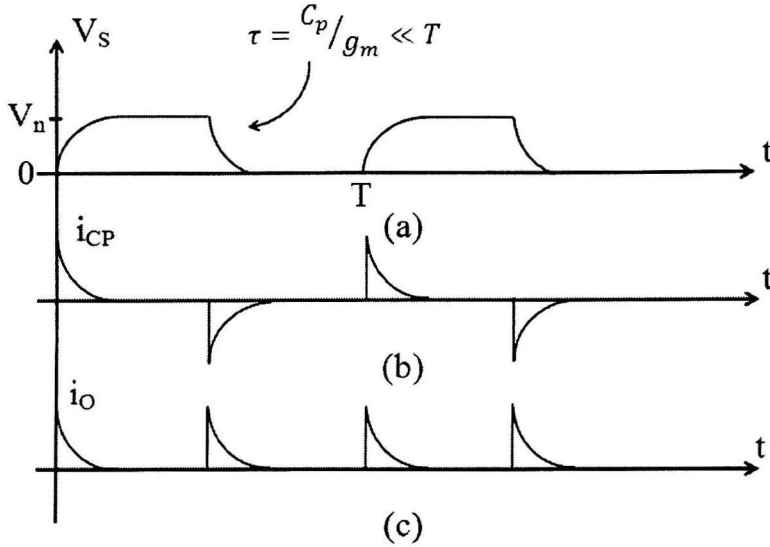


Figure6.18. Waveforms resulting from a square-wave LO: (a) voltage at tail, (b) capacitive current, and (c) output current [68].

As shown in Figure6.18.b, this voltage will result in current generation in the equivalent parasitic capacitance of the tail which has the same frequency as the LO signal, but with zero DC value. Finally, this current will result in a noise current in the output with double the LO's frequency. The amount of flicker noise is the average of the output current and is given by,

$$i_{o,n} = \frac{2}{T} \int_0^{T/2} i_{cp}(t) dt = \frac{2}{T} \int_0^{T/2} C_p \left[ \frac{d}{dt} V_s(t) \right] dt . \quad (5.50)$$

Therefore, the output noise current will be,

$$i_{o,n} = \frac{2}{T} C_p \left( V_s \left( \frac{T}{2} \right) - V_s(0) \right) = \frac{2}{T} C_p V_n . \quad (5.51)$$

Using these results and as it is calculated in [68], the signal-to-noise ratio will be:

$$SNR_3 = \frac{g_m \frac{2}{\pi}}{2 f_{LO} C_p} \times \frac{V_{in}}{V_n} = 2 \frac{f_T}{f_{LO}} \cdot \frac{V_{in}}{V_n} . \quad (5.52)$$

It should be mentioned that all of these expressions are calculated with the assumption of square wave signal for the LO input. In the case of a sinusoidal LO input, these expressions will be changed.

For the high-frequency case, white noise can be calculated using same explanation of low-frequency noise. Basically, switches contribute to the noise when both of them are ON. If one of switches is OFF, then it acts as a cascode transistor in which its tail current is of constant value  $I$  and a fixed by RF transconductance stage. This means that the sampling window, to consider a pulse train, is when both switches are on, or

$$T_S = \Delta V/S. \quad (5.53)$$

This means that the switch's noise is transferred to the output only at each zero crossing. Assuming a sampling function given by

$$p(\omega_{LO}t) = \sum_n G_m \left( t - \frac{nT}{2} \right), \quad (5.54)$$

in which  $G_m$  is periodic at twice the LO frequency, then the mixer output noise will be [68],

$$i_{o,n} = p(\omega_{LO}t).V_n(t). \quad (5.55)$$

Also, in [68], it is shown that power spectral density of output current noise due to one switch is

$$i_{o,n}^2 = 4kT\gamma \frac{4I}{ST}. \quad (5.56)$$

This equation is very interesting since it states that noise density of switches only depends on the LO amplitude, and the bias current and transistor size does not have any effect on it. Finally, as calculated in [68] using extensive mathematics, the total white noise at the mixer output will be

$$V_{o,n}^2 = 8kTR_L \left( 1 + \gamma \frac{R_L I}{\pi A} + \gamma \frac{g_m R_L}{2} \right). \quad (5.57)$$

In this equation, the first term is the output load noise, the second term is due to switches and the last term is the noise generated because of the transconductance stage. This equation changes as written below for the Gilbert cell since in that configuration, the number of elements are twice that of the single balanced mixer:

$$V_{o,n}^2 = 8kTR_L \left( 1 + \gamma \frac{2R_L I}{\pi A} + \gamma g_m R_L \right). \quad (5.58)$$

Using this equation, it is possible to optimize the noise figure of the mixer since we know that which parameters affect the noise figure.

Now that we know enough about the noise mechanism of a mixer, it is easier to investigate the noise performance of our selected design. As explained above, the switch noise due to direct mechanism can be expressed as.

$$i_{o,n(dir)} = 4I_{dsRF} \frac{V_n}{S.T}, \quad (5.59)$$

in which  $V_n$  is

$$V_n = \sqrt{2 \frac{K_f}{WLC_{oxf}}}, \quad (5.60)$$

and  $K_f$  is a process parameter. This equation shows that by increasing the switches size as well as reducing DC current the noise will be less. On the other hand, if the switches become larger in size, then their parasitic capacitances will be larger; consequently, as was described for the indirect noise mechanism, this noise, which is given in following equation for a sine-wave, will be higher

$$i_{o,n(ind)} = \frac{2C_p}{T} V_n \cdot \frac{(C_p \omega_{LO})^2}{g_{m,sw}^2 + (C_p \omega_{LO})^2}. \quad (5.61)$$

What is discussed above shows clearly that decoupling the RF and LO stages can help in optimizing the noise performance of mixer, especially noise due to the switches

### 6.3.2. Gain and Linearity

As mentioned before during the introduction of the Gilbert cell, the gain of a mixer based on Gilbert cell and considering LO signal as a square wave is.

$$G_c = \frac{1}{2} \frac{4R_L \left( \frac{2g_m A_{rf}}{\pi} \right)}{A_{rf}} = \frac{4g_m R_L}{\pi} \quad (5.62)$$

in which  $A_{rf}$  is the amplitude of the RF signal. This equation suggests that to increase mixer's conversion gain, the transconductance of the RF transistors should be increased.

Usually, a constraint for increasing  $g_m$  is power, but here in this circuit, even if power is allowed to be increased up to an specific value, it is not guaranteed that we will be able to increase the conversion gain. Assuming that  $g_m$  is increased by making the RF transistor bigger (higher values for the width of the transistor), the parasitic capacitances of the MOSFET will be higher. On the other hand, we have the decoupling capacitor,  $C_{ac}$ , which is connected to the connecting node of the NMOS and PMOS RF transistors. Later in this Chapter, using mathematical expressions for the input impedance, at higher frequencies, the high values of capacitance from this node to ground will result in serious problems for input impedance matching. For smaller sizes of the transistors, this problem is not very serious, but as transistors' sizes increases to boost conversion gain, impedance matching for higher frequencies becomes worse. To solve this problem, two solutions for impedance matching have been proposed in this work. These solutions are described in next parts of this Chapter. Solving the matching problem, it will be possible to increase the conversion gain up to values which are allowed by power constraints.

On the other hand, using Volterra series, it is shown in [60] that the third harmonic distortion of a Gilbert cell can be expressed as,

$$\begin{aligned}
 HD_3 &= \frac{I_{rf}^+ |3rd\text{-order term}|}{I_{rf}^+ |fundamental|} \approx \frac{1}{4} \left| \frac{\alpha_3}{\alpha_1} \right| A_{rf}^2 = \frac{1}{4} \frac{\left| -\frac{1}{8} \sqrt{\frac{K}{I_{SS}}} \right|}{\sqrt{\frac{I_{SS}}{K}}} A_{rf}^2 \\
 &= \frac{1}{32} \frac{K}{I_{SS}} A_{rf}^2 = \frac{1}{32} \frac{\mu_{eff} C_{ox} (W_{eff}/L_{eff})}{I_{SS}} A_{rf}^2 .
 \end{aligned} \tag{5.63}$$

And the third-order inter-modulation component is

$$\begin{aligned}
 IM_3 &= 3HD_3 = \frac{3}{32} \frac{K}{I_{SS}} A_{interface}^2 \\
 &= \frac{3}{32} \frac{\mu_{eff} C_{ox} (W_{eff}/L_{eff})}{I_{SS}} A_{interface}^2 .
 \end{aligned} \tag{5.64}$$

Note that  $IM_3$  should be as low as possible. The amplitude of input third order intercept point is:

$$A_{IP3} = \sqrt{\frac{4}{3} \left| \frac{\alpha_1}{\alpha_3} \right|} = \sqrt{\frac{4}{3} \frac{\left| \sqrt{\frac{I_{SS}}{K}} \right|}{\left| -\frac{1}{8} \sqrt{\frac{K}{I_{SS}}} \right|}} = \sqrt{\frac{32}{3} \left( \frac{I_{SS}}{\mu_{eff} C_{ox} (W_{eff}/L_{eff})} \right)}. \quad (5.65)$$

and for this circuit IIP3 will be,

$$iIP3 = 4 \sqrt{\frac{2 I_{ds,RF}}{3 K_{RF}}}, \quad (5.66)$$

in which  $I_{ds,RF}$  is drain current of the RF transistors and  $K_{RF}$  is the process parameter given by

$$K_{RF} = 2\mu C_{ox} \frac{W}{L}, \quad (5.67)$$

where  $\mu$  is the carrier mobility. As a result, increasing the DC current improves also the linearity too. Furthermore, it is well-known that increasing the drain-source current of an RF MOSFET considerably improves its noise performance. Putting all of these facts together shows that increasing the DC current helps improving every important parameter in a mixer design. But when the DC current increases, the voltage across the load resistance also increases. Consequently, less voltage headroom remains for the output signal to swing. In other words, although the equations might suggest that increasing bias current helps linearity, we can see that eventually it will result in degradation in linearity. In the literature, there are many works on improving a mixer's linearity. Among them, the charge-injection method proposed in [71] is one of the more popular ones. In [71], the basic idea is to provide the required current for the RF stage to improve gain and linearity, bypassing switches which are basically commutating MOSFETs. Figure6.19 shows main idea proposed in [71].







Since the LNA's output is designed to be matched with a  $50\Omega$  load, the input impedance of the mixer should have the same value. In our mixer architecture, which is demonstrated in Figure6.13,  $R_f$  is the element responsible for input impedance matching. By adjusting  $R_f$ , we can easily achieve impedance matching for a wide band of frequency. On the other hand, simulation results show that for higher frequencies, we might face problems regarding impedance matching. This is shown in Figure6.23.

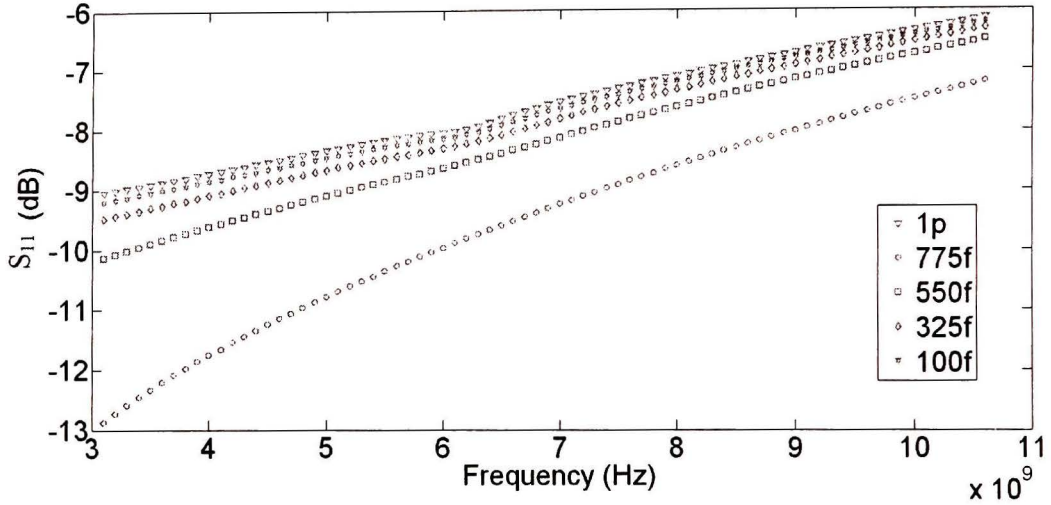


Figure 6.23.  $S_{11}$  of Mixer in Figure6.13 for different  $C_{ac}$  values.

As we can see in this figure, input impedance matching is related to frequency in a way that it gets worse as the frequency increases. Figure6.23 also shows another fact, that decreasing  $C_{ac}$  results in improving  $S_{11}$  for lower frequencies, but for higher frequencies, it does not have any significant effect. Also, it will be shown later that decreasing this capacitor under one pF might result in degradation in the conversion gain. Since this problem is directly related to frequency, changing  $R_f$  does not solve it, as also confirmed with simulation results. To find a proper solution, the best way is to write the input impedance equation. In the circuit shown in Figure6.13, we have,

$$Z_1 = Z_{C_{ac}} + (R_b \parallel \frac{1}{g_{m5}} \parallel \frac{1}{g_{m6}}) = \frac{R_b}{(1+R_b)(g_{m5}+g_{m6})} + Z_{C_{ac}} = \frac{R_b}{SR_b C_{ac} + (1+R_b)(g_{m5}+g_{m6})} \quad (5.68)$$

$$Z_2 = R_f \parallel C_{gs2} \parallel C_{gd1} = \frac{R_f}{1 + SR_f(C_{gs2} + C_{gd1})} \cong \frac{R_f}{1 + SR_f C_{gs2}}, \quad (5.69)$$

and

$$\begin{aligned}
Z_3 &= Z_1 || Z_{sb1} || Z_{db2} \\
&= \frac{R_b}{(1 + R_b)(g_{m5} + g_{m6}) + SR_b(C_{ac} + C_{db1} + C_{sb2})}.
\end{aligned} \tag{5.70}$$

Assuming that,

$$g_{m5} = g_{m6} \ \& \ R_b \gg 1 \ \& \ C_{ac} \gg C_{db1}, C_{db2}, \tag{5.71}$$

we can rewrite  $Z_3$  as,

$$Z_3 \cong \frac{1}{2R_b g_{m5} S C_{ac}}. \tag{5.72}$$

As a result  $Z_{in}$  will be:

$$\begin{aligned}
Z_{in} \\
&= \frac{1 + SR_f C_{gs2} + 2R_f R_b g_{m5} C_{ac}}{(1 + SR_f C_{gs2})(2SR_b g_{m5} C_{ac}) + S(C_{gd2} + C_{gs1})(1 + SR_f C_{gs2} + 2SR_f R_b g_{m5} C_{ac})}
\end{aligned} \tag{5.73}$$

The above equation can be simplified assuming that,

$$\begin{aligned}
C_{gs1} &\gg C_{gd2}, \\
R_f C_{gs2} &\ll 2R_f R_b g_{m5} C_{ac}, \\
\text{and } 2R_b g_{m5} C_{ac} &\gg C_{gs1}.
\end{aligned}$$

To following equation:

$$Z_{in} = \frac{1 + 2SR_f R_b g_m C_{ac}}{2S^2 R_f R_b g_{m5} C_{ac} (C_{gs1} + C_{gs2}) + 2S g_{m5} R_b C_{ac}} \tag{5.74}$$

As we can see from the above equation, the magnitude of the input impedance will decrease as the frequency increases. In addition, the real part of this impedance can be written as:

$$Re\{Z_{in}\} = \frac{2S^2 R_f R_b g_m (C_{gs1} + C_{gs2}) + 4SR_f R_b^2 g_{m5}^2 C_{ac}}{\left[4 \left(R_f R_b g_{m5} (C_{gs1} + C_{gs2})\right)^2 S^2 - 4(g_{m5} R_b)^2\right] C_{ac}}. \tag{5.75}$$

This expression shows the dependence of the real part of the input impedance on the frequency. Based on the above explanations, it can be seen which parameters affect the input impedance and the magnitude of this effect.

On the other hand, as mentioned before, sweeping the coupling capacitor shows that if this capacitor becomes smaller than a specific value, it cannot be considered as a short

circuit during small-signal analysis. This makes impedance matching even harder since increasing the capacitor will result in worse matching as it is shown in Figure 6.23.

In this work two solutions have been proposed. The first one is to add an inductor to compensate the capacitive effect of  $C_{ac}$  in a way that the input impedance will not be linearly dependent on frequency. Adding an inductor in series with  $R_f$  affects the frequency dependent part of the input impedance in a way that perfect impedance matching is achievable for the whole bandwidth, as shown in Figure 6.24.

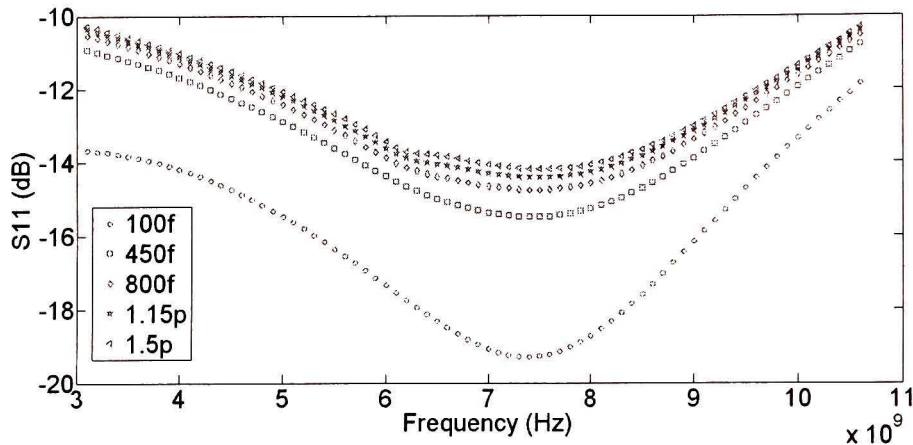


Figure 6.24. input matching after addition of auxiliary inductor.

As shown in this figure, very good matching is achieved for a large enough capacitance which won't result in any degradation in conversion gain. On the other hand, simulations show that the added inductors in both ends have inductance of less than one nH which means very good quality factor and low-loss. These advantages will result in the ability to design inductors precisely to cancel capacitive effects, while being very low-loss, which will result in a very small degradation in the noise figure. Noise simulations confirm this expectation. A major disadvantage of adding the inductor is increasing the chip area. The other solution which is implemented in this work is based on adding an active balun which converts single-ended to differential inputs. Different configurations are proposed for balun, among them, some are very complicated and also include inductor which makes them not suitable for our application. An example is described in [73]. On the other hand, some designs are relatively simple as well as being inductor-less. The balun which is used in this work is shown in Figure 6.25.

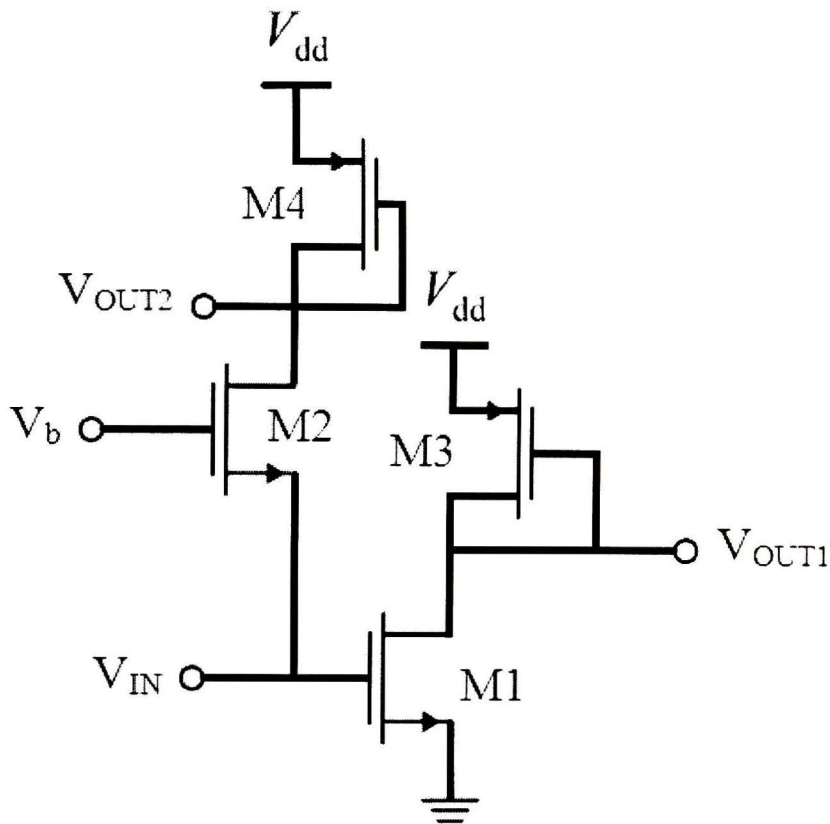


Figure 6.25. Active balun designed for input network of mixer.

In designing of this balun, it should be recalled that the balun must have a good performance for the entire band. In fact, a reason that active elements are used is the wideband nature of our design because passive components like inductors limits the bandwidth of a circuit.

Since the input signal is applied to both common-source and common-gate stages, input matching can be easily achieved by adjusting the transconductance of the CG transistor since input impedance of this circuit is inversely related to  $g_m$  of this transistor. Also, regarding to the freedom that we have in selecting the components' sizes, the output impedance of this circuit is very flexible and it can be designed to be in a perfect match with the input impedance of mixer.

In addition to these advantages, because active components' are used, this balun can also increase the conversion gain of our mixer. Also, since no inductor has been used, the added area is very small. In addition to these advantages, since number of inputs will be reduced by one, it is very helpful in saving area when we are drawing the layout. To make it clearer, since each signal input needs a pad for signal and two pads for grounds,

having two RF and two LO inputs will result in 12 pads which should be one side of the chip. Eliminating two of these signals will result in area savings of 50%, which is very significant.

Despite all of the above advantages, adding active balun has its drawbacks. Since we are using active elements the noise figure will be significantly affected. In this case, Figure 6.26 shows difference between noise figure curves before and after applying the balun. This difference means that this solution is not appropriate for impedance matching.

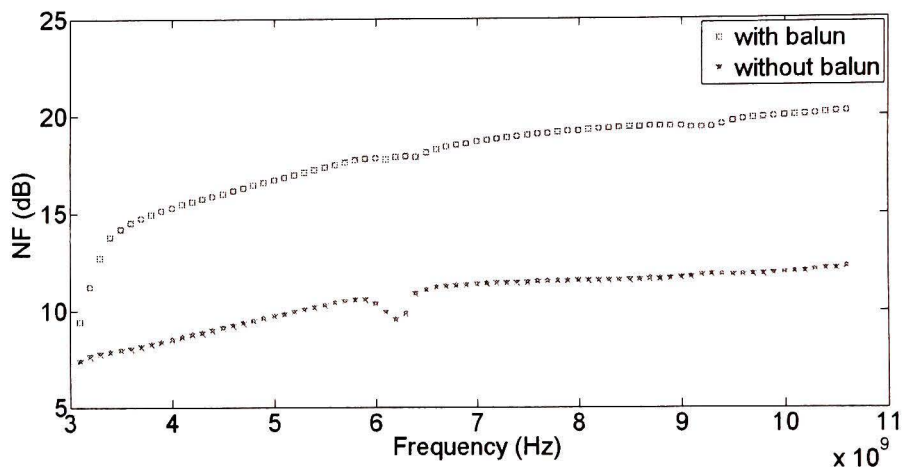


Figure 6.26. Noise figure before and after addition of balun. As it is shown, adding balun will result in a significant increase in noise figure.

Furthermore, conversion gain is affected by the balun too. Since balun's gain decreases with increasing frequency, and considering that the mixer's conversion gain has the same behavior, adding a balun will result in losing gain flatness. As a result, although the gain will be increased for lower frequencies, it will be decreased much faster than original gain when the frequency increases. This is shown in Figure 6.27.

Considering noise and gain problems that are caused because of balun, it seems that first approach which was based on adding an inductor was a better solution. In fact each solution has its advantages and disadvantages, but the first solution seems to have fewer drawbacks.

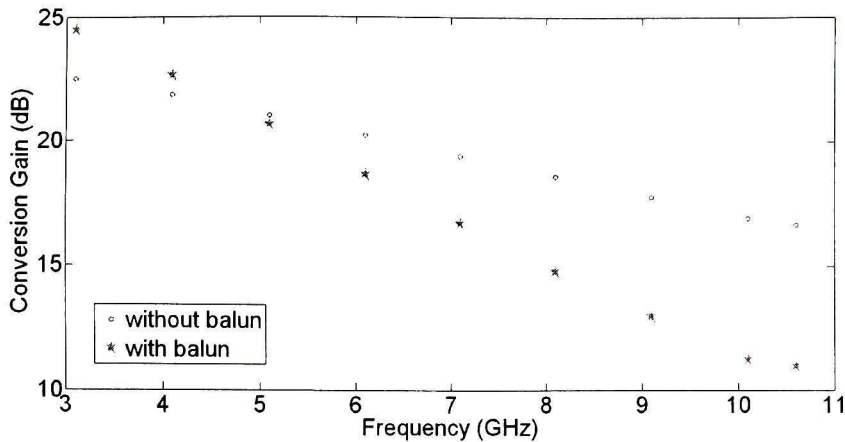


Figure 6.27. Mixer's Conversion gain before and after addition of balun. It is demonstrated that for lower frequencies, conversion gain increases with balun but it decreases much faster than original mixer for higher frequencies.

In this design since we needed to decrease number of pads for input signal, our only choice was using baluns. On the other hand, since the balun was not a part of the designed mixer, it was fabricated as a test structure to be de-embedded. This means that after measurement, the noise figure, gain and other performance parameters of mixer core will be calculated by de-embedding the balun. Considering that the balun has to be added for our circuit, there is no need to add inductor anymore, since the impedance matching problem is solved using the balun.

## 6.4. Design Procedure

Now that all the important parameters have been described, the design steps can be performed. In this work, two approaches for the design are pursued. In the first approach, the RF transistors are designed in super-threshold mode and in the second one, sub-threshold region is selected for operation of these devices. The advantages and disadvantages of sub-threshold biasing of transistors are discussed previously in this Chapter. For each design parameter, results of these approaches are compared. Generally speaking, significant improvement is achieved in power consumption during transition from super threshold to sub-threshold. On the other hand, conversion gain, noise figure and linearity are degraded. Of course all of them have very acceptable performance in comparison with other publications. Impedance matching also remains almost the same.

Since the RF and LO stages are decoupled, their design can be performed independently. For the RF stage and in super-threshold mode, the most important criterion is achieving a high conversion gain. Both NMOS and PMOS, transistors are designed in a way that they have high transconductances. Of course, our constraint in this step is power consumption, which should be kept as low as possible. For the sub-threshold approach, the voltage supply of this stage is not  $V_{dd}$  anymore and it can be reduced considerably or as much as needed. Since the devices are biased in sub-threshold region and low-power performance is the most important target, the NMOS and PMOS transistors in this stage cannot have a transconductance as large as it could be achieved for the super-threshold approach. As a result the conversion gain is lower for the super-threshold case.

Power consumption is again a constraint in design of the LO stages. An optimum point should be found in a way that power consumption requirements are achieved while switches operate fast. It was explained earlier in this Chapter how we can design switches and provide the LO signal in a way that the noise figure will have its optimum value.

Next is the load stage and output buffer which are required for measurement purposes and output matching. As described before, the loads are designed in a way to be immune to process variations. The load value directly affects conversion gain, and higher loads will result in higher gain. On the other hand, a higher load will result in a large voltage drop and consequently poor linearity. Figure 6.28 shows the comparison of designed mixer between noise performance of super and sub-threshold modes.

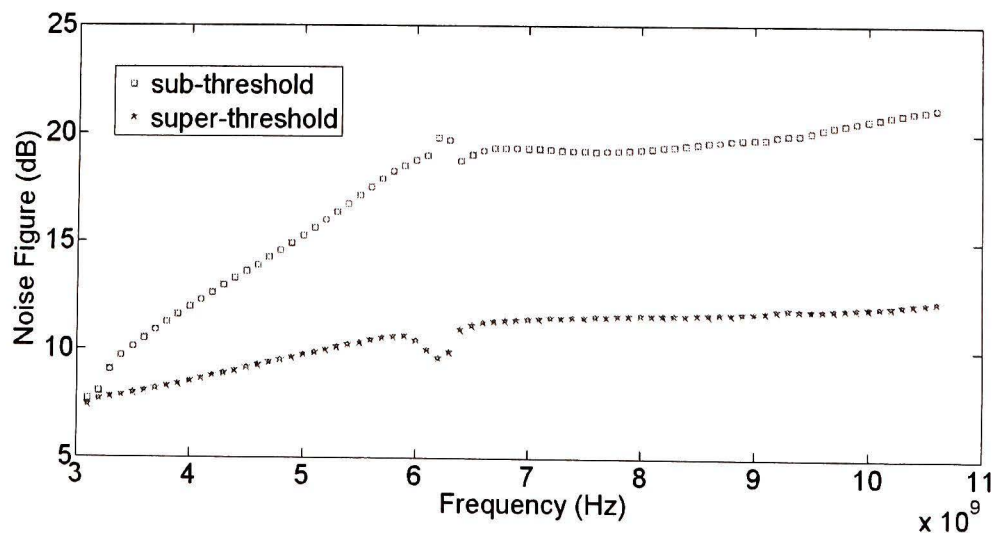


Figure 6.28. Mixer's noise figure for super- and sub-threshold modes.

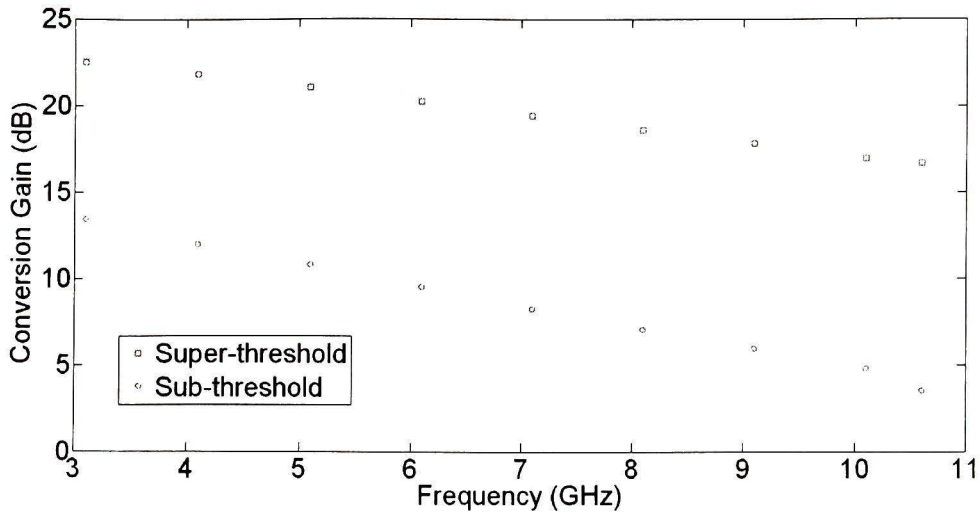


Figure 6.29. Mixer’s conversion gain for super- and sub-threshold modes.

Also it is shown in Figure 6.29 that switching from super-threshold mode to sub-threshold results in significant degradation in conversion gain. In spite of the large change in conversion gain, its curve still has the same behavior. Also, comparing to other works, the conversion gain of sub-threshold mixer is acceptable.

Figure 6.30 shows impedance matching and more specifically, reflection coefficient of the mixer before and after going to sub-threshold region. As shown, for both cases, this parameter shows completely acceptable results.

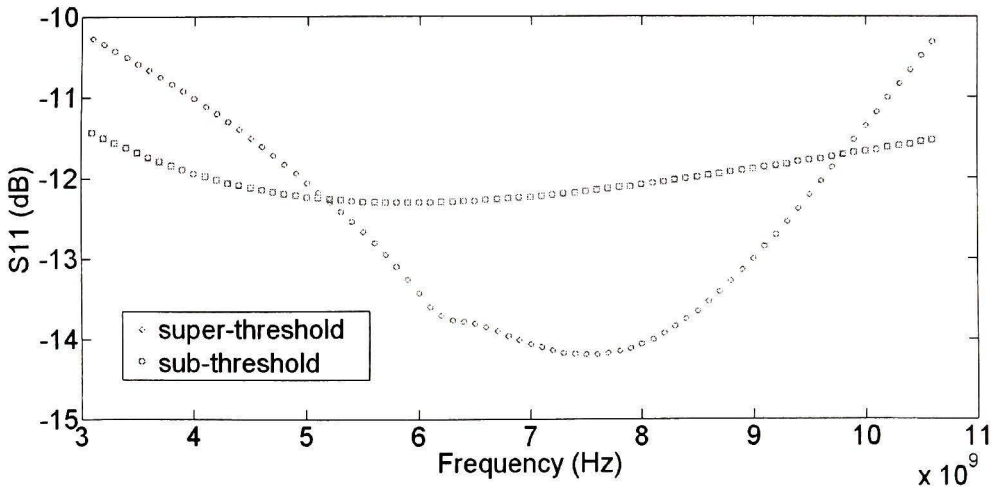


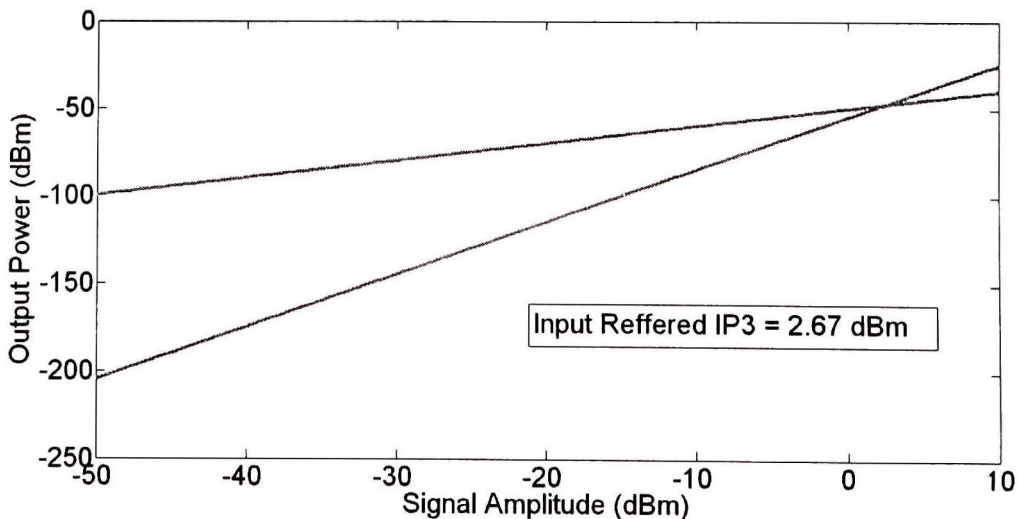
Figure 6.30. Mixer’s reflection coefficient for both super- and sub-threshold modes.

Finally, we have the input-referred third-order intercept point curves for both super- and sub-threshold approaches. As expected, linearity is also degraded due to decrease in bias current. Generally, when we go to the sub-threshold mode, since the bias current is

reduced, the voltage across the load resistors will be lower, and as a result, more voltage headroom will be present. But in this case, since we have used the folded-cascode architecture and voltage headroom is not an issue from the beginning, going to sub-threshold mode will only have negative effect on the linearity of the mixer.

Figure 6.31.a and b shows IIP3 (input referred third-order intercept point) for both super- and sub-threshold modes of operation. Again, we can see through comparison with other works that sub-threshold circuit's IIP3 is acceptable and can be compared with good mixer designs. Since both numbers are acceptable for our application, no linearity technique like what was explained previously in this Chapter is applied to this circuit.

Finally to compare results of both approaches, their specifications are presented in table 6.1. As shown, the sub-threshold approach resulted in very low power consumption with acceptable gain and linearity as well as input and output matching. On the other hand, the noise performance is not as good as what we had in super-threshold approach. Both designs show a good figure-of-merit and each one can be used for its own appropriate applications. For example, for high gain and low-noise applications in which power is not a major issue, super-threshold should be used. For low-power application in which lower gain values as well as higher noise figures are tolerable, sub-threshold circuit can be used.



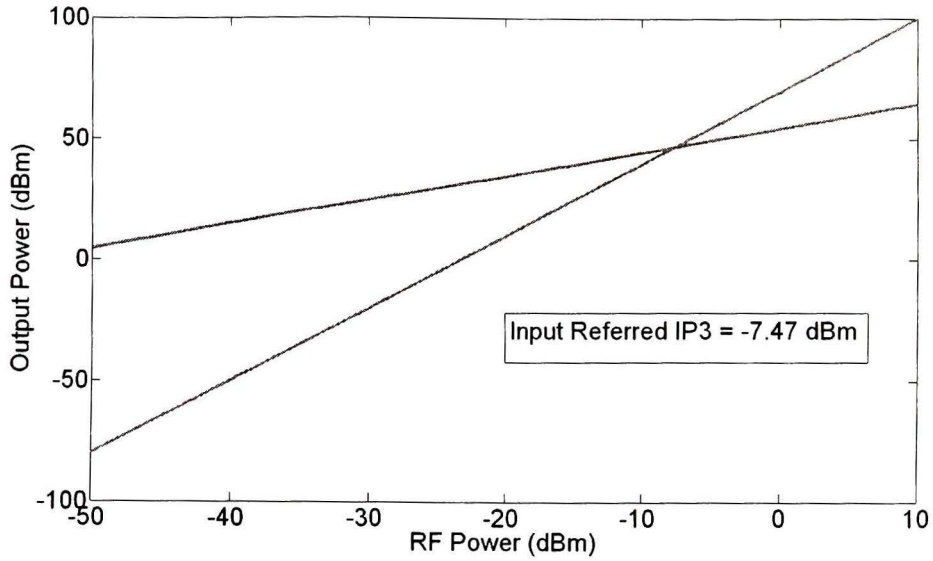


Figure 6.31. (a) IIP3 for superthreshold mode. (b) IIP3 for sub-threshold mode. Both of them are for 6 GHz.

Here in this work both of circuits are designed and simulated, but unfortunately due to lack of area, only sub-threshold circuit is fabricated.

Table 6.1

Mixer Specifications Comparison

	super-threshold	sub-threshold
Technology	.13um	
bandwidth (GHz)	3.1 - 10.6	
CG Max (dB)	22.54	13.44
IIP3 (dBm)	2.67	-7.47
NFmin (dB)	7.407	7.67
NFavg (dB)	9.58	16.32
Power Consumption (mW)	6.67	0.623
Input Reflection Coefficient(dB)	<-10.2	<-11.4
Power Supply (V)	1.2	
biasing circuits power (mW)	0.12	

### 6.5. Layout

As it was mentioned previously, only the sub-threshold IC was fabricated. Figure6.31 shows a screen capture of the 2mm × 2mm chip which was submitted for fabrication. Due to the small chip size, there was a limitation on number of input pins which was possible,

and as a result, an active balun was used to convert the single-ended input to differential signals for both RF and LO signals. Also, to perform de-embedding, bias circuits and balun are placed separately as test structures in the right half of the chip. Other test structures for calibration purposes are also added in this layout.

The layout design was done using the Virtuoso Layout Editor tool available in the Cadence package. The core folded cascode Gilbert mixer occupies an area of  $0.084 \text{ mm}^2$ . All of longer connections are tried to be drawn using MA which has the least sheet resistance and is the highest level of metal and furthest away from substrate which results in lowest parasitic capacitances. The tool provides a parasitic extraction function, which can be used for post layout simulations. However, this function does not work at the time the layout was being done.

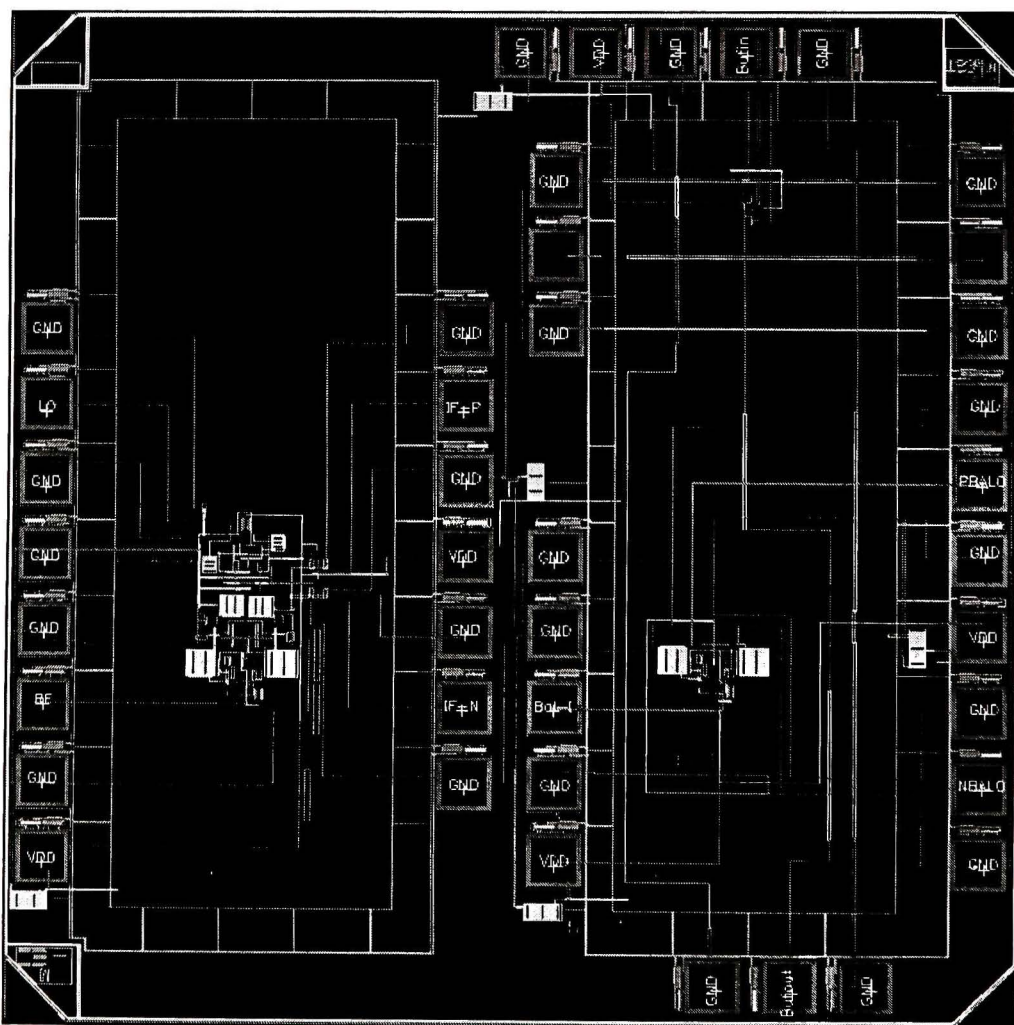


Figure 6.32. Layout picture of designed mixer

## 6.6. Measurement

Figure 6.33 shows a photograph of the complete layout of the fabricated chip. As shown, the chip is divided to two main parts. The circuit on the left is the designed mixer and in the right part of the chip we have designed Balun and output buffers separately for de-embedding purposes.

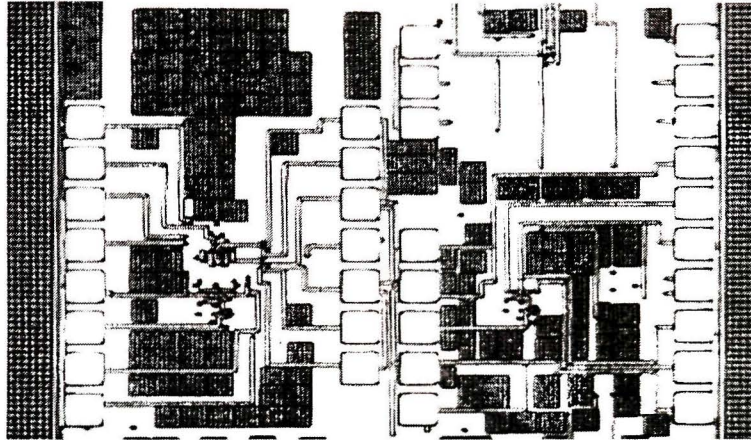


Figure 6.33. Photograph of designed mixer (in the left half), and balun and output buffer (on the right half of the picture).

All the top level metals can be clearly seen, which includes those are used for long paths and input and output pads for RF and DC signals.

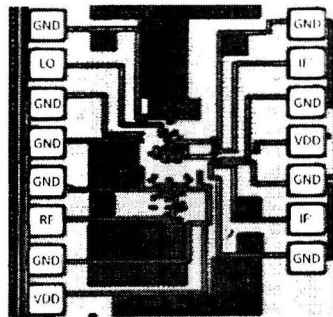


Figure 6.34. Designed mixer with specified inputs and outputs.

Also Figure 6.34 shows the mixer core which is designed with its inputs and outputs. Same as LNA, after Layout completion, post-layout simulation must be performed to see how parasitic elements due to interconnections affect the performance. Again, at the time of submission, since the Cadence kit was not able to extract parasitic elements including capacitance, inductance and resistance, this stage was done manually as it was explained for the LNA measurement.

The mixer is probed on-wafer using Picoprobe Multi-contact wedge probes. The DC voltages were provided by an HP4156B Semiconductor Parameter Analyzer. Here, since all DC bias voltages are designed internally, only  $V_{DD}$  and ground must have been provided.

Three sets of measurements were set up for this circuit. First, using a network analyzer, input and output impedance matching were measured. Here, unlike the LNA we don't need transmission and isolation parameters anymore and the only measured ones are reflection parameters. Usually for mixers, the only important reflection coefficient is  $S_{11}$  and  $S_{22}$  is not very important. Next test setup is for conversion gain measurement, in which, two signal generators and a spectrum analyzer are used. Finally we had noise figure measurement in which, a noise figure meter is used and will be described later.

Figure 6.35 shows test setup for reflection coefficient measurements. As shown, a synthesized sweeper provides LO signal while RF input is connected to "PORT A" of the PNA. Also each one of IF output ports are connected directly to "PORT B" of the PNA to be tested for impedance matching.

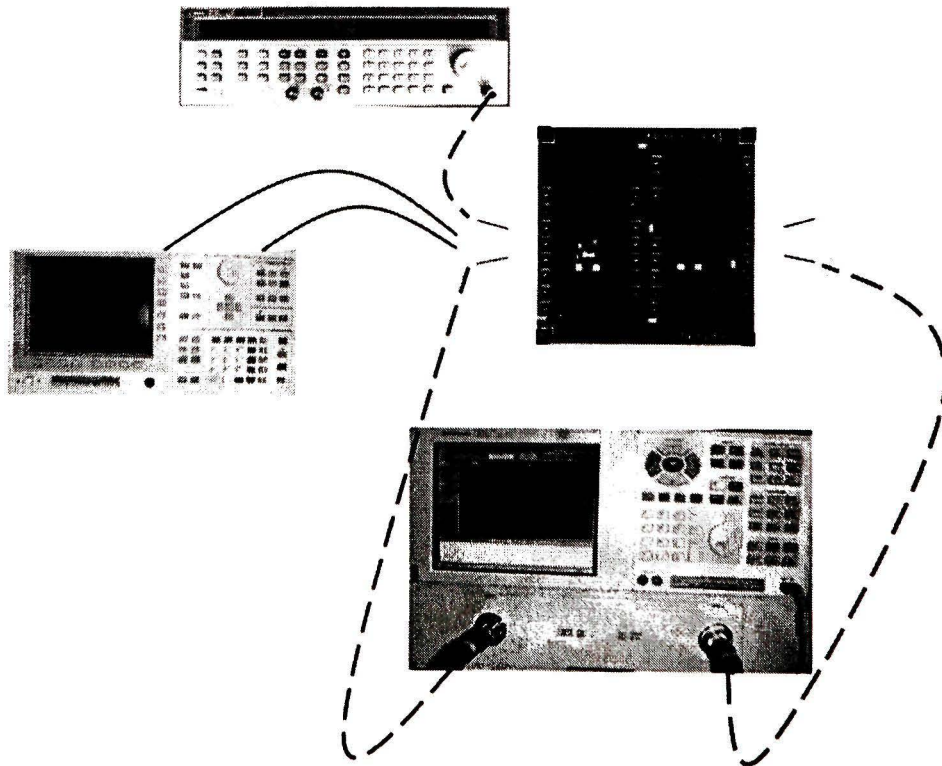


Figure 6.35. Measurement setup for measurement of reflection coefficient.

As shown in this figure, since we have used multi-wedge probes, DC voltages can be provided directly to these probes using BNC cables. As a result DC probe holders can be avoided in this setup. Figure 6.36 shows measurement results of mentioned test setup, in which,  $S_{11}$  is in good conditions.

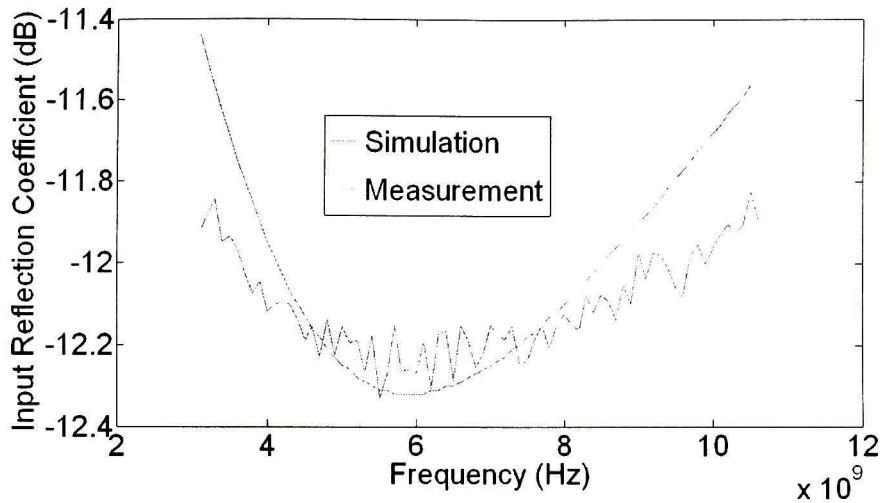


Figure 6.36. Measurement vs. simulation results for  $S_{11}$  of the mixer.

The next test setup is for conversion gain measurement, which is shown in Figure 6.37.

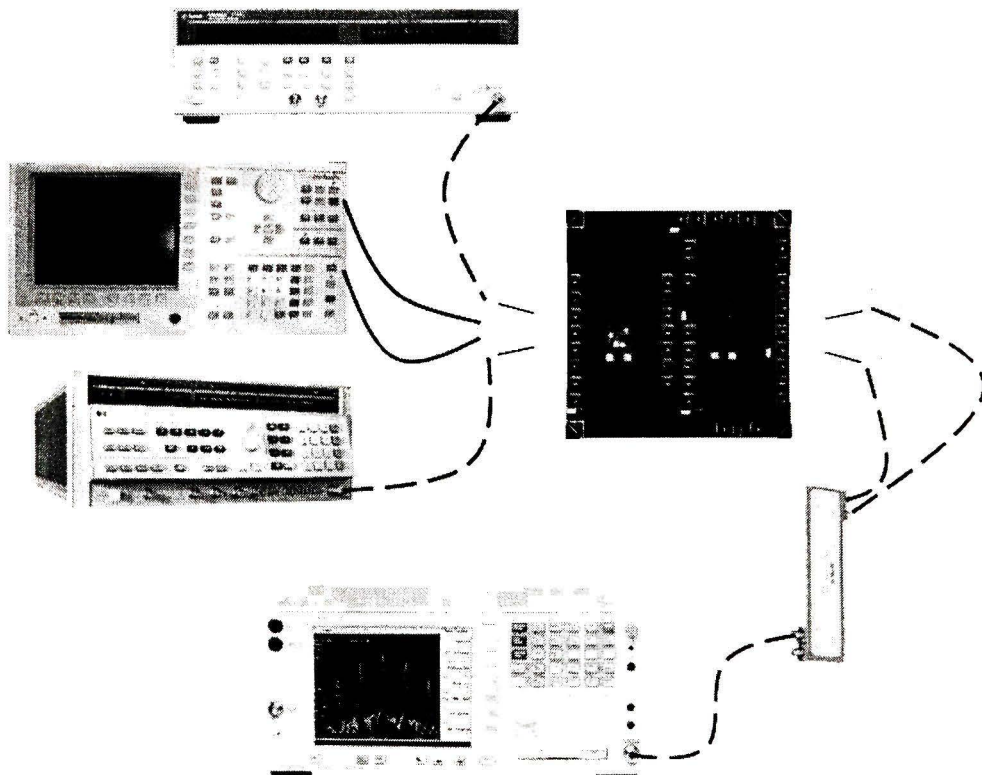


Figure 6.37. Test setup for measurement of conversion gain.

Here again, DC voltages,  $V_{DD}$  and GND, are connected through BNC connectors and there is no need to use DC probe holders. Also, as shown, two synthesized sweepers provide RF and LO signal as inputs of mixer-under-test. At the output, positive and negative intermediate-frequency outputs are connected to a signal combiner block. Task of this circuit is to subtract or add input signals. Here, we connect both IF outputs to input ports of this block and then output of this block is connected to RF input port of spectrum analyzer.

A complete set of calibrations was done for this measurement. First, since at the time of measurement, spectrum analyzer was not working properly for frequencies from 3 to 9 GHz, we just did the measurement for 9 to 10.6 GHz. Even considering that, we needed to de-embed effect of cables and signal combiner as well as internal circuits like output buffers and input baluns. All of these circuits are not part of mixer core and their effect must be de-eliminated. Because of this reason, in the right-half of the chip, balun and output buffer were laid out separately. To de-embed effect of all of additional elements, in the initial test, input and output cables were connected to the balun and buffer instead of mixer circuit. Figure 6.38 shows part of right-half of the chip where the input balun is laid out.

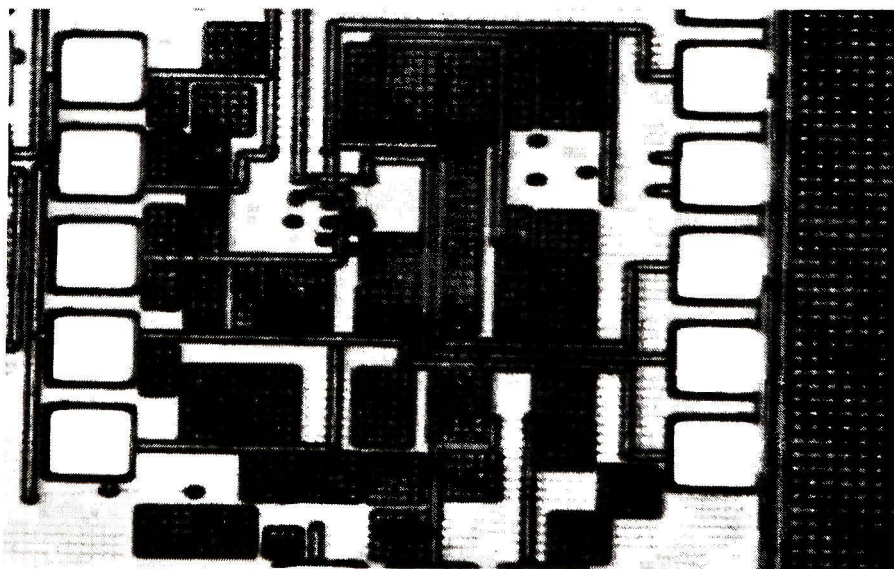


Figure 6.38. photograph of input balun on right-half of the chip.

Results of initial setup give us enough information to calculate mixer's conversion gain. In fact, when main circuit is put under probe as device under test, the measured conversion gain is a number which is affected by gain and loss of mixer plus other

elements such as balun, cables and signal combiner. Figure 6.39 shows measured conversion gain for the mixer after de-embedding and for 9 to 10.6 GHz. Results are in a good agreement with simulation results. The small difference between simulation and measurement results is due to the effect of parasitic elements which their model was not precise enough. Moreover, since the conversion gain is only measured for higher frequencies, we expect smaller difference in lower frequencies. This is mainly because of higher precision of modeling in lower frequencies. Finally, we should always consider error in measurement instruments.

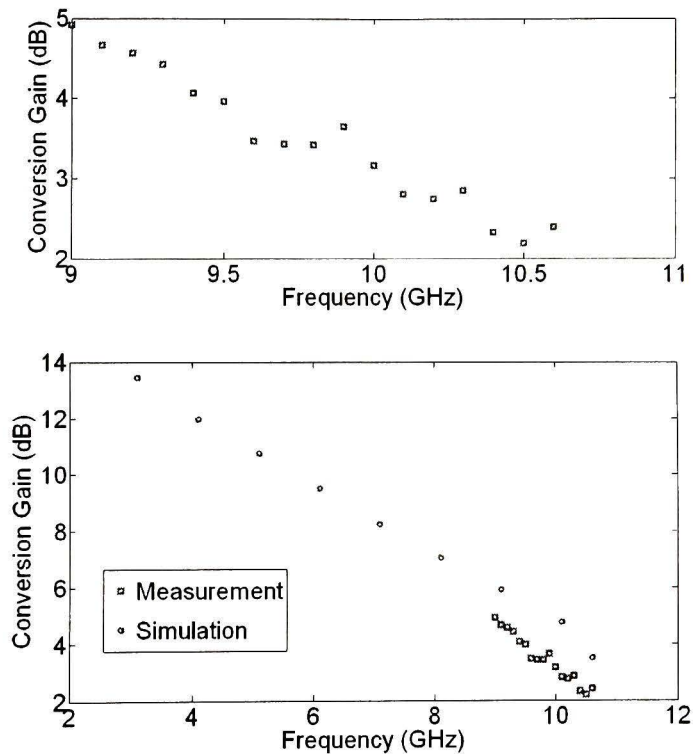


Figure 6.39. (Top) measurement results for conversion gain of the mixer. (Bottom) measurement vs. simulation results of mixer's conversion gain.

Finally we have noise figure measurement for the mixer. Same as LNA, we have to do this measurement in multiple steps so that measurement results would be only noise of the mixer. Here, first test setup is built as shown in Figure 6.40 for NF meter calibration. Using this configuration, noise which is added by output cables and signal combiner will be eliminated and will not affect final results. In other words, noise of all of structures which are connected to the output of the mixer are calculated in this stage and then NF

meter is calibrated in a way that mentioned structures will be part of NF meter and will not have any effect on final results.

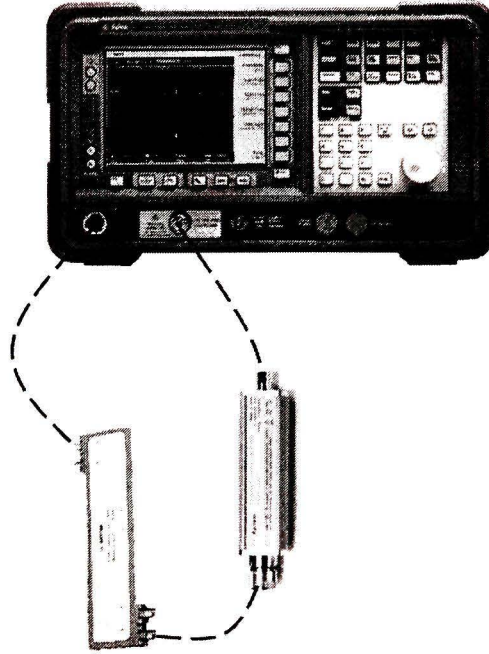


Figure 6.40. A measurement setup for output cable de-embedding and NF-meter calibration

Next step is to calculate noise figure generated by other noise sources like input cables and input balun. Figure 6.40 shows the test setup in which mentioned noises are measured. In this case probes are connected to the test structures on the right half of the chip. Using this setup, and considering that the effect of output cables and signal combiner are eliminated from measurement results, noise figure of input cables and input balun and probes can be measured. All of these noise sources which are located before mixer core, can be assumed as a first stage of a two stage system. Second stage of this system is the mixer core. Test setup for NF measurement of main circuit similar to the previous configuration except for DUT. In fact, this time, probes are connected to the mixer circuit on the left half of the chip. Measurement result of this configuration is the noise figure of the whole system. Now that we have noise figure for the two stages together and for the first stage, using Friis equation, noise figure of second stage which is the mixer core is measurable.

$$F_{total} = F_1 + \frac{F_2 - 1}{G_1} + \frac{F_3 - 1}{G_1 G_2} + \frac{F_4 - 1}{G_1 G_2 G_3} + \dots \quad (5.76)$$

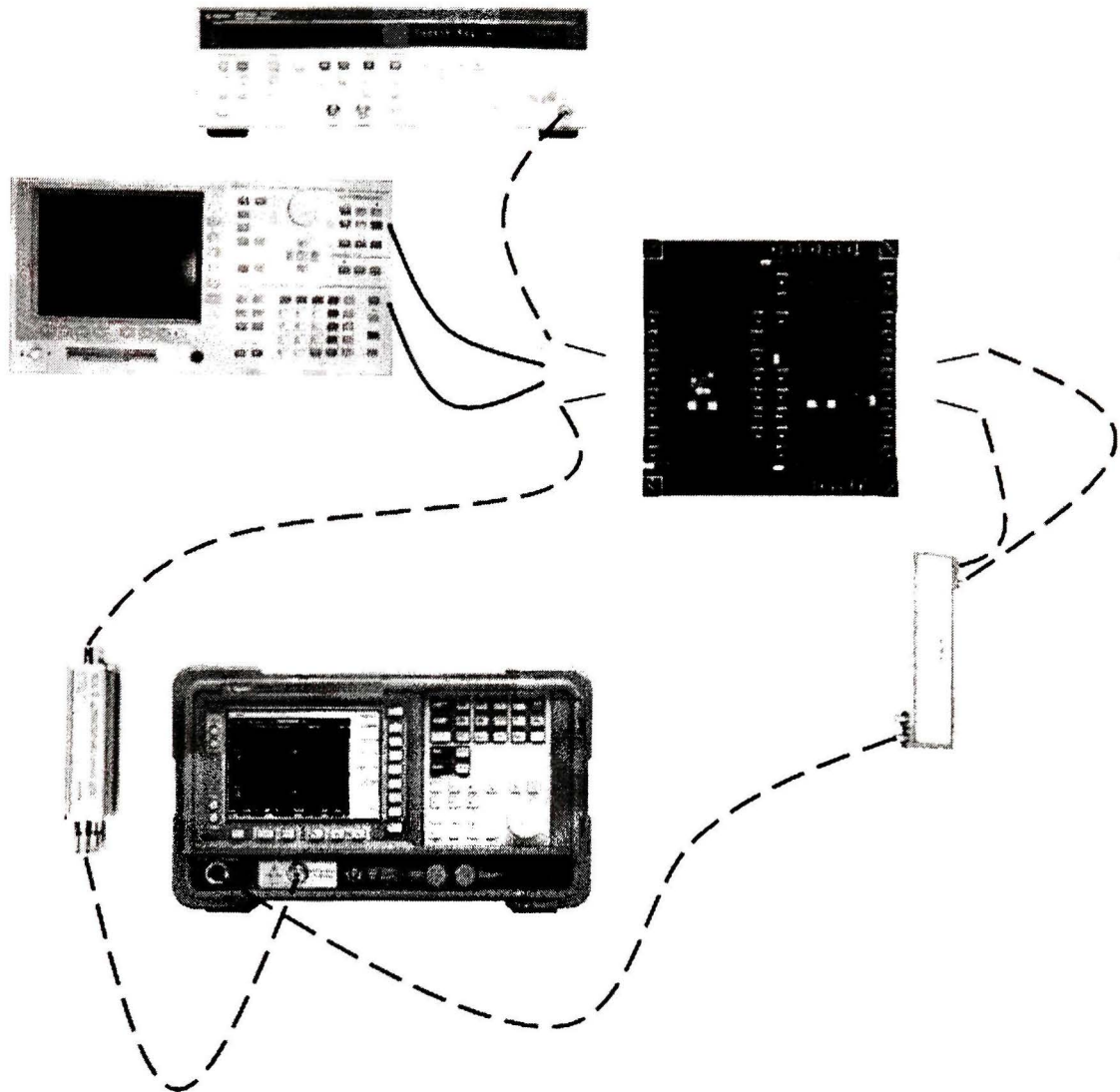


Figure 6.41. test setup to measure noise figure of input noise source structures ( in case probes are connected to the input balun) and to measure noise figure of whole circuit ( in case probes are connected to the main circuit).

Figure 6.42 shows measurement results for the noise figure of the mixer. Also noise figure of first stage and two stages together are shown. As we can see from this picture, measured and simulated noise figures are in a good agreement. Also from this picture, effect of de-embedding and calibration is shown clearly. While total noise figure for the whole circuit and connecting cables is much higher than simulation results, after de-embedding, we can see that mixer core's noise figure is very similar to our expectations from simulation. During our measurements, we saw that input structure's loss was much higher than what we expected before, with an average value of 6.5 dB. As shown in

Figure 6.42, for the majority part of the band, noise which is generated by the additional structures is much higher than the mixer itself.

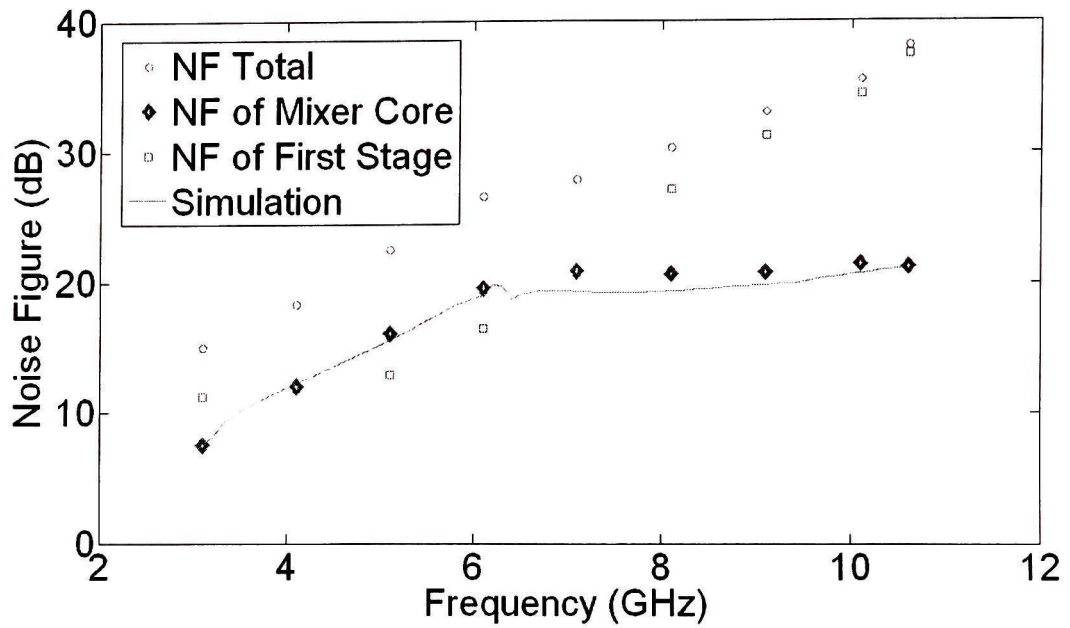


Figure 6.42. Measurement and simulation results for the mixer's noise figure. In this Figure NF of first stage means noise Figure of input structures which can be noise sources such as input cables and balun, etc.

# Chapter 7

## Conclusion and Future Works

---

### 7.1. Conclusion

Ultra Wide-Band communication is gaining a growing importance in medical imaging applications. In this thesis, we have focused on UWB application in one of the most serious diseases, namely breast cancer. High false-negative rate of detections in current imaging systems is one of the most important causes that made this type of cancer, second death cause in the world [1]. Considering this fact, detections systems demand for newer technologies with higher precision and reliability. UWB is one of technologies which have shown an excellent potential to be a very good substitute for existing systems.

UWB imaging system for breast cancer detection is made of several major blocks. Although, many variations for system's architecture are proposed, transmitter and receiver front-ends are two un-avoidable blocks which should be designed in all of them. In this thesis, two major blocks of UWB receiver which are used in this system are designed and fabricated. Our main concentration was performance improvement in terms of different design parameter so that better detection can be achieved. In contrast with other works which are mostly concentrated on block-level design, in this work circuit-level performance was our highest priority. In fact, not only each circuit's performance is tried to be improved, their connection to each other and they way they operate as system blocks are also considered.

First, for the LNA, a new design technique is applied to conventional CS configuration with inductive degeneration, resulting in better amplitude and flatness for voltage gain and input impedance matching as well as keeping other performance parameters constant. New design technique, is mainly based on a root-locus analysis and adding new circuit elements in a way that circuit's transfer function's poles and zeros will be relocated to new frequencies while new poles and zeros are added to the LNA too. With precise design of added elements, which are two inductors, and placing them between specific

nodes, added and relocated poles and zeros will result in a wider bandwidth and ability for higher gain value as well as better input impedance matching. The layout for designed LNA is sketched and the chip is fabricated and tested. The idea is vivified with the aid of simulation and measurement results and results show a considerable improvement in mentioned parameters.

Second, the mixer is designed based on a  $g_m$ -boosting folded cascode with resistive feedback configuration, resulting in high-gain and low power consumption in the same time. In addition, this circuit is designed in sub-threshold mode which is resulted in a very low power consumption compared to the state-of-the-art UWB mixers. Moreover, a UWB input Balun is designed and added to the mixer which improves conversion gain and input impedance matching considerably. Also, the Balun helps layout and measurement constraints, since it reduces number of input pads by 50%, which results in chip-area saving and easier measurement. Furthermore, with the added Balun, an inductor which was specially placed for input impedance matching can be removed, resulting in another reduction in chip-area. The layout for the mixer is also completed and the chip is fabricated and tested. Measurement results are in a good match with simulation and calculation results.

High and flat gain together with low noise Figure provides a low-noise amplified signal at the mixer's input and high conversion gain as well as low noise factor of the mixer will result in a well-shaped strong signal for intermediate-band signal processing unit. Due to low power consumption for both circuits, this signal can now be provided with a considerably lower cost.

## 7.2. Recommendation and Future Work

Although comparing figure of merit of designed circuits with the state-of-the-art works on LNA and mixer shows that both works' performance are excellent, there are some improvements that can be applied for both of circuits.

For the LNA, area is the main issue that should be considered. As a matter of fact, inductors are most area-consuming elements in the layout of analog and RF circuits and since our design has seven inductors, chip-area is rather larger than other works. Other than two inductors that are added in our work, there are three inductors in the input 3<sup>rd</sup>-

order Chebyshev network which increases chip area. For area-constraint applications, first,  $L_C$  can be removed with cost of slightly losing gain flatness and as a result we can only add  $L_D$ . result of this change is shown in simulation results of Chapter 5. Second, input network can be designed using other methods like 2<sup>nd</sup>-order filters or even inductor-less networks. The former will result in less precision in resonance frequencies determination, and the latter results in higher noise figure and possibly lower gain amplitude.

Also, since our main focus in this design has been on gain amplitude and flatness, while keeping other performance parameters in a good condition, these parameters have the potential to be improved. Especially with down-scaling of MOS devices, and the operating voltages and currents of circuits going down, design of low-noise circuits becomes even more challenging, since there is usually a trade-off between noise and power consumption of analog circuits [81].

For the mixer, the most important part to focus is the conversion gain flatness. In fact, since the conversion gain for the mixer core decreases with increasing frequency, adding a Balun which has the same behavior will result in a serious problem regarding gain flatness. One possible solution is to design a balun which its gain increases with the frequency, so that it can cancel the gain reduction of the mixer core. Different topologies are studied for a balun able to work in UWB range, but existing circuits does not have mentioned characteristics and to reach to such behavior, we need to design a new circuit and a new topology. Again, same as LNA, noise figure needs more study and work. Most importantly direct and indirect noise of switches in the LO stage of the mixer must be improved since they are the most important noise sources of this circuit.

Next important issue is connecting designed circuits. In fact since these circuits are parts of an integrated system, their combined performance is very important. In addition, connecting these circuits gives us a degree of freedom that can help in improving system's performance. To be clearer, when we designed each circuit individually, input and output impedance must have been 50  $\Omega$ . This was because this is the standard impedance which should be considered for most of RF circuits so that we can connect the circuit to the other circuits with optimum power transfer. Also for measurements, we needed a 50  $\Omega$  impedance matching to have a precise measurement results. However, in

this case, since we know that output of LNA is going to be connected to the mixer's input, these impedances (LNA's output impedance and mixer's input impedance) can be chosen at any value as long as they are equal. since output impedance of LNA is easily adjustable, as it was explained in Chapter 5, we can work on mixer's gain and noise figure and then adjust LNA's output impedance in a way such that it will be equal to mixer's new input impedance. In this way, mixer's input impedance matching is not an issue anymore, resulting in performance improvement of this circuit in terms of other parameters such as conversion gain, noise and linearity.

# References

---

- [1] Jemal A, Siegel R, Ward E et al. "Cancer statistics". CA Cancer J Clin 58 (2): 71–96, 2008.
- [2] E. C. Fear, X. Li, S. C. Hagness, M. A. Stuchly, "Confocal microwave imaging for breast cancer detection: localization of tumors in three dimensions," IEEE Transactions on Biomedical Engineering, vol. 49, pp.48-56, 2002.
- [3] W. T. Joines, Y. Zhang, C. Li, and R. L. Jirtle, "The measured electrical properties of normal and malignant human tissues from 50 to 900 MHz," Med. Phys., vol. 21, pp. 547–550, 1994.
- [4] Y. Xie, B. Guo, L. Xu, J. Li, and P. Stoica, "Multistatic Adaptive Microwave Imaging for Early breast Cancer Detection" IEEE Trans. Biomed. Eng., vol.53, pp.1647-1657, 2006.
- [5] L. Xu, S. Davis, S. C. Hagness, D. Weide, B. Veen, "Microwave Imaging via Space–Time Beamforming: Experimental Investigation of Tumor Detection in Multilayer Breast Phantoms," IEEE Trans. Microwave & Theory Tech., vol. 52, pp. 1856–1865, 2004.
- [6] Xia Xiao, T.Kikkawa, "Study on the Breast Cancer Detection by UWB Microwave Imaging", IEEE 2008.
- [7] John McCorkle, "Ultra Wide Bandwidth (UWB): Gigabit Wireless Communications for Battery Operated Consumer Applications", 2005 Symposium on VLSI Circuits Digest of Technical Papers
- [8] K. Siwiak, "Ultra-wide band radio: Introducing a new technology," in Proc. IEEE Veh. Technol. Conf., vol. 2, pp. 1088–1093, May 2001.
- [9] K. Siwiak, P. Withington, and S. Phelan, "Ultra wide band radio: The emergence of an important new technology," IEEE Veh. Technol.Conf., vol. 2, pp. 1169-1172, May 2001.
- [10] "Ultra-Wideband First Report and Order," Federal Communication Commission, Tech. Rep., February 2002.

- [11] Nekoogar, F. “*Ultra-wideband Communications: Fundamentals and Applications*” Prentice Hall, Sydney, 2005
- [12] T. E. McEwan, “*Body monitoring and imaging apparatus and method*,” US Patent No. 5,573,012, Issued on November 12, 1996.
- [13] Xu Yong, Lu Yinghua, Zhang Hongxin, Wang Yeqiu, “*An Overview of Ultra-Wideband Technique Application for Medial Engineering*,” 2007 IEEE/ICME International Conference on Complex Medical Engineering(CME), Beijing, May 2007.
- [14] Enrico M. Staderini, “*UWB radars in medicine*,” IEEE Aerospace and Electronic Systems Magazine, Vol. 17, Issue 1, Page:13-18, 2002
- [15] LK Hady, AA Kishk , “*Ultra-Wideband Transceiver Architecture for Early Breast Cancer Detection System*,” 2007 IEEE Region 5 Technical Conference, 2007.
- [16] M. Patlak, S. Nass, I. Henderson, and J. Lashof, editors. “*Mammography and Beyond: Developing Technologies for the Early Detection of Breast Cancer*”. The National Academies Press, 2001.
- [17] Bond E J, Li X, Hagness S.C. and Van Veen B.D. *Microwave imaging via space-time beamforming for early detection of breast cancer IEEE Trans. Antennas Propag.* 51 1690–705, 2003.
- [18] P. T. Huynh, A. M. Jarolimek, and S. Daye, “*The false-negative mammogram*,” Radiograph., vol. 18, no. 5, pp. 1137–1154, 1998.
- [19] Elmore JG, Barton MB, Mocerri VM, et al. Ten-year risk of false positive screening mammograms and clinical breast examinations. *N. Engl J. Med*; 338: 1089–96, 1998.
- [20] Foster K R and Schwan H P, “*Dielectric properties of tissues and biological materials*”, A critical review *Crit. Rev. Biomed. Eng.* 17, 25–104, 1989.
- [21] K. S. Osterman, T. E. Kerner, D. B. Williams, A. Hartov, S. P. Poplack, and K. D. Paulsen, *Multifrequency electrical impedance imaging: preliminary in vivo experience in breast*, *Physiol Meas*, 21, pp. 99-109, 1989.
- [22] J. L. Mueller, S. Siltanen and D. Isaacson. “*A direct reconstruction algorithm for electrical impedance tomography*.” *IEEE Trans. Medical Imaging*, 216, pp.555–559, 1989.

- [23] T. O. McBride, B. W. Pogue, S. D. Jiang, U. L. Osterberg, K. D. Paulsen, and S. P. Poplack, “*Initial studies of in vivo absorbing and scattering heterogeneity in near-infrared tomographic breast imaging*,” *Opt. Lett.* 26, 822–824, 2001.
- [24] Oppermann, I., M. Hamalainen, and J. Iinatti, *UWB Theory and Applications*, Chapter 6, John Wiley and Sons, 2004.
- [25] H.M. Jafari, M.J. Deen, S. Hranilovic and N.K. Nikolova, A Study of Ultra-Wideband Antennas for Near-Field Imaging, *IEEE Transactions on Antennas and Propagation*, Vol. 55(4), pp. 1184-1188 (April 2007).
- [26] J. G. Proakis, *Digital Communications*. New York: McGraw-Hill, 1995.
- [27] Lang, J. “*UWB chip design with embedded functionality*”, UWB Summit, Paris, France, CD Proceedings, 1989.
- [28] Funk, E., S. Sadow, L. Jasper and A. Lee ‘*Time coherent ultra-wideband pulse generation using photoconductive switching*’, *Digest of the LEOS Summer Topical Meetings*, pp. 55–56, 1995.
- [29] Montoya T. P, Smith G. S. ‘*A study of pulse radiation from several broad-band loaded monopoles*’, *IEEE Transactions on Antennas and Propagation*, 44, pp.1172–1182, Aug 1996.
- [30] van Cappellen W. A., de Jongh R. V., Ligthart L. P. (2000) ‘*Potentials of ultra-short-pulse time-domain scattering measurements*’, *IEEE Antennas and Propagation Magazine*, 42, pp. 35–45, Aug 2000.
- [31] Shlager K. L., Smith G. S., Maloney J. G. ‘*Accurate analysis of TEM horn antennas for pulse radiation*’, *IEEE Transactions on Electromagnetic Compatibility*, 38, pp. 414–423, 1996.
- [32] Baum C. E., Stone A. P. (1993) “*Transient lenses for transmission systems and antennas*”, in *Ultra-Wideband Short Pulse Electromagnetics* , H. L. Bertoni, L. Carin, and L. B. Felsen, Eds., New York: Plenum Press, pp. 211–219, 1993.
- [33] Baum C. E., Farr E. G. (1993) ‘*Impulse radiating antennas*’, *Ultra-Wideband Short Pulse Electromagnetics* , H. L. Bertoni, L. Carin, and L. B. Felsen, Eds., New York: Plenum Press, pp. 139–147, 1993.
- [34] Kardo-Sysoev, A. F., V. I. Brylevsky, Y. S. Lelikov, I. A. Smirnova and S. V. Zazulin (1999) ‘*Generation and radiation of powerful nanosecond and sub-nanosecond*

pulses at high pulse repetition rate for UWB systems', 1999 International Ultra-wideband Conference, Washington, DC USA.

[35] "Feasibility study and design of a low-cost system-on-a-chip microwave radiometer on silicon" Fonte, A.; Zito, D.; Neri, B.; Alimenti, F.; Waveform Diversity and Design Conference, International Page(s): 37 – 41, 2007.

[36] L. Yang, Y. Kiat Seng, A. Cabuk, M. Jianguo, D. Manh Anh and L. Zhenghao, "A novel CMOS low-noise amplifier design for 3.1 to 10.6-GHz ultra-wide-band wireless receivers," IEEE Transaction on Circuits and Systems, vol. 53, no. 8, pp. 1683-1692, Aug. 2006.

[37] W. Zhuo, X. Li, S. Shekhar, S. H. K. Embabi, J. Pineda de Gyvez, D.J. Allstot, and E. Sanchez-Sinencio, "A capacitor cross-coupled common-gate low-noise amplifier," IEEE Transactions on Circuits and Systems- II: Express Briefs, vol. 52, no. 12, pp. 875–879, Dec. 2005.

[38] C. W. Kim, M. S. Kang, P. T. Anh, H. T. Kim and S. G. Lee, "An Ultra-wide-band CMOS low-noise amplifier for 3–5 GHz UWB system," IEEE J. Solid-State Circuits, vol. 40, no. 2, pp. 544–547, Feb. 2005.

[39] C.-W. Kim, M.-S. Kang, P. T. Anh, H.-T. Kim and S.-G. Lee, "An ultra-wideband CMOS low noise amplifier for 3–5-GHz UWB system," IEEE J. Solid-State Circuits, vol. 40, no. 2, pp. 544–547, Feb. 2005.

[40] R. C. Liu, K. L. Deng, and H. Wang, "A 0.6–22-GHz broadband CMOS distributed amplifier," in Proc. IEEE Radio Freq. Integrated Circuits Symposium Digest, Philadelphia, PA, pp. 103–106, June 2003.

[41] J.C. Ranuárez, M.J. Deen and C.H. Chen, Temperature Effects in CMOS Microwave Distributed Amplifiers, Journal of Vacuum Science and Technology A (Special Issue for CSTC 2005), Vol A24(3), pp. 831–834, (May 2006).

[42] Y-J. Lin, S.S.H. Hsu, J-D. Jin and C. Y. Chan, "A 3.1–10.6 GHz ultra-wideband CMOS low noise amplifier with current-reused technique," IEEE Microwave and Wireless Components Letters, vol. 17, no. 3, pp. 232–234, March 2007.

[43] S. P. Voinigescu, T. O. Dickson, T. Chalvatzis, A. Hazneci, E. Laskin, R. Beerkens, and I. Khalid, "Algorithmic design methodologies and design porting of wireline

- transceiver IC building blocks between technology nodes,”* in IEEE Custom Integrated Circuits Conference, 18-21 September 2005, pp. 111–118.
- [44] J. Borremans, P. Wambacq, and D. Linten, “*An ESD-protected DC-to-6GHz 9.7mW LNA in 90nm digital CMOS,*” in IEEE International Solid-State Circuits Conference, San Francisco, 11-15 February 2007, pp. 422–423.
- [45] R. Ramzan, S. Andersson, J. Dabrowski, and C. Svensson, “*A 1.4V 25mW inductorless wideband LNA in 0.13 $\mu$ m CMOS,*” in IEEE International Solid-State Circuits Conference, San Francisco, pp. 424–425, 11-15 February 2007.
- [46] H. A. Haus, W. R. Atkinson, W. H. Fonger, W. W. McLeod, G. M. Branch, W. A. Harris, E. K. Stodola, W. B. Davenport, Jr., S. W. Harrison, and T. E. Talpey, “*Representation of noise in linear twoports,*” Proceedings of the Institution of Radio Engineers, vol. 48, no. 1, pp. 66–74, January 1960.
- [47] H. Rothe, “*The theory of noisy four-poles,*” IEEE Transactions on Electron Devices, vol. 1, no. 4, pp. 258–259, December 1954
- [48] H. Hillbrand and P. H. Russer, “*An efficient method for computer aided noise analysis of linear amplifier networks,*” IEEE Transactions on Circuits and Systems, vol. 23, no. 4, pp. 235–238, April 1976.
- [49] A. Bevilacqua and A. M. Niknejad, “*An ultrawideband CMOS low noise amplifier for 3.1–10.6 GHz wireless receivers,*” IEEE Journal of Solid-State Circuits, vol. 39, no. 12, pp. 2259–2268, Dec. 2004.
- [50] P. H. Woerlee, M. J. Knitel, R. van Langevelde, D. B. M. Klaassen, L. F. Tiemeijer, A. J. Scholten, and A. T. A. Zegers-van Duijnhoven, “*RF-CMOS performance trends,*” IEEE Trans. Electron Devices, vol. 48, pp. 1776–1782, 2001.
- [51] M. J. Deen, C.-H. Chen, S. Asgaran, G. A. Rezvani, J. Tao and Y. Kiyota, High Frequency Noise of Modern MOSFETs: Compact Modeling and Measurement Issues, IEEE Transactions on Electron Devices (Special Issue on Advanced Compact Models and 45-nm Modeling Challenges), Vol. 53(9), pp. 2062-2081 (Sep. 2006).
- [52] V. Aparin and L. Larson, “*Modified derivative superposition method for linearizing fet low-noise amplifiers,*” IEEE Transactions on Microwave Theory and Techniques, vol. 53, no. 2, pp. 571–581, Feb 2005.

- [53] Leonid Belostotski (2007), “*Wide-Band CMOS Low Noise Amplifier for the Square Kilometer Array Radio Telescope*” thesis (Ph.D.), University of Calgary.
- [54] T. H. Lee, “*The Design of CMOS Radio-Frequency Integrated Circuits*”, 1<sup>st</sup> ed. New York: Cambridge Univ. Press, 1998.
- [55] S. Asgaran, M.J. Deen, and C-H. Chen, Design of the Input Matching Network of RF CMOS LNAs for Low-Power Operation, *IEEE Transactions on Circuits and Systems I*, Vol. 54(3), pp. 544-554 (March 2007).
- [56] S. Asgaran, M.J. Deen and C.-H. Chen, A 4 mW Monolithic CMOS LNA at 5.7 GHz with the Gate Resistance Used for Input Matching, *IEEE Microwave and Wireless Components Letters*, Vol. 16(4), pp. 188-190 (April 2006).
- [57] G. Matthaei, L. Young, and E. M. T. Jones, “*Microwave Filters Impedance-Matching Networks and Coupling Structures*”. New York: McGraw-Hill, 1964.
- [58] S. Shekhar, J. S.Walling, and D. J. Allstot, “*Bandwidth extension techniques for CMOS amplifiers,*” *IEEE Journal of Solid-State Circuits*, vol. 41, no. 11, pp. 2424–2439, Nov. 2006.
- [59] Xiaohua Fan, Edgar Sánchez-Sinencio, and Jose Silva- Martínez, “*A 3GHz-10GHz Common Gate Ultrawideband Low Noise Amplifier, IEEE Midwest Symposium on Circuits and Systems*”, pp 631-634, Aug 2005.
- [60] Chen, J. (2008), “*RF IC Design- 6*”, Lecture, McMaster University, unpublished.
- [61] M. Jamal Deen, Rizwan Murji, Ahmed Fakhr, Nabeel Jafferli and Wai Leung Ngan, Low Power CMOS Integrated Circuits for Radio Frequency Applications, *IEE Proceedings - Circuits, Devices and Systems*, Vol. 152(5), pp. 509-522 (October 2005).
- [62] A. Zolfaghari and B. Razavi, “*A Low-Power 2.4-GHz Transmitter/Receiver CMOS IC,*” *IEEE J. Solid-State Circuits*, vol. 38, pp. 176-183, Feb. 2003.
- [63] S. Asgaran and M.J. Deen, A Flicker Noise Cancellation Technique for Low-Voltage Direct-Conversion Mixers, *Electronics Letters*, Vol. 43(19), pp. 1020-1021 (13 September 2007).
- [64] T. Wang, et al., “*A low-power oscillator mixer in 0.18-um CMOS technology,*” *IEEE Trans. Microwave Theory Tech.*, vol. 54, no. 1, pp. 88-95, Jan. 2006.
- [65] C. Tang, et al., “*A 2.4-GHz CMOS down-conversion doubly balanced mixer with low supply voltage,*” in *Proc, IEEE Int. Symp. Circuits & Systems (ISCAS)*, vol. 4, May

2001, pp.794-797.

[66] C. Hermann, M. Tiebout and H. Klar, “*A 0.6-V 1.6-mW Transformer-Based 2.5-GHz Downconversion Mixer With +5.4-dB Gain and -2.8-dBm IIP3 in 0.13-um CMOS*,” IEEE Trans. Microwave Theory Tech., vol. 53, no. 2, pp. 488-495, Feb. 2005.

[67] G. Kathiresan, C. Toumazou, “*A Low Voltage Bulk Driven Downconversion Mixer Core*,” in Proc. IEEE Int. Symp. Circuits & Systems (ISCAS), vol. 2, May 1999, pp. 598-601.

[68] H. H. Hsieh and L. H. Lu, “*Design of ultra-low-voltage RF frontends with complementary current-reused architectures*,” IEEE Trans. Microw. Theory Tech., vol. 55, no. 7, pp. 1445–1458, Jul. 2007.

[69] L. K. Meng, N. C. Yong, Y. K. Seng, and D. M. Anh, “*A 2.4 GHz ultra low power subthreshold CMOS low-noise amplifier*,” Microw. Opt. Technol. Lett., vol. 49, no. 4, pp. 743–744, Apr. 2007.

[70] J. B. Seo et al., “*A Low-Power and High-Gain Mixer for UWB Systems*,” IEEE microwave and wireless components letters, VOL. 18, NO. 12, DECEMBER 2008

[71] H. Lee, S. Mohammadi, “*A Low-Power and High-Gain Mixer for UWB Systems*,” 2007 IEEE Radio Frequency Integrated Circuits Symposium, 2007.

[72] S.K. Hampel et al, “*Low-Voltage, Inductorless Folded Down-Conversion Mixer in 65nm CMOS for UWB Applications*,” 2009 IEEE Radio Frequency Integrated Circuits symposium, 2009.

[73] A. Rofougaran, J. Y. C. Chang, M. Rofougaran, and A. A. Abidi, “*A 1 GHz CMOS RF front-end IC for a direct-conversion wireless receiver*,” IEEE J. Solid-State Circuits, vol. 31, pp. 880–889, July 1996.

[74] Payam Heydari, “*High-Frequency Noise in RF Active CMOS Mixers*”, Proceedings of the ASP-DAC Asia and South-Pacific, pp.57-61, 27-30 January 2004.

[75] H. Darabi and A. A. Abidi, “*Noise in RF-CMOS mixers: A simple physical model*,” IEEE J. Solid-State Circuits, vol. 35, pp. 15–25, Jan. 2000

[76] J. Chang, A. A. Abidi, and C. R. Viswanathan, “*Flicker noise in CMOS transistors from sub-threshold to strong inversion at various temperatures*,” IEEE Trans. Electron Devices, vol. 41, pp. 1965–1971, Nov. 1994.

- [77] D. M. Binkley, J. M. Rochelle, B. K. Swann, L. G. Clonts, and R. N. Goble, “*A micro-power CMOS direct-conversion, VLF receiver chip for magnetic-field wireless applications*,” IEEE J. Solid-State Circuits, vol. 33, pp. 344–358, Mar. 1998.
- [78] L. MacEachern, and T. Manku, “*A Charge-Injection Method for Gilbert Cell Biasing*”, Proceeding of the IEEE Canadian Conference on Electrical and Computer Engineering (CCECE 98), pp. 365-368, 1998.
- [79] Motieifar, A., Pour, Z.A., Bridges, G., Shafai, C. and Shafai, L., “*An Ultra Wideband (UWB) Mixer with 0.18UM RF CMOS Technology*”, Electrical and Computer Engineering, Canadian Conference on, Pages : 697-700, May 2006.
- [80] C.I. Shie et al, “*UWB LNA and mixer with an active balun in 0.18 $\mu$ m CMOS process*,” Microwave Conference, 2009. APMC 2009. Asia Pacific, 2009
- [81] Rizwan Murji and M. Jamal Deen, Design Issues of a Low Power Wideband frequency Doubler Implementation in 0.18  $\mu$ m CMOS, Analog Integrated Circuits and Signal Processing Vol. 53(1), pp. 53-62 (October 2007).